

Star formation history of Canis Major OB1

II. A bimodal X-ray population revealed by *XMM-Newton*

T. Santos-Silva^{1,2,3}, J. Gregorio-Hetem², T. Montmerle³, B. Fernandes^{2,3} and B. Stelzer^{4,5}

¹ Universidade Federal do Rio Grande do Sul, Brazil,
e-mail: thais.santos@ufrgs.br

² Universidade de São Paulo, IAG, Departamento de Astronomia, Brazil,

³ Institut d'Astrophysique de Paris, France

⁴ Eberhard-Karls Universität, Institut für Astronomie und Astrophysik, Sand 1, D-72076 Tübingen, Germany

⁵ INAF - Osservatorio Astronomico di Palermo, Piazza del Parlamento 1, 90134 Palermo, Italy

September 27, 2018

ABSTRACT

Aims. The Canis Major OB1 Association has an intriguing scenario of star formation, especially in the region called Canis Major R1 (CMa R1) traditionally assigned to a reflection nebula, but in reality an ionized region. This work is focused on the young stellar population associated to CMa R1, for which our previous results from ROSAT, optical and near-infrared data had revealed two stellar groups with different ages, suggesting a possible mixing of populations originated from distinct star-formation episodes.

Methods. The X-ray data allow the detected sources to be characterized according to hardness ratios, light curves and spectra. Estimates of mass and age were obtained from the *2MASS* catalogue, and used to define a complete subsample of stellar counterparts, for statistical purposes.

Results. A catalogue of 387 *XMM-Newton* sources is provided, 78% being confirmed as members or probable members of the CMa R1 association. Flares (or similar events) were observed for 13 sources, and the spectra of 21 bright sources could be fitted by a thermal plasma model. Mean values of fits parameters were used to estimate X-ray luminosities. We found a minimum value of $\log(L_X[\text{erg/s}]) = 29.43$, indicating that our sample of low-mass stars ($M_* \leq 0.5M_\odot$), being faint X-ray emitters, is incomplete. Among the 250 objects selected as our complete subsample (defining our “best sample”), 171 are found to the East of the cloud, near Z CMa and dense molecular gas, 50% of them being young (< 5 Myr) and 30% being older (> 10 Myr). The opposite happens to the West, near GU CMa, in areas lacking molecular gas: among 79 objects, 30% are young and 50% are older. These findings confirm that a first episode of distributed star formation occurred in the whole studied region ~ 10 Myr ago and dispersed the molecular gas, while a second, localized episode (< 5 Myr) took place in the regions where molecular gas is still present.

Key words. X-rays: stars; infrared: stars; star formation regions: X-rays; early-type; open clusters and associations: general; stars: Young Stellar Objects -YSO, stars: formation; stars: pre-main sequence

1. Introduction

The efficiency of using X-ray observations to discover large samples of pre-main sequence stars has been demonstrated in many star-forming regions. For instance, thousands of X-ray sources have been identified in Orion Nebula by means of the *Chandra* Orion Ultradeep Project – COUP (Getman et al. 2005b,a) and several hundreds were detected in the Taurus Molecular Cloud by means of the *XMM-Newton* Extended Survey of Taurus – XEST (Güdel et al. 2007).

The method is now familiar: the X-rays come from high-mass stars owing to their strong wind shocks, and also from the numerous young, low-mass stars ($M_* < 2M_\odot$: T Tauri stars), owing to their magnetic activity and/or accretion, which may be present up to a relatively old age (~ 10 Myr, depending on their mass). Therefore, once they have lost their accretion disks (no IR excess, no $H\alpha$ emission: ages ≥ 10 Myr), X-rays are the only way to identify the stars as being young. The ages are then derived using colour-magnitude diagrams and theoretical Pre-Main Sequence (PMS) evolutionary tracks.

The discovery of large samples of PMS stars has shown that many star-forming regions seem to have complex star formation histories, typically involving a sequence of individual episodes that created different sub-groups or clusters. For an understanding of the star formation process, it is therefore of essential importance to look for young stars not only around the center of a prominent cluster, but also to investigate its environment, in order to detect and identify *distinct stellar populations* that often are found in separate clusters or groups, having different ages.

One prominent example is the Scorpius-Centaurus OB association, where the individual sub-groups have ages between ~ 5 Myr and ~ 15 Myr (Preibisch & Mamajek 2008). A similar situation, although with smaller age differences of just a few Myr, is seen in the sub-groups of the Ori OB1 association (Bally 2008). The ~ 4 Myr stars of the Ori OB1c sub-group are seen in projection directly in front of the famous Orion Nebula Cluster and contaminate the cluster.

Another spectacular illustration of the diversity of young populations, not only in age, but also in space, is provided by the *Chandra* 22-field mosaic, ~ 1.4 sq. deg. survey of the Carina nebula (Townsend et al. 2011; Feigelson et al. 2011), where

Send offprint requests to: T. Santos-Silva

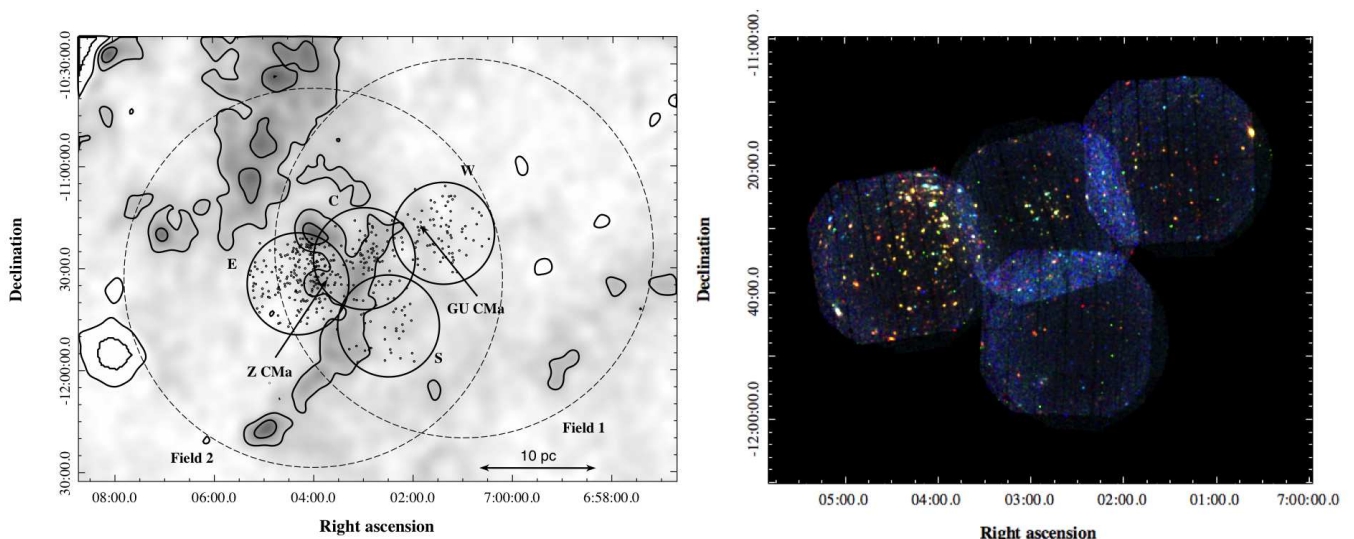


Fig. 1. *Left:* Spatial distribution of X-ray sources detected by *XMM-Newton* (fields E,C,S and W - full lines) on the A_V map (Cambr s, private communication) with $A_V = 2.0$ and 4.0 mag contours, compared with *ROSAT* fields from Gregorio-Hetem et al. (2009) (dashed lines). *Right:* Mosaic of images of *XMM-Newton* EPIC PN, MOS 1 and MOS 2 for the same CMa fields combined in three different energy bands. The filters red, green and blue present the soft band (0.5-1.0 keV), medium band (1.0-2.0 keV) and hard band (2.0-7.3 keV) respectively.

the $\sim 10,000$ X-ray sources detected as young stars clearly belong to two distinct, equally numerous groups: (i) a *clustered* population, with centrally concentrated distributions of stars (including cases of “clusters of clusters”), and a fairly homogeneous *distributed* fainter population. This is consistent with two main modes of star formation: localized cluster formation from dense molecular cores, and more widely spread star formation from smaller condensations (e.g., “pillars” eroded by the hydrodynamical feedback from winds and/or supernova explosions from massive stars ($M_* > 8M_\odot$), as in the Eagle Nebula (Guarcello et al. 2010; Flagey et al. 2011). The various clusters, as well as the distributed young stars in Carina nebula, also show a large spread in ages (~ 1 -10 Myr depending on the location within the nebula).

Therefore, it is now clear, in particular from X-ray observations, that a *large-scale* picture of young clusters, and not only of a small area around their brightest members, is essential to reliably disentangle age and membership effects – in particular the spatial mixing of stars having different formation histories (i.e., originating in distinct clusters or born via various feedback mechanisms at different epochs).

The above discussion raises crucial issues on star formation in clusters: What is the “real” membership of a cluster? And, which are the youngest and oldest member stars? The answer to the former is needed to build a reliable mass distribution and the latter to determine the global age distribution, and hence the duration of star formation in a given region.

These issues are not restricted to massive star forming regions, but may apply to young clusters in general, hence fuel the ongoing debate on the duration of the star formation process (e.g., Palla 2011). Such a statement can be inferred for the CMa R1 star-forming region ($d \sim 1$ kpc) because it is a young complex, with a lot of molecular material still around, and star formation both finished and still ongoing, according to our previous results based on the wide field of *ROSAT* on the famous arc-shaped ionized nebula Sh2-296 (Gregorio-Hetem et al. 2009, hereafter Paper I). This nebula, of as yet unclear origin, comprises known young (~ 1 -5 Myr) clusters, including around

the famous binary (FU Ori-type + Herbig) star Z CMa. Figure 1 shows the two fields, covering more than ~ 2.7 deg 2 , where 98 X-ray sources were detected with *ROSAT*. A detection limit of $F_X = 5.0 \times 10^{-15}$ erg s $^{-1}$ cm $^{-2}$ ($\log L_X = 29.78$) was achieved in Field 1 (exposure time of 20ks), while observations in Field 2 were less sensitive because of a much shorter exposure (5 ks) ($F_X = 8.4 \times 10^{-15}$ erg s $^{-1}$ cm $^{-2}$; $\log L_X = 30$).

Paper I report the discovery of a previously unknown cluster of low-mass stars having ages up to ~ 10 Myr, called the “GU CMa cluster”, after the name of its brightest member. It is located away from dense molecular material, indicating that star formation has now ceased in its vicinity. In contrast, the existence of several younger clusters on the other side of the CMa R1 molecular cloud, including around Z CMa, has been known for some time as a result of previous surveys at various wavelengths (see review by Gregorio-Hetem 2008). With respect to the molecular cloud, the GU CMa cluster therefore lies opposite to the Z CMa cluster, in a region devoid of molecular gas. The age gradient in each cluster, and the similarity of the fraction of the intermediate-age populations (see Fig. 10 of Paper I) strongly suggests some degree of mixing between the two clusters. The young population in-between Z CMa and GU CMa (the “inter-cluster” region) could be really mixed (i.e., coming from two distinct clusters, mixing at their edges), or perhaps be indicative of the existence of an as yet unnoticed, distributed population on a large scale.

Results from Paper I motivated our group to propose new X-ray observations of CMa R1, more sensitive than those previously obtained with *ROSAT* in order to improve the identification of the entire young stellar population in this region. We have focused on the “inter-cluster” region between the GU CMa and Z CMa sub-groups (see *XMM-Newton* fields in Fig. 1) aiming to investigate if there is a mixing of their populations. Besides getting a more complete sample of the CMa R1 young stellar population we use the properties of X-ray and near-infrared emission of these sources to identify their nature and disentangle the scenario of star formation in this region.

The outline of the paper is as follows. In the next section, we describe the source detection and data reduction of the *XMM-Newton* observations, and the X-ray general properties are presented in Sect. 3. Section 4 is dedicated to the infrared analysis based on *2MASS* and *WISE* data. A comparative analysis between X-rays and parameters derived from the infrared is performed in Sect. 5. Section 6 summarizes the results of this work. The general picture of star formation in CMa R1, extending the results from Paper I, is discussed in Sect. 7 and the main conclusions are presented in Sect. 8. Finally, Appendix A gives details about the analysis of the *XMM-Newton* data and Appendix B gives the complete catalogue of X-ray sources.

2. Observational data

For this work, four fields (each about 30 arcmin diameter with some overlap) were observed with the *XMM-Newton* satellite. These fields are located (Fig. 1): inside the arc-shaped ionized nebula, next to Z CMa - *Field E* (East); around GU CMa - *Field W* (West); and between both - *Field C* (Center) and *Field S* (South). The central coordinates from each field are given in Table 1. These observations were performed with the EPIC cameras (MOS1, MOS2 and PN) in full frame mode with medium filter. The C, W and S fields had an exposure time without background corrections of about 30 ks while field E had 40 ks.

These observations were analyzed with the *XMM-Newton Scientific Analysis System* (SAS) version 11.0.0 software. The calibrated and concatenated events lists were obtained by *epproc* and *empproc* tasks applied to PN and MOS raw data, respectively. Fields E, W and S were affected by high background activity, mainly in observations of the PN camera. In order to maximize the signal-to-noise ratio of weak sources we created lists of clean events using the standard procedure for EPIC cameras that filters the background, removes flares, as well as bad pixels, bad events and reduces noise¹. The good time intervals (GTI) of these observations are presented in Table 1.

Table 1. Observing log for the *XMM-Newton* observations of CMa R1.

Field name	ID Obs.	α (J200)	δ (J2000)	GTI (ksec) ^(a) PN - MOS
CMa cluster East	0654880201	07 04 18.3	-11 27 24.0	32 - 35
CMa cluster Center	0654880101	07 02 58.4	-11 34 44.7	30 - 32
CMa cluster South	0654880401	07 02 29.5	-11 47 12.4	28 - 32
CMa cluster West	0654880301	07 01 23.0	-11 19 56.6	28 - 32

(a) Good time interval from *XMM-Newton* observations.

The source detection was performed in two steps: individually for each of the three EPIC cameras, and merging them. In both cases, the detection was made in the three energy bands defined by Barrado et al. (2011): soft - $S_{B2011} = 0.5 - 1.0$ keV, medium - $M_{B2011} = 1.0 - 2.0$ keV and hard - $H_{B2011} = 2.0 - 7.3$ keV. In order to distinguish young stars from field objects, different energy bands were tested and these were chosen because they are more efficient for the detection of (thermal) stellar sources. The images from the three cameras were created in each of these bands and also in the full energy range (0.5 - 7.3 keV). The right panel of the Fig. 1 shows a combined image obtained with EMOSAIC task, illustrating the three energy bands detections in PN+MOS images: S_{B2011} (red), M_{B2011} (green) and H_{B2011} (blue).

¹ See the SAS thread at http://xmm.esac.esa.int/sas/current/documentation/threads/EPIC_filterbackground.shtml.

As a first step, the data from the three EPIC cameras were analyzed separately, by using the SAS metatask EDETECT_CHAIN for source detection in each detector. This metatask creates exposure maps used to correct the images for the quantum efficiency, filter transmission and mirror vignetting. It also provides detection maps that are used in order to perform sliding box detection using locally estimated background. These sources are masked and background maps are created. Then, the metatask performs a second detection of sources using the background map and derives the parameters by a maximum likelihood method, for each source. In order to explore softer energy bands, this procedure was also applied only to the PN data considering the energy bands suggested by Hasinger et al. (2001) as more efficient to detect (non-thermal) extragalactic sources: $S_{H2001} = 0.2 - 0.5$ keV, $M_{H2001} = 0.5 - 2.0$ keV and $H_{H2001} = 2.0 - 4.5$ keV. However, the tests exploring these softer energy bands turned out to be less efficient for the detection of (thermal) stellar sources. For this reason we adopted 0.5 keV as lower limit.

As a second step, the images (corrected by exposure map) were divided by the effective area of the respective detector, in order to take into account the differences in efficiency of the EPIC-PN and EPIC-MOS detectors. (Then, with the EMOSAIC task, a combined image was created from these images, for each energy band.) Finally, the source detection was performed from combined image using the EMOSAICPROC metatask, that works similarly to the EDETECT_CHAIN taking into account the merged data from different observations and, instruments improving the source statistical significance and enabling detections of weak sources. However, this task considers only sources present in all combined instruments. A double check was applied in the individual images, searching for sources that were missed in the second step due to placement problems, like falling outside of the field-of-view (FOV), inside a bad column or near to a gap of one or more of the instruments. In both cases the detection threshold was of maximum likelihood $ML \geq 15$. Some sources were detected in two fields, because fields E, W and S are overlapping field C, and in this case we chose the sources with the highest signal-to-noise ratio.

The detection procedure has provided a catalogue containing 387 sources: 84 are in Field C, 187 in Field E, 79 in Field W, and 37 in Field S. 351 of them were detected using the merged images of all three cameras, and 36 were detected by only one or two cameras. Table B.1 (Appendix B) lists the X-ray detections and parameters for all sources in the four fields studied. These parameters are: coordinates (J2000), maximum likelihood (ML) of source detection, count rate (CR) in the total energy band (0.5 - 7.3 keV), and hardness ratios $HR1_i = (M_i - S_i)/(M_i + S_i)$ and $HR2_i = (H_i - M_i)/(H_i + M_i)$. Here, S_i , M_i and H_i are the energy bands defined above, where the index i is related to the energy band ranges defined by B2011 and H2001.

Light curves and spectra were extracted only from EPIC-PN data, using the standard SAS routines^{2,3}. There are 47 sources in MOS 1/2 FOVs only, but none is bright enough for extraction of spectra and light curves. In both procedures the source and background regions were chosen by visual inspection, for each source. For the light curves we adopted the B2011 full energy range (0.5 - 7.3 keV) and time bins of 1000 sec. The spectra were obtained in the full standard energy range (0.2 - 10 keV) suggested by SAS and were analyzed using XSPEC version 12.7.1.

² <http://xmm.esac.esa.int/sas/current/documentation/threads/timing.shtml>

³ http://xmm.esac.esa.int/sas/current/documentation/threads/PN_spectrum_thread.shtml

3. Results on X-ray properties

The X-ray data give us information related to the nature of the source, inferred from hardness ratios (HRs) diagrams; parameters derived from spectral analysis, and from the light curve. Appendix A gives more details on how these parameters were obtained from EPIC/PN data.

From HRs diagrams analysis, based on B2011 and H2001 energy bands, we could classify 194 sources by comparing their X-ray emission with two model grids: thermal plasma, APEC (Astrophysical Plasma Emission Code, Smith et al. 2001) and a power-law (PWL)⁴ distribution, both multiplied by an absorption photoelectric model (PHABS)⁵. The sources that are compatible only with the APEC grid were classified as stellar objects, only 1/181 (0.5%) of them do not have IR counterpart. The sources compatible with a power-law may have another origin, probably extragalactic or perhaps compact objects. There are 195 sources that we call “undefined”, 47 of them can be fitted by either model (APEC or PWL), and 148 by neither. According to the results from the infrared (*2MASS+WISE*) data analysis (see Sect. 5), we suggest that 84 sources remain as undefined objects: 23 probably are foreground stars, and 17 have counterparts that are too faint (bad quality data), without confident classification. The other 44 undefined sources (11% of the *XMM-Newton* sample) do not have *2MASS* data, probably are background objects, which is in agreement with the expected 10% of contamination, at this level of sensitivity, mainly due to extragalactic sources (Getman et al. 2005b).

Table 2. Source classification based on X-ray emission.

	Stellar ^a	Other ^b	Undefined	
Field	APEC	PWL	(APEC + PWL) ^c	None ^d
E	102	7	22	56
C	39	-	12	33
S	9	1	6	21
W	31	3	7	38
Total	181	11	47	148

(a) Sources fitted by APEC models; (b) Sources fitted by Power-Law models; (c) Undefined sources: fitted by both models; (d) Undefined sources: fitted by neither model.

3.1. Light Curves and Spectra

Magnetically active stars, including T Tauri stars, typically show variable X-ray emission, for example, due to *flare-like* events varying from few minutes (< 30 min) to few hours (> 8.5h) and involving a large release of energy (10^{32} to 10^{35} erg/s, see Table A.1) (Feigelson & Montmerle 1999; Favata & Micela 2003; Güdel 2004; Stelzer et al. 2007). In young stars, particularly T Tauri stars, the light curves of these events appear with different shapes (e.g., Favata et al. 2005; Wolk et al. 2005; Franciosini et al. 2007; Stelzer et al. 2007; López-Santiago et al. 2010).

Within our four ~ 30 ks exposures, 13 sources presented *flare-like* events, which we identified using the definition of a flare adopted from Franciosini et al. (2007) and Wolk et al. (2005), as described in Appendix A.2, which also presents all the light curves and flare parameters for these sources. The

⁴ <https://heasarc.gsfc.nasa.gov/xanadu/xspec/manual/XSmodelPowerlaw.html>

⁵ <https://heasarc.gsfc.nasa.gov/xanadu/xspec/manual/XSmodelPhabs.html>

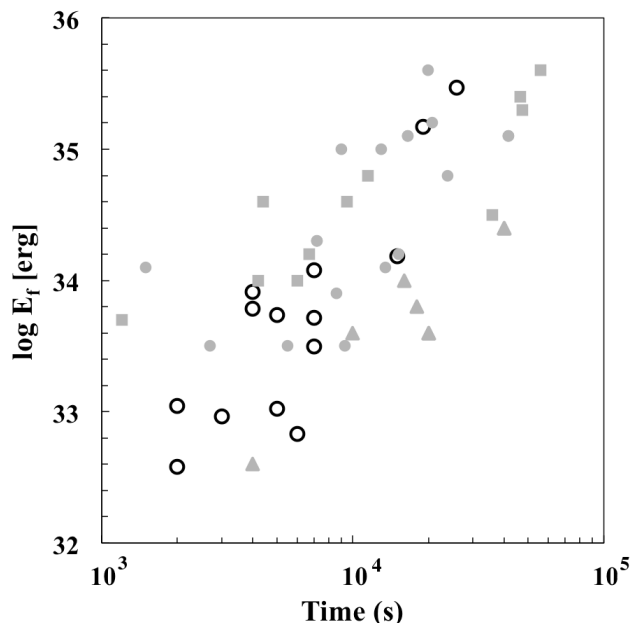


Fig. 2. Energy (E_f) and duration (T_f) of X-ray flares on CMA R1 sources (open circles), compared with those observed on members of *Taurus Molecular Cloud* (Stelzer et al. 2007), where Classical- and Weak- T Tauri are respectively represented by filled circles and squares. Filled triangles show young stellar objects associated with the η *Chamaleontis* cluster (López-Santiago et al. 2010).

characteristics of *flare-like* events in this work are similar to T Tauri stars of the *Taurus Molecular Cloud* (e.g., Stelzer et al. 2007), or young stellar objects from the η *Chamaleontis* cluster (López-Santiago et al. 2010). This similarity is shown in Fig. 2 that compares the energy and flare duration for our sample and these other regions.

In spite of the poor signal-to-noise ratio, we could perform the spectral fits of low resolution integrated spectrum for the whole exposure of some sources. The hydrogen column density, plasma temperature and flux for non-flaring sources were obtained by fits of PHABS \times APEC models for 21 sources, adopting metallicity $Z = 0.2 Z_{\odot}$, as appropriate for low-mass stars (see details in Appendix A.1). These spectra and parameters are presented in Appendix A.3. Their average hydrogen column density, $N_H = 1.8 \pm 1.5 \times 10^{21} \text{cm}^{-2}$, corresponds to an extinction $A_V = 0.9 \pm 0.7$ mag, by adopting $N_H/A_V = 2.1 \times 10^{21} \text{cm}^{-2}$ (e.g., Vuong et al. 2003). This value is compatible with $A_V = 1.0$ mag adopted in Paper I for CMA R1 and it is inside the range in which most of the sources are compatible with APEC model grids. The coronal temperatures, varying from 0.5 to 2.1 keV ($6.7 < \log T(\text{K}) < 7.4$), are also compatible with those found in other star formation regions like σ Orionis, η *Chamaleontis* (López-Santiago & Caballero 2008; López-Santiago et al. 2010) and the *Pipe Nebula* (Forbrich et al. 2010). Note that this means a low-extinction region, if compared with the minimum values for N_H corresponding to $A_V = 0.4$ for the foreground extinction in the direction of CMA R1, computed from the large-scale extinction models by Amôres & Lépine (2005), $N_H = 5.9 \times 10^{21} \text{cm}^{-2}$ from LAB Map (Kalberla et al. 2005) and $6.9 \times 10^{21} \text{cm}^{-2}$ from DL Map (Dickey & Lockman 1990).

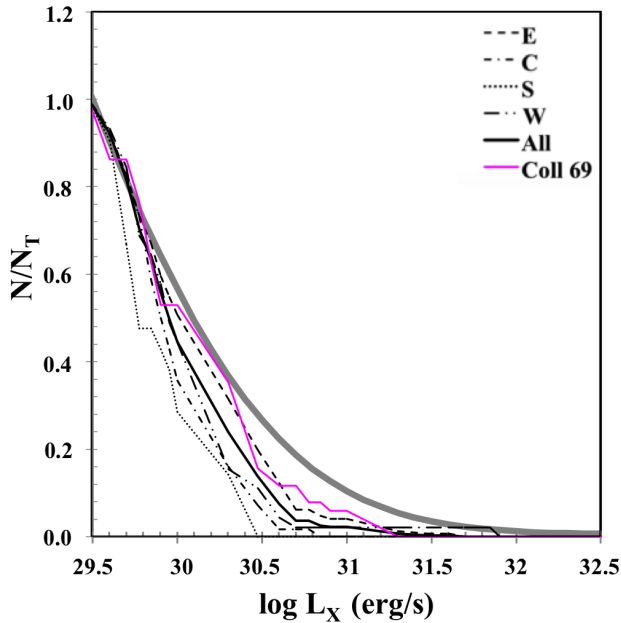


Fig. 3. Cumulative distribution of X-ray luminosities for sources in CMa R1 (black lines) and Collinder 69 (Barrado et al. 2011, magenta line). A thick grey line shows the log-normal distribution with $\mu=29.3$ and $\sigma=1$ proposed by Feigelson et al. (2005).

3.2. X-ray fluxes and luminosities

Based on the flux derived from the spectral fits of the brightest sources, we obtained the energy conversion factor (ECF) from the correlation between count-rate and flux. The linear fits of these parameters gives a mean value of $ECF = (1.60 \pm 0.04) \times 10^{-12} \text{ erg cm}^{-2} \text{ cts}^{-1}$ compatible with $ECF = 1.56 \times 10^{-12} \text{ erg cm}^{-2} \text{ cts}^{-1}$ calculated by PIMMS⁶ for a 1-T thermal model adopting the mean values for plasma temperature and N_H , derived from the EPIC/PN spectra (see Sect. 3.1).

The X-ray luminosities (L_X) were derived from the fluxes for all the 340 sources detected by PN camera, by adopting a distance of $d = 1 \text{ kpc}$ for CMa R1 (Shevchenko et al. 1999; Kaltcheva & Hilditch 2000, Paper I). Figure 3 shows the cumulative L_X Function ($L_X F$) derived for each field. As further discussed (Sect.5), the presence of possible non-members contributes with low levels of X-ray emission, not affecting the $L_X F$. A thick line shows $L_X F$ for all sources, compared to the 5 Myr-old cluster Collinder 69 (Barrado et al. 2011) represented by the magenta line in Fig. 3⁷. For both samples, which data have similar sensitivity, the $L_X F$ cumulative distribution was derived taking into account detected sources with $\log L_X(\text{erg/s}) > 29.5$. As a guidance, we add in Fig. 3 the log-normal distribution with $\mu=29.3$ and $\sigma=1$, the “Universal X-ray luminosity function” proposed by Feigelson et al. (2005). The differences on the distribution are found in the high luminosities end, mainly due to the low number of massive stars in our sample. This distribution is similar to the results for other low-mass clusters, as Serpens and NGC 1333, for instance, discussed by Günther et al. (2012).

⁶ <http://heasarc.gsfc.nasa.gov/cgi-bin/Tools/w3pimms/w3pimms.pl>

⁷ Collinder 69 is a 5 Myr cluster for which count rate and hardness ratios were estimated by using the same energy range that was adopted by us. This similarity of studying method was the reason for comparing the X-ray properties of our sample with this specific cluster.

4. Analysis of infrared properties

The characterization of the X-ray sources needs to be complemented by observational data obtained in other wavelengths. For instance, Fernandes et al. (2015) performed with the *Gemini South telescope* a spectroscopic follow-up of optical counterparts for a partial sample of the *XMM-Newton* stellar sources associated with the Sh 2-296 nebula. Among 58 candidates, they found 41 confirmed T Tauri stars and 15 possible PMS stars (including intermediate-mass stars). Almost 50% of the young stars have less than $1 M_\odot$ and 35% have masses between $1-2 M_\odot$. While half of their sample has an age of 1-2 Myr or less, only a small fraction (<10%) shows evidence of IR excess indicating the presence of circumstellar disks. In comparison with other young star-forming regions (e.g., Haisch et al. 2001; Hernández et al. 2008; Fedele et al. 2010), this is a very low fraction of disk-bearing stars.

In order to expand the search for disk candidates among the X-ray sources associated with CMa R1, we analyse the near-infrared (NIR) counterparts of these sources using available data in the *2MASS* and *Wide-field Infrared Survey Explorer (WISE)*; Wright et al. 2010) catalogues. The method used to estimate the infrared properties is described in Sect. 4.1, where we identify the NIR counterparts based on *2MASS* data, and use colour-colour and colour-magnitude diagrams to determine mass and age of the candidates. In the remainder of this section, we describe the IR classification (Sect. 4.2) determined with data from the *AllWISE* catalogue; the selection of a “best sample”, by adopting mass and age criteria (Sect. 4.3); the analysis of mass function (Sect. 4.4) and age distribution (Sect. 4.5).

4.1. Near-infrared counterparts

We selected NIR counterparts by searching the *2MASS* catalogue (Cutri et al. 2003) for candidates located less than $10''$ away from the nominal X-ray source positions. No counterpart was found for 45 sources. Candidates for which the distance seems to be incompatible with the cloud were disregarded. In the colour-magnitude diagram (see Fig. 4), these sources appear below the Main Sequence, indicating they probably are field stars.

The complete list of NIR counterpart candidates is given in Table B.2, but we consider as reliable only those with AAA flags in the *2MASS* catalogue, *i. e.*, magnitudes with high signal-noise ratio ($S/N > 10$), low errors ($< 0.1 \text{ mag}$) and above the completeness limit ($J < 15.8$, $H < 15.1$ and $K_s < 14.7$) ensuring good photometric quality (Lee et al. 2005). Table 3 gives the number of X-ray sources for each field and the corresponding number of their reliable NIR counterparts. Almost all are found less than $5''$ away from the centroid of the X-ray emission. This value has been used typically as a good estimate of the effective radius within $\sim 90\%$ confidence of the uncorrected positions (López-Santiago & Caballero 2008; Watson et al. 2003).

In total, we selected 340 reliable NIR counterparts to 290 X-ray sources, among them 46 have multiple counterpart candidates. Following Santos-Silva & Gregorio-Hetem (2012), we compare their positions in the colour-colour diagram (Fig. 4 left) with theoretical curves of the zero age main-sequence (ZAMS) from Siess et al. (2000)⁸; giants (Bessell & Brett 1988). Figure 4 (left) also includes an arrow that represents the reddening vector of $A_V = 2 \text{ mag}$ (Rieke & Lebofsky 1985), the T Tauri stars locus (Meyer et al. 1997), and the regions defined by Jose et al. (2011)

⁸ <http://www.astro.ulb.ac.be/~siess/pmwiki/pmwiki.php/WWWTools/Plots>

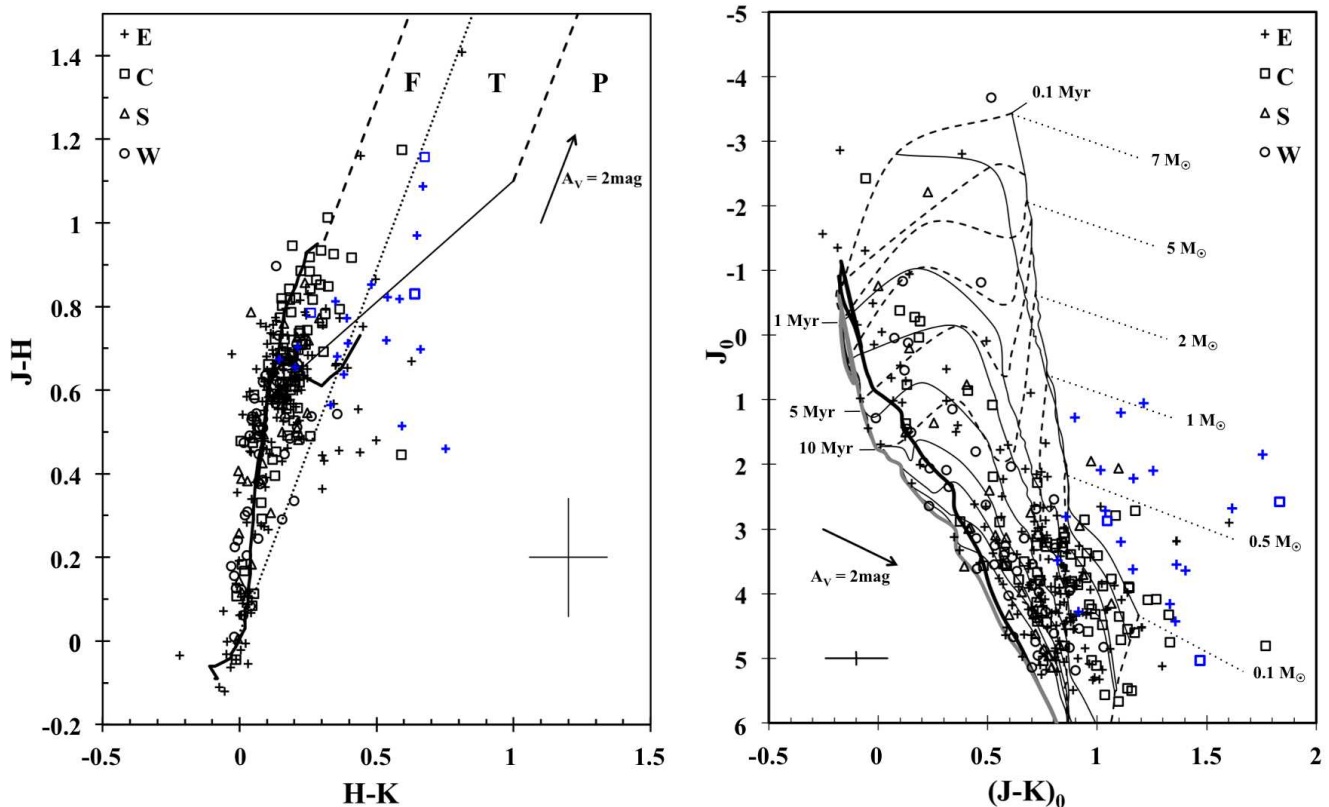


Fig. 4. *Left:* Colour-colour diagram for all 340 2MASS counterparts of X-ray sources found in fields E, C, S and W. Blue symbols represent disk-bearing (Class I and II) stars classified in Sect. 4.2. The ZAMS and the locus of giant stars are indicated by thick lines, while the locus of T Tauri stars is represented by a thin line. Dotted and dashed lines show reddening vectors. *Right:* Colour-magnitude diagram showing the isochrones 0.2, 1, 5, 10, 15, 20 Myr and ZAMS (full lines), early Main Sequence (grey thick line) and evolutionary pre-MS tracks 0.1, 0.5, 1, 2, 3, 4, 5, 6 and 7 M_{\odot} (dashed line) from Siess et al. (2000).

Table 3. Number of sources with one (1) or more (2, 3) 2MASS counterparts.

Field	1	2	3	Total X ^a	Total IR ^b
E	121	30	2	153	187
C	53	10	1	64	76
S	23	1	1	25	28
W	47	1	-	48	49
Total	244	42	4	290	340

(a) Total number of X-ray sources with 2MASS counterparts for each observed field; (b) The sum of NIR counterparts, by considering single and multiple candidates.

according to the NIR excess: stars with accretion disks are expected to be found in region “T” (Classical T Tauri stars: CTTS) and Class I protostars appear in region “P”. Field stars and diskless T Tauri stars (Weak T Tauri stars: WTTS), having little or no excess, are mainly located in region “F”. It can be noted that most of the counterparts are found in region F and/or near the ZAMS, indicating a low level of NIR excess for these sources.

Figure 4 (right) shows the colour-magnitude diagram (CMD) with reddening corrections made according to the extinction law from Cardelli et al. (1989) for $A_V = 0.9$ mag which is the mean value in the visual extinction map⁹ and corresponds to the average hydrogen column density ($N_H = 1.9 \times 10^{21} \text{ cm}^{-2}$), obtained

from the X-ray spectrum fits (see Sects. 3.2 and A.3). The absolute magnitudes were estimated by using the distance modulus $m_J - M_J = 10 \text{ mag.}$, according to the cloud distance adopted in Sect. 3.1 ($d = 1 \text{ kpc}$).

The CMD shows theoretical isochrones for 0.2 to 20 Myr, the ZAMS, and 0.1 to 7 M_{\odot} evolutionary tracks. We also included the “Early Main Sequence” model that represents the last stage of evolution in the Siess et al. (2000) calculations (see Sect. 4.3). Mass and ages were estimated from comparison with the theoretical curves by interpolating the models, except for candidates appearing rightwards of the models in the CMD. According to the *WISE* data (analysed in Sect. 4.2), several of these candidates are Class I or Class II objects (see blue symbols in Fig. 4).

4.2. Classification based on *WISE* data

Among our list of 340 NIR counterparts (Table 3), only 272 are also listed in the *AllWISE* data release (Cutri & et al. 2013). However, we focused the infrared classification on 157 objects with reliable *WISE* photometry, i.e., 115 sources with errors greater than 0.2 mag in Bands 1 ($3.4 \mu\text{m}$) and 2 ($4.6 \mu\text{m}$) and upper limits in Band 3 ($12 \mu\text{m}$) were not considered. In a first analysis, we looked for IR excess by combining the 2MASS and *WISE* data in the K-[4.6] vs. H-K diagram.

The distribution of the 157 selected sources in this diagram revealed 34 objects with $K-[4.6] > 0.7 \text{ mag}$, which is an indication of IR excess (Cusano et al. 2011; Fernandes et al. 2015) that

⁹ L. Cambr esy, private communication; (see Cambr esy et al. 2002).

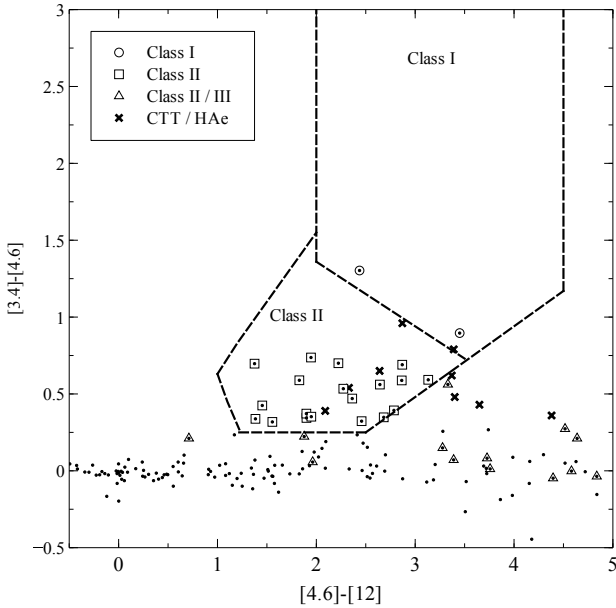


Fig. 5. *WISE* colours of counterparts of X-ray sources (dots), compared with the locus of Class I and Class II proposed by Koenig & Leisawitz (2014). Open symbols show objects classified according to their infrared excess, while crosses indicate known disk-bearing stars (Fernandes et al. 2015).

could be due to the presence of a disk. This excess is in agreement with the colours of T Tauri and Herbig Ae/Be stars associated with Sh2-296 (Fernandes et al. 2015), which were included in this analysis (indicated by crosses in Fig. 5) as representative of known disk-bearing stars.

A more conclusive infrared classification was obtained by using the criteria presented by Koenig & Leisawitz (2014) to classify YSOs based on *WISE* colours. Figure 5 shows the $[3.4]-[4.6]$ vs. $[4.6]-[12]$ diagram and the Class I, II and III regions (dashed lines) defined according to the distribution of objects associated to Taurus Molecular cloud (Rebull et al. 2010). This analysis provided the separation of the 34 candidates, which show IR excess ($K-[4.6] > 0.7$ mag), in different types: 2 Class I; 19 Class II; and 13 Class II/III. The other 123 NIR counterparts having good quality of data, but not showing IR excess, are considered Class III. Finally, the remaining 115 NIR counterparts with bad quality of *WISE* data, to which we could not assign an infrared classification, are marked with “?” in the last column of Table B.2.

As we discuss further in Sect. 5.3, in spite of the youth of the sample associated with CMa R1, a low fraction ($21/157 < 14\%$) of disk-bearing stars (Class I and Class II) is found, reinforcing the previous partial results of Fernandes et al. (2015).

4.3. Defining a “best sample” of *XMM-Newton* sources

As a consequence of the dependence of X-ray luminosity on stellar mass, the selection of our sample naturally imposes a mass detection threshold. More precisely, due to our *XMM-Newton* detection limit (see below, Sect. 5.2), and in comparison with other X-ray observations of star-forming regions, our list of X-ray sources is incomplete for low-mass stars. In order to statistically improve the analysis of the 2MASS data, we have adopted conservative criteria searching for NIR sources, which restrict

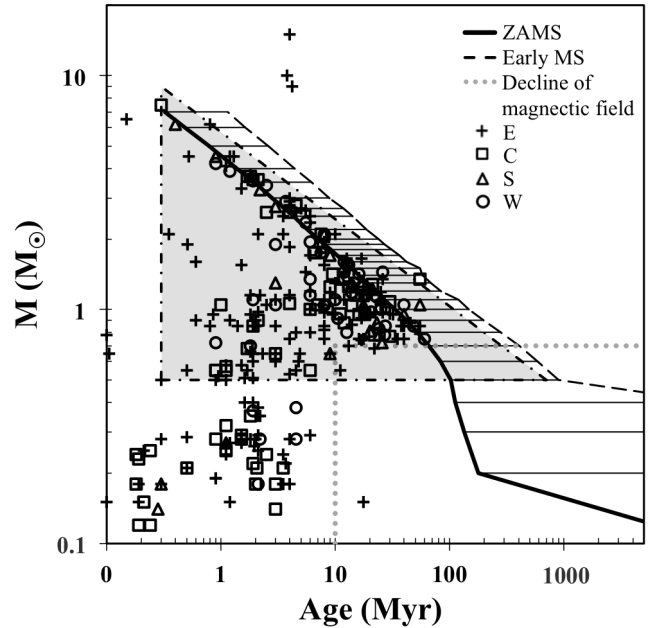


Fig. 6. “Best sample” of X-ray sources based on estimates of masses and ages for 340 2MASS counterparts (see Table B.2), which takes into account the incompleteness of our sample below $\sim 0.5 M_{\odot}$, are present in the grey area. The empty area between dotted lines corresponding to the mass range $0.5 - 0.7 M_{\odot}$ and age > 10 Myr is interpreted as the decline of magnetic activity of low-mass young stars with age (see Sect. 7.2).

the counterparts selection to the reliable candidates where the source sample is complete, i.e., our so-called “best sample”.

The selection criteria are based on Fig. 6 that compares masses and ages of our candidates with theoretical values interpolated from the zero age main-sequence (ZAMS) and Early Main Sequence evolutionary tracks from Siess et al. (2000). According to these authors, this last track is more representative of stars with mass $> 1.2 M_{\odot}$ having reached equilibrium after the CNO cycle. This is the last stage of evolution in the Siess calculations, occurring after the ZAMS, and corresponds to the end of deuterium burning, when the nuclear energy production switches to hydrogen burning and starts to provide all the stellar luminosity. Considering that our sample is complete only in the ranges of $0.5 < \text{mass} (M_{\odot}) < 9$ and $0.3 < \text{age} (\text{Myr}) < \text{ZAMS}$, when taking into account the *XMM-Newton* detection limit for CMa R1 (see Sect. 5.1 and Fig. 10), our final “best sample” is highlighted by the hatched region in Fig. 6. By adopting this criterion, the NIR analysis is restricted to 225 counterparts (comprising multiples): 122 of them belong to field E, 37 to field C, 23 to field S, and 43 to field W.

It is important to stress that the other sources (appearing outside the hatched region of Fig. 6) remain as possible counterparts of the X-ray sources. They were removed of the present analysis only to obtain more conclusive results based on a limited, but complete sample (in a given range of mass and age), rather than on a larger, but incomplete, sample, as explained above.

4.4. Mass Function

Considering the four *XMM-Newton* fields together, we find that over 75% of stars have masses $0.5 < M(M_{\odot}) < 2$, together

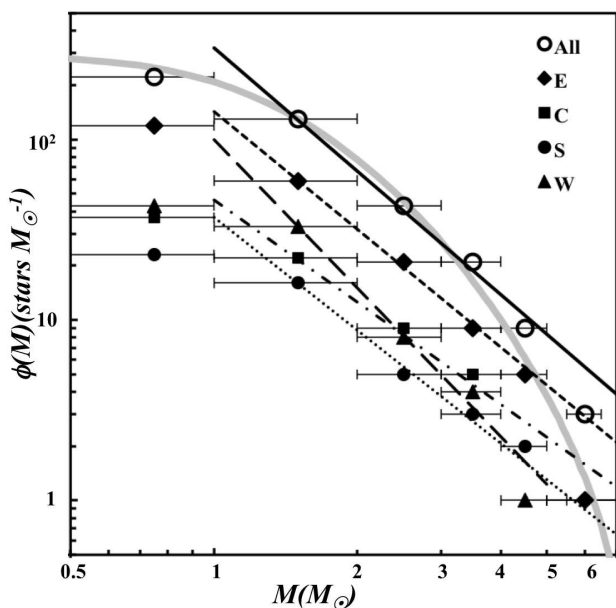


Fig. 7. Observed mass distribution indicated by different symbols with error bars. The lines represent the power-law fitting of mass function $\phi(M)$ for $M > 1 M_{\odot}$ of individual *XMM-Newton* fields: E (dashed), C (dotted), S (long dashed) and W (dotted), and considering the entire “best sample” (black). The grey line shows the theoretical log-normal curve proposed by Chabrier (2005) with $\mu = 0.3$ and $\sigma = 0.6$.

with a few massive stars. In order to examine differences and similarities in the mass distribution of each field we calculate their cumulative mass function, which we write in the form $\phi(M) \propto M^{-(1+\chi)}$. According to Krumholz (2014), for young stellar clusters the mass function is essentially identical to the Initial Mass Function (IMF), so we can directly compare our mass functions with theoretical models of IMF, such as Salpeter (1955), Kroupa (2001) and Chabrier (2005). According to these authors, the IMF for stars with masses larger than $1 M_{\odot}$ can be represented by a power-law function with a slope $\chi \sim 1.35$, while for low-mass stars Kroupa (2001) suggests broken power-law functions with $\chi = 1.3$ ($0.5 - 1 M_{\odot}$) and $\chi = 0.3$ ($0.08 - 0.5 M_{\odot}$). Chabrier (2005) suggests a log-normal distribution with peak at $\sim 0.2 - 0.3 M_{\odot}$ and a dispersion of $\sim 0.5 - 0.6 M_{\odot}$. A good discussion about the differences among these models is presented by Bastian et al. (2010).

Figure 7 shows the observed $\phi(M)$ and the slopes obtained for each *XMM-Newton* field. Aiming to compare our results with the theoretical power-law function (valid for $M > 1 M_{\odot}$), the fit to the slope of $\phi(M)$ does not include stars with $0.5 < M(M_{\odot}) < 1$. The mean value of $\chi = 1.27 \pm 0.09$ obtained for the entire sample is consistent with Salpeter’s IMF and agrees with the models of Kroupa (2001) and Chabrier (2005), although it differs somewhat from the values estimated for each field: 1.21 ± 0.11 (Field E), 0.97 ± 0.14 (Field C), 1.08 ± 0.09 (Field S) and 1.73 ± 0.14 (Field W). Since our “best sample” is complete for $M > 0.5 M_{\odot}$, the turnover below $1 M_{\odot}$ is real and consistent with the log-normal distribution proposed by Chabrier (2005) as shown in Fig. 7. In this case, the theoretical curve, a log-normal function with $\mu = 0.3$ and $\sigma = 0.6$, is compared with the distribution of all sources of the “best sample”.

Altogether, except for Field W which has a definitely steeper slope, all fields have mass function slopes compa-

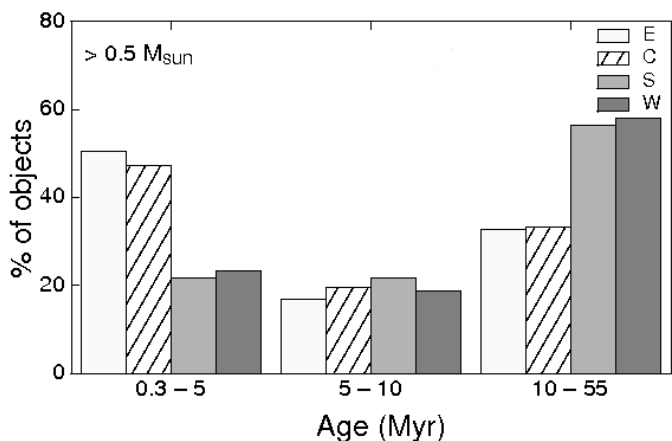


Fig. 8. Comparison of age distributions for each field, by considering three ranges of age.

table to those of other young stellar clusters studied by Santos-Silva & Gregorio-Hetem (2012), for instance: Collinder 205, Lyngå 14, NGC 2362, NGC 2367, NGC 2645, NGC 3572, NGC 3590, NGC 6178, Stock 13 and Stock 16.

4.5. Age distribution

The histograms in Fig. 8 show, for each field, the distribution of objects in three age ranges. The main differences are in Fields E and C where about 50% of the sources have ages between 0.3 and 5 Myr, while in Fields S and W more than 55% of the objects are between 10 Myr-old and the ZAMS. Even considering the 43 NIR counterparts that were discarded due to lack of age information (see Sect. 4.1), the distribution follows the same trend, since their NIR-excess suggests they probably are < 0.3 Myr. In this case, the fraction of sources with ages < 5 Myr in Fields E and C would be more than 60%, not affecting the distribution of Fields S and W.

Note that, although we discuss each field separately, it is important to keep in mind that this division is purely observational, being based on the selection of the *XMM-Newton* pointing directions. However, they do reflect to some extent different stellar populations, since the fields were selected on the basis of our previous *ROSAT* observations (Paper I). So the large differences apparent in the histogram of Fig. 8 are statistically significant and indicative of real differences in the stellar populations within the CMA R1 region. In particular, these results fully confirm and extend the age distribution obtained in Paper I, in which, in particular, the group next to CMA GU (age > 10 Myr) appears significantly more evolved than the group near Z CMA (age < 5 Myr), with a mixture of ages in between.

5. Comparison of X-ray and NIR properties

As described in the previous sections, X-ray and NIR data have revealed that most (79%) of the *XMM-Newton* sources are probable members of CMA R1. The combination of the results from both analyses can confirm their young nature. On the other hand, 21% of the *XMM-Newton* sample probably are field objects. Among them, 6% (23/387) have infrared counterparts that probably are foreground stars, and 4% (17/387) have counterparts that are too faint (bad quality data), without reliable classification. The other 11% of undefined sources (44/387) do not have

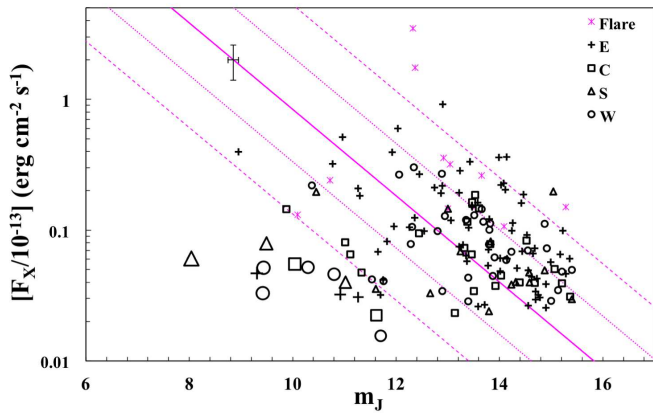


Fig. 9. X-ray fluxes (F_X) vs magnitude in 2MASS J band (m_J): full line presents the relationship $\log(F_X) = -9.8(\pm 0.4) - 0.33m_J$ similar to that obtained using *ROSAT* data in Paper I. Large symbols represent Herbig Ae/Be stars ($M > 2 M_\odot$). Dotted and dashed lines show 1σ and 2σ offset, respectively.

2MASS data, being classified as possible background objects. We have seen that the *XMM-Newton* error boxes may include multiple NIR counterparts, so we restrict the comparative analysis described in this Section to the 158 X-ray sources of our “best sample” that are associated with a single NIR counterpart.

5.1. X-ray flux vs. J-band magnitudes

Based on *ROSAT* sources detected in CMaR1, in Paper I a correlation between X-ray luminosities and absolute magnitude in J-band ($= 1.24\mu\text{m}$) was presented: $\log L_X = 31(\pm 0.4) - 0.33 M_J$, that is similar to the results for T Tauri stars associated with nearby clouds like Chamaeleon (Feigelson et al. 1993) and ρ Ophiuchi (Casanova et al. 1995). Compact stars and extragalactic objects are expected to appear above this correlation, since their X-ray emission is comparatively much more intense relative to their NIR luminosity. Herbig Ae/Be stars, which have lower levels of X-ray flux, when compared to their NIR emission, show the opposite, appearing below the T Tauri correlation, in spite of the age similarities for these two types of pre-main sequence stars.

Considering that 1 keV (the typical energy peak of our sources) and the J band coincidentally have almost exactly the same extinction cross-section (Ryter 1996), we opted for a direct comparison between X-ray flux and apparent J magnitude, avoiding inaccuracies due to errors on the extinction estimation that affects luminosity and absolute magnitude estimation.

In this case, the correlation given in Paper I can be expressed by $\log F_X = -9.8(\pm 0.4) - 0.33 m_J$, where F_X is given in $\text{erg s}^{-1} \text{cm}^{-2}$. A comparison of our sample with this correlation is presented in Figure 9, where the sources showing flares are highlighted. The error-bars shown in the top-left of Fig. 9 correspond to less than 30% of the flux and 0.1 in magnitude, which are representative of our “best sample”.

Most sources of our sample roughly follow the empirical correlation within 2σ deviation. Only seven sources have a larger deviation, but they are not real outliers. Three of them are associated with flare events, which is not unexpected since flares release a large amount of energy, resulting in a higher X-ray flux than that emitted by the source in quiescence, but are too hot to affect the NIR emission. The other four objects (three in Field

E and one in S) found above the correlation may be unresolved multiple systems with faint companions. In fact, one of them has been identified by Fernandes et al. (2015) as a binary system, in which both companions were classified as WTTS. The fainter star in the binary was not included in our sample of NIR counterparts due to the low quality of NIR data. Based on the number of X-ray sources with two or more NIR counterpart candidates, we estimate less than 8% (17/206) of possible (not confirmed) binaries in our “best sample”.

On the other hand, 13 sources lie below a 2σ deviation from the correlation because they have low F_X but high values of m_J . Large symbols are used to represent these sources that are more likely coinciding with the expected region for Herbig Ae/Be stars in Fig. 9. This hypothesis is reinforced by the high mass of these objects, that varies from 2.1 to $6.2 M_\odot$.

We conclude that, based on the correlation for T Tauri stars displayed in Fig. 9, all the sources in this sample can convincingly be considered as young stellar objects.

5.2. Masses and X-ray luminosities

The distribution of L_X as a function of mass was compared to that of other young clusters and star-forming regions such as the Orion Nebula Cluster (ONC; Preibisch et al. 2005), the Taurus Molecular Clouds (TMC; Güdel et al. 2007) and Collinder 69 (Barrado et al. 2011). A summary of lower limits of X-ray luminosities and fluxes, as well as target distances and exposure times of the X-ray observations used in this comparison are presented in Table 4.

Table 4. Limits in X-ray observations

	Flux ^(a) $10^{-15} \text{erg s}^{-1} \text{cm}^{-2}$	$\log(L_X)^{(b)}$	d ^(c) pc	Exp. Time ^(d) ks	Inst. ^(e)
Field E _{XMM}	2.5	29.48	1000	32	XMM
Field C _{XMM}	2.2	29.43	1000	30	XMM
Field S _{XMM}	2.4	29.46	1000	28	XMM
Field W _{XMM}	1.6	29.27	1000	28	XMM
Field 1 _{ROSAT}	3.6	29.78	1000	20	ROSAT
Field 2 _{ROSAT}	8.36	30	1000	5	ROSAT
ONC	0.042	27.01	450	838	Chandra
TMC	1.70	27.60	140	31 - 131	XMM
Collinder 69	5.22	29	400	28 - 37	XMM

(a) Flux limit of X-rays observations; (b) Luminosity limit; (c) Distance; (d) Exposure time; (e) Instrument used for observations.

The ONC and TMC are closer than CMa R1, and some of their X-ray observations were performed with longer exposure times. Therefore the capability to detect fainter sources results in a more complete sampling of the lower mass end of their population (see Table 4). For comparison, the detection limit of our sample is illustrated in Fig. 10.

The minimum flux detected in the other regions is 10 to 100 times lower than that of CMa R1, clearly suggesting the absence of faint X-ray emitters among our sample, which implies that a considerable number of low-mass stars ($< 0.5 M_\odot$) are below our detection limit, especially if we compare the masses and luminosities of sources in our sample with TMC objects.

It is interesting to note the differences and similarities on the $L_X F$ derived in Sect. 3.2 for each field compared to the Collinder 69 cluster considering the same mass range (see Fig. 3). The $L_X F$ for all the CMa R1 sources has slightly lower X-ray levels than Collinder 69, which has most of the members with 5 Myr and masses $< 2 M_\odot$. In this case, the differences in X-ray properties depend not only on the larger range of ages of our sample, but

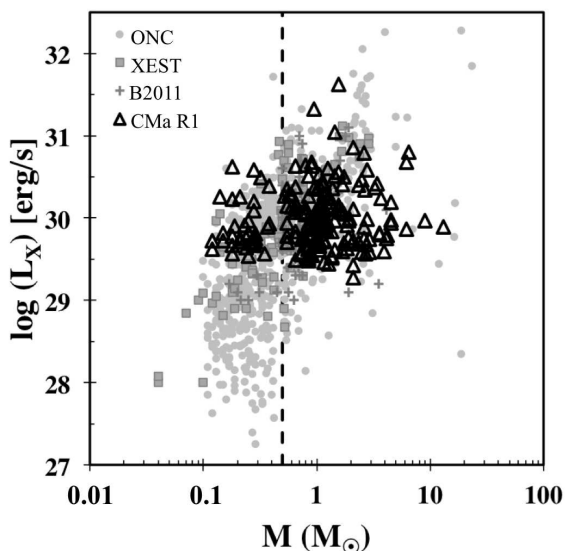


Fig. 10. X-ray luminosity vs. stellar mass for the sources in CMA R1 (black triangles) compared with T Tauri stars in other star forming regions: Orion Nebula Cluster (ONC), Taurus Molecular Cloud (TMC) and Collinder 69 (Coll69). The dashed line indicates the limit of mass adopted to define our “best sample”. The gap at 0.4 - 0.5 M_{\odot} is not real, but due to difficulties in interpolating models on this mass range.

also on the masses. As indicated in Fig. 9, intermediate-mass young stars tend to have lower X-ray emission when compared with the F_X vs. m_J correlation found for low-mass stars. This can also be seen by the relatively higher proportion of sources found in Field C (~19%), appearing below the 1σ correlation in Fig. 9, when compared to Field E fraction of sources (< 6%), which also reflects to the fainter $L_X F$ presented by field C. Since the fraction of young stars (< 5 Myr) is similar for both fields, it is not an age effect but differences on mass distribution. As shown in Fig. 7, there is a lack of stars more massive than $4M_{\odot}$ in field C, giving a less steep slope if compared with the mass distribution in Field E.

5.3. Comparison with the dust and dense gas distributions

As discussed in Sect. 4 there is a low fraction of stars with IR excess, which are those appearing to the right of the vector indicated by the dotted line in the $2MASS$ colour-colour diagram (see Fig. 4). When considering the whole sample of $2MASS$ counterparts only 8.5% (29/340) have a K-band excess. The analysis based on *WISE* data shows 22% (34/157) of the sample with $K-[4.6] > 0.7$ mag that we considered disk-bearing candidates, however only 2 of them were confirmed as Class I objects and 19 are Class II. This small number of Class I protostars and Class II T Tauri stars candidates in the *XMM-Newton* fields is also confirmed by a census of young stellar objects covering the whole CMA OB1 star forming region ($10^{\circ} \times 10^{\circ}$) performed by Fischer et al. (2016). These authors follow a slightly modified version of the criteria suggested by Koenig & Leisawitz (2014). Despite they use *WISE* colours similar to those adopted by us (Sect. 4.2), in the list of Fischer et al. (2016) a smaller number of disk-bearing stars, 1 Class I and 11 Class II, is found coinciding with the X-ray sources. Their census is not complete for the *XMM-Newton* surveyed area, probably due to their more restric-

tive criteria in excluding *WISE* sources that show any contamination flag.

The spatial distribution of the NIR counterparts is analysed in Fig. 11 to look for evidence of clustering. In spite of the fact that the fields observed with *XMM-Newton* were not meant to correspond exactly to physically separated clusters or stellar groups, their location turns out to reflect fairly accurately the spatial distribution of the sources as a function of position (in projection). Roughly, Field E contains sources located on the inner side of the cloud, Fields C and S contain sources distributed along the border of the visible nebula, while most of the Field W sources are outside the molecular cloud.

The position of the sources in Fig. 11 is also compared to the cloud gas distribution, revealed by ^{13}CO map¹⁰, where dense areas coincide with the dust distribution, (as seen in Fig. 1) indicated by the A_V map⁹. It can be noted that Field W is dominated by older objects (> 10 Myr) (circles), without preferential distribution. On the other hand, Fields E and C show a mixing of all age ranges as well as objects without well defined age (represented by crosses). In Field C, most of the younger objects (< 5 Myr) are within the area with the highest concentration of CO, while in field S younger objects are on the edge or outside the CO contours. In both cases we can see a segregation of ages, in which most of the older sources are to the right side, towards GU CMA, and younger ones are to the left side, near the edge of the nebula. However, young objects are also found in the “empty” area around GU CMA, while older ones are also found in the dense area around Z CMA, pointing to an apparent paradox in the history of star formation in the CMA R1 region.

It is interesting to note that about 70% of NIR counterparts with K-band excess, as well as all disk-bearing candidates found in Fischer et al. (2016), are distributed in regions with high ^{13}CO flux (> 20 Jy), which is also the location of dust concentration responsible for the extinction. Since a uniform value $A_V = 0.9$ mag has been adopted in the present work, it is possible that the reddening correction was too small for these sources. Several of them are located in the area of the BRC 27 and VDB RN92 clusters that have $A_V = 6.5$ and 4.4 mag, respectively (Soares & Bica 2002, 2003). A more detailed estimate of individual values of A_V could help us better determine the ages and masses for such embedded objects, and probably increase the sample of *bona fide* CMA R1 members. We defer such a study to a future paper.

6. Summary of the results

Our observations performed with *XMM-Newton* resulted in a sample of 387 X-ray sources (187, 84, 37 and 79 in Fields E, C, S and W respectively), 340 of them having one or more NIR ($2MASS$) counterparts.

In order to characterize the CMA R1 members, we made complementary use of the X-ray and NIR data: We compared the X-ray hardness ratios to a model grid for a hot thermal plasma and for power-law spectra that we simulated with XSPEC and we compared the NIR photometry to the isochrones from PMS evolutionary models.

Based on results from the X-ray analysis, summarized in Table 2, the sources were separated according their HRs: 47% are well reproduced by a thermal plasma (APEC model), as expected for stars, and 3% probably are extragalactic sources (power-law model). The other half of the sample could not be identified in one of these categories, because 12% are reproduced by both models and 38% are outside the grids. As described below, the

¹⁰ T. Onishi, private communication; (see Onishi et al. 2013).

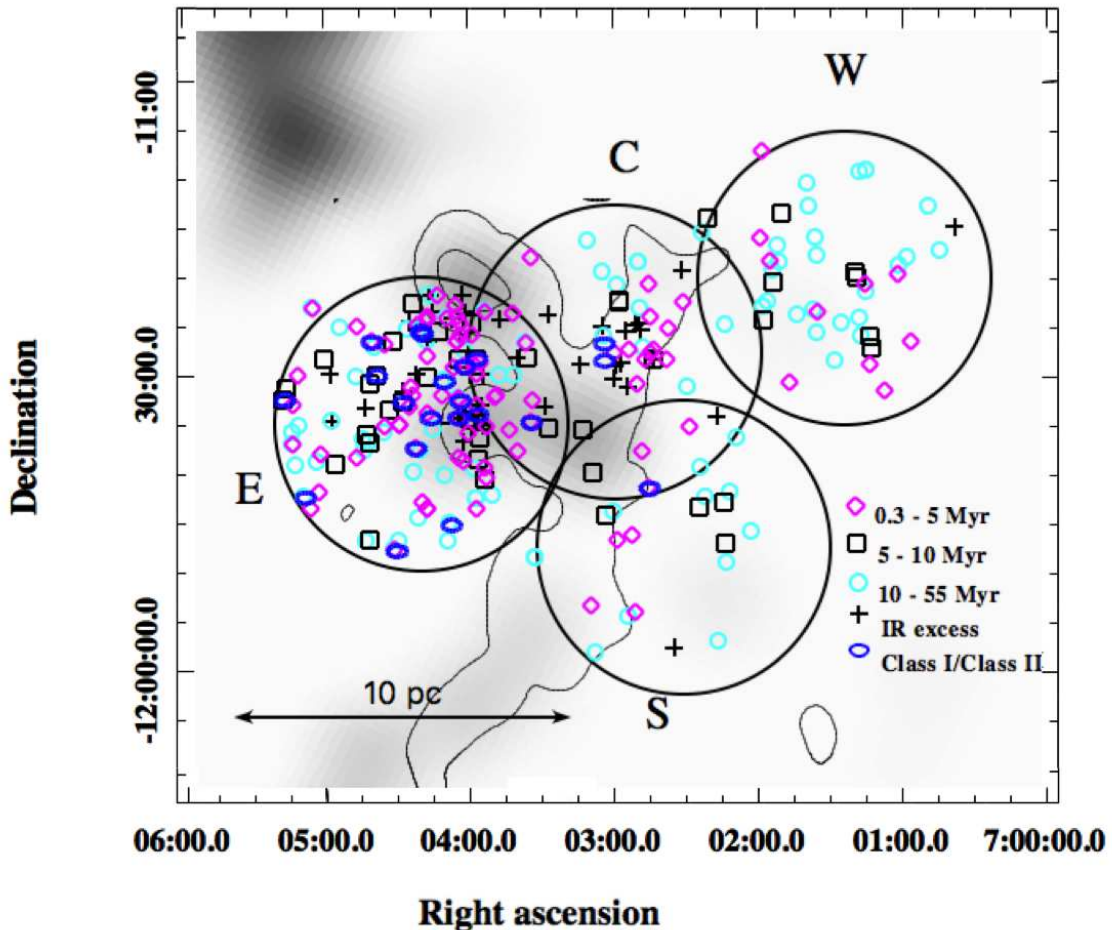


Fig. 11. Spatial distribution of NIR counterpart of X-ray sources as function of the age compared to a ^{13}CO map¹⁰ shown the grey image superimposed on $A_V > 2$ and 4 mag contours (the same as Fig. 1). The diamonds, squares and circles represent objects with less than 5 Myr, between 5 and 10 Myr, and more than 10 Myr respectively. The counterparts found outside of Siess et al. (2000) PMS isochrones are represented by crosses and disk-bearing candidates (see Sect. 4.1) are shown by blue ellipses. Black circles delimit the fields E, C, S and W.

numbers of probable members or field objects were refined in agreement with the analysis of NIR counterparts. Moreover we could obtain more X-ray properties of several sources through their light curves and spectra. About 13 sources show *flare-like* events and the 21 brightest sources had their plasma parameters determined by fits of the low resolution EPIC/PN spectrum with an APEC model. The results from the spectra of these bright sources were used to determine the energy factor conversion and consequently the X-ray luminosities.

Among the NIR counterparts, 225 were selected to define our so-called “best sample”. The fits of the mass distribution $\phi(M)$, assumed to be a power-law of the form $\phi(M) \propto M^{-(1+\chi)}$ gives a slope $\chi \sim 1.3 \pm 0.1$, for stars more massive than $1 M_\odot$, which is consistent with the Salpeter IMF and in agreement with theoretical and observational results from the literature. Almost no difference is found among the observed fields when comparing their individual mass function, except of Field W, which has a lower fraction of stars more massive than $4 M_\odot$, with respect to its fraction of low-mass stars, increasing its slope. Most of the younger sources (< 5 Myr) are present in Fields E and C, while about 60% of older sources (> 10 Myr) are in Fields W and S. All the fields have almost the same proportion ($\sim 20\%$) of objects with intermediated ages (5 – 10 Myr).

The comparison with the X-ray flux and J magnitude correlation, found for T Tauri stars or Herbig Ae/Be stars, was restricted to the 158 sources of our “best sample” having a single NIR counterpart. Most of them follow the F_X vs. m_J correlation, except for 13 below it, probably Herbig Ae/Be stars, as confirmed by their mass $2 < M(M_\odot) < 8$, and for 7 sources that are above this correlation: three are in a flaring state and four have anomalous light curves, meaning that two or more peaks of X-ray flux, followed by a decline, were detected when compared to the quiescent state.

Compared with other young stellar clusters, our sample shows a typical distribution of X-ray luminosities as a function of mass. However, the sample is incomplete for low-mass stars, mainly those that are faint X-ray emitters. Our survey could detect only objects having $\log(L_X [\text{erg/s}]) > 29.5$, which results in an apparent deficiency of young stars with masses $< 0.5 M_\odot$. Another possible cause for incompleteness is related to the fact that about 10% of the X-ray sources may be low-mass stars affected by high levels of visual extinction: most of them are located in the direction of dense regions of the ^{13}CO map¹⁰, which prevented estimates of mass and age in this case.

By combining the two methods, X-rays and NIR, we propose a classification of the *XMM-Newton* sources into 3 groups: (i) CMa R1 members – these sources are very likely associated to

Table 5. Number of CMA R1 candidate members.

Field	M ^a	P ^b	U ^c	Total
E	70	89	28	187
C	20	45	19	84
S	8	17	12	37
W	20	33	26	79
Total	118	185	84	387

(a) CMA R1 member; (b) Possible CMA R1 member; (c) Undefined sources.

the region because they have X-ray HRs compatible with a thermal plasma model and belong to our “best sample” of NIR counterparts; (ii) Possible CMA R1 members - these sources were considered young according to one of the methods only; (iii) undefined sources - objects for which we could not determine their origin by any of the methods, or sources rejected by at least one method. The number of classified sources in each group is shown in Table 5. Among the undefined sources there are 44 (11% of the total *XMM-Newton* sample) that we estimate to be extragalactic (background), due to the lack of NIR counterpart; 23 (6%) objects with NIR colours of field stars (foreground), while 17 (4%) with counterparts that have bad quality *2MASS* data, giving them an inconclusive classification.

The optical spectroscopy performed with *Gemini South* by Fernandes et al. (2015) covered 40 of our sources in Field E. Among the CMA R1 members (M) and possible members (P) classified by us, 22 and 18, respectively, were confirmed as PMS objects. Moreover, all Class I, II and III objects, based on *WISE* data, are also found among M and P sources of Table 5.

This agreement also proves the efficiency of the methods adopted in this work to identify the members of CMA R1.

7. Discussion

In order to obtain a comparative and wider view of the young stellar population in CMA R1, we include in the present discussion some additional objects selected from Paper I on the basis of their *ROSAT* observations.

A simple comparison of the spatial density of detected sources in both surveys gives an immediate appreciation on how much the sensitivity improved with the present *XMM-Newton* observations (yielding ~ 550 sources deg^{-2}) over the previous *ROSAT* results (~ 36 sources deg^{-2}). However, the *ROSAT* sources were detected in a larger field-of-view ($\sim 2.7 \text{ deg}^2$) while the total area covered by *XMM-Newton* for the present work is 5 times smaller ($\sim 0.7 \text{ deg}^2$).

An overview of the spatial distribution of the total number of 250 young stars selected as our enlarged “best sample” (225 *XMM-Newton* + 25 *ROSAT*) indicates that 171 (68%) are seen close to Z CMA, superimposed in the East side the of $A_V > 2$ mag contour shown in Fig. 12, while 79 are found in the West side of A_V contour, around GU CMA, in areas devoid of molecular gas ($A_V \sim 0.5$ mag). In the next sections, the location of the sources is discussed relative to their ages and masses as obtained in Sect. 4.1 for our sample and in Paper I for *ROSAT* sources, and to the distribution of dense gas, over a wider area than that covered by *XMM-Newton* alone.

7.1. Spatial distribution vs. stellar ages

With the purpose of investigating the spatial distribution of our sample of young stars relative to their age, Table 6 gives the num-

ber of *XMM-Newton* sources supplemented by *ROSAT* sources, separated in three age ranges, the same ones as in Fig 8: 0.3 - 5 Myr (“younger stars”), 5 - 10 Myr (“intermediate-age stars”), and 10 - 55 Myr (“older stars”). Based on these definitions, the fraction of $\sim 40\%$ of the younger stars observed by *XMM-Newton*, which is similar as that of the older stars, is thus in agreement with Paper I (their Fig. 10, top left panel), based on *ROSAT* observations of a much smaller source sample (they give 45% and 35% respectively) in spite of the differences in sensitivity and field of view. This means that this age distribution is very robust and gives a good characterization of the X-ray detected young stars as a whole, over a large area.

The spatial distribution of objects was also examined relative to their position with respect to the gas, based on the comparison with the density contours of the CO map shown in Fig. 12. The last two columns of Table 6 give the number of objects seen in front of dense parts of the cloud (“East” side, around Z CMA), or of regions devoid of gas (“West” side, around GU CMA).

This study yields what seem to be paradoxical results. (i) On the one hand, we can clearly see an expected correlation between the ages of stars and their relation with star formation sites: the youngest stars are spatially correlated with dense gaseous regions of the cloud, as it is observed in, e.g., ONC and OMC2/3 regions (Megeath et al. 2012; Gutermuth et al. 2011), while older stars are spread where the gas is absent. (ii) But on the other hand, we also find young stars in the empty regions (30%), and older stars in the dense regions (34%), while intermediate-age stars (19%) are found everywhere. To help understand this paradox, let us now turn to the distribution of stellar masses.

7.2. Spatial distribution vs. stellar masses

As in the previous Section, we separate the sources in three ranges of mass as shown in panels *d*, *e* and *f* of Fig. 12. The number of objects in each range is given in Table 7. When comparing the overall mass distribution of *XMM-Newton* sources with that obtained from *ROSAT* (Paper I), we find comparable fractions of stars in the ranges $1 - 2 M_\odot$ and $> 2 M_\odot$, respectively $\sim 55\%$ and $\sim 30\%$ of the *ROSAT* sources (see Paper I, Fig.10, top right panel). As expected because of their different sensitivities, the main difference is found for low-mass stars (0.5 to $1 M_\odot$), for which the fraction in the *ROSAT* list is three times lower (15%) than in the present work (41%).

The spatial distribution of the stars found on both sides of the cloud (see the last two columns of Table 6) shows a trend (34/53) for the higher stellar masses to be more concentrated in the dense, East side, in the vicinity of Z CMA. More precisely, Fig. 12*d* shows the stellar mass interval $2 - 9 M_\odot$ broken down in three mass ranges ($2 - 3 M_\odot$, $3 - 5 M_\odot$, and $5 - 9 M_\odot$ for *XMM-Newton* sources: for all these ranges, the *XMM-Newton* field E, overlapping Z CMA, is more populated than the other fields. On the other hand, the *ROSAT* data (for which the masses cannot be determined as accurately as from *XMM-Newton* data) show that high-mass stars ($2 - 9 M_\odot$), which normally are closer to dense matter since they are younger, do exist also far from the main cloud. Intermediate-mass stars (Fig. 12*e*: $1 - 2 M_\odot$) are more evenly distributed on both sides of the cloud, and are quite numerous also in the empty regions of *ROSAT* field, far from the cloud. In contrast, Fig. 12*f* shows a decline of low-mass stars towards the empty, West side of the cloud as detected by *XMM-Newton*, and none in the *ROSAT* field further out.

This strong effect cannot be entirely due to the comparatively low sensitivity of the *ROSAT* observations. It is true that, as men-

Table 6. Number of X-ray sources as a function of age and mass ranges and their spatial distribution.

Age	<i>XMM</i> ^a	<i>ROSAT/XMM</i> ^b	<i>ROSAT_add</i> ^c	<i>ROSAT_Total</i> ^d	<i>XMM+ROSAT_add</i> ^e	Side of Cloud	
						East ^f	West ^g
0.3-5 Myr	93 (41%)	20 (53%)	12 (48%)	32 (51%)	105	81 (47%)	24 (30%)
5-10 Myr	42 (19%)	5 (13%)	5 (20%)	10 (16%)	47	32 (19%)	15 (19%)
10-55 Myr	90 (40%)	13 (34%)	8 (32%)	21 (33%)	98	58 (34%)	40 (51%)
Mass							
0.5-1 M_{\odot}	93 (41%)	14 (37%)	1 (4%)	15 (24%)	94	79 (46%)	15 (19%)
1-2 M_{\odot}	89 (40%)	17 (45%)	14 (56%)	31 (49%)	103	58 (34%)	45 (57%)
2-9 M_{\odot}	43 (19%)	7 (18%)	10 (40%)	17 (27%)	53	34 (20%)	19 (24%)

Percents computed as a function of total number of sources: (a) 225 (*XMM-Newton*); (b) 38 *XMM-Newton* best sample detected by *ROSAT*; (c) Additional 25 *ROSAT* sources; (d) 63 (all *ROSAT*); (e) 250 (*XMM+ROSAT*); (f) 171 (on dense regions: $A_V > 2$); and (g) 79 (outside the cloud: $A_V < 2$).

tioned in Table 4, the *ROSAT* observations in this area are 0.3 dex less sensitive than the East field *XMM-Newton* observation (a factor of 2 in luminosity), so that the *ROSAT* census of low-mass stars ($M_{\star} < 1 M_{\odot}$) cannot be complete. Nevertheless, as shown by Table 6, where we have indicated the sources detected both by *ROSAT* and *XMM-Newton*, we see that in total 15 low-mass stars have been successfully detected by *ROSAT*, but 4 only ($\sim 25\%$) have been detected in the area defined by the *XMM-Newton* Field W, and none beyond. Since we see in all the other panels of Fig. 12 that there are many *ROSAT* detections outside of the *XMM-Newton* fields, this effect must be real.

To look in greater detail at this apparently different behaviour in our X-ray detection of low-mass stars compared to higher-mass stars, we have created a set of three figures (Fig. 13a, 13b, and 13c), corresponding to the same late age range as Fig. 12c (10-55 Myr), but broken down in three low-mass ranges (respectively 0.5-1 M_{\odot} , 0.5-0.8 M_{\odot} , and 0.5-0.7 M_{\odot}). We also include, for each panel, the *ROSAT* detections, even if they correspond also to *XMM-Newton* detections. First, we see a very clear trend for the number of sources to diminish towards lower masses: there are only two *XMM-Newton* detections left (and no *ROSAT* below 0.7 M_{\odot} , compared with 39 *XMM-Newton* and 4 *ROSAT* detections below 1 M_{\odot}). Second, even though we know the *ROSAT* sample is incomplete below 1 M_{\odot} , we still have 3 *ROSAT* detections (and 14 *XMM-Newton*) between 0.5 and 0.8 M_{\odot} . However, irrespective of the (low-mass) range, there is no detection in the *ROSAT* field outside of the *XMM-Newton* fields. Third, this effect corresponds to the empty area visible in the mass-age scatter plot for our “best sample” of *XMM-Newton* sources (Fig. 6), for $M_{\star} < 0.7 M_{\odot}$ and age > 10 Myr. Such an effect is not expected in the *ROSAT* data because of its incompleteness in this mass range.

In fact, there is a physical reason for this behaviour of low-mass stars. The study by Preibisch & Feigelson (2005) on the evolution of X-ray emission in young stars spanning the 1 - 10 Myr age range, which covers very young clusters in Orion (COUP: Getman et al. 2005a), NGC2264 and Chamaeleon, supplemented by older, open clusters (Pleiades, Hyades) extending the ages to 650 Myr, has shown two regimes. During the PMS phase (up to ~ 10 Myr), the X-ray luminosity is roughly constant for all masses, which corresponds to the “saturated phase” in which the young stars are fully convective. Then a radiative core develops, and beyond 10 Myr the X-ray luminosity decreases abruptly (see their Fig. 4) in relation with the stellar spin-down (link with the magnetic field generation by the $\alpha\Omega$ dynamo; see also Vidotto et al. 2014). Preibisch & Feigelson (2005) show that, for masses $M_{\star} = 0.5-0.9 M_{\odot}$, the median X-ray luminosity $\langle L_X \rangle$ (in erg s^{-1}) declines from $\langle \log L_X \rangle \sim 30$ between 1

and ~ 10 Myr (ONC, NGC 2264 and Chamaeleon), down to $\langle \log L_X \rangle \sim 29$ at ~ 100 Myr (Pleiades and Hyades). The slope of the decline is steeper for higher masses¹¹. So in our case, given the sensitivity of our X-ray observations ($\log L_X \sim 29.3 - 29.5$ for *XMM*, see Table 4), we interpret the empty area of Fig. 6 as evidence for this decline in magnetic activity at > 10 Myr for $M_{\star} < 0.7 M_{\odot}$.

Consequently, the West side of the cloud very likely contains low-mass stars, but these were formed over 10 Myr ago, in an earlier episode of star formation, and are now too faint to be visible in our observations. In fact, several objects detected by *WISE* appear in this side of the cloud, without IR excess, so may be Class III or field stars.

More precisely, since the *WISE* detections imply the existence of faint, evolved circumstellar disks (debris, and/or planet-forming), the corresponding stars are classified Class II/III, and it is worth considering whether their presence affects their detectability in X-rays (i.e., their magnetic activity), in addition to, or instead of, the change in internal structure at ages ~ 10 Myr. First, with reference to Fig. 13a ($M_{\star} = 0.5-1.0 M_{\odot}$), we find 14 *XMM* sources to the West of the cloud complex ($A_V < 2$): 3 have ages < 10 Myr, and 11 have ages > 10 Myr. However, of these only 5 have a *WISE* classification: below 10 Myr, 2 sources are Class III (no disk), above 10 Myr 1 is Class II/III, and 2 are Class III. Within this small sample, the difference is not significant. To increase the statistics, we can enlarge the sample in mass: for the range $M_{\star} = 0.5-2.0 M_{\odot}$, we find 19 sources having a *WISE* classification, respectively 1 Class II/III vs. 7 Class III for ages < 10 Myr, and 1 Class II/III vs. 10 Class III for ages > 10 Myr, so the difference in diskless stars (7 vs. 10) is again not significant. In other words, the decline in magnetic activity after ~ 10 Myr equally affects the X-ray detectability of low-mass stars, whether or not they are surrounded by (evolved) disks.

8. Conclusions

We focus our main conclusions on two issues: (i) a major observational contribution, which has increased the known census of the stellar population associated with CMa R1 by a factor 15, and (ii) the implication of these results to unveil its complex star formation history. By discussing the interplay between star formation and molecular clouds that probably dictated the scenario of this history, we aim to shed some light on the role of stellar feedback on molecular clouds, an open issue on the general context of star formation in the Galaxy.

¹¹ More recent studies indicate a decline at later ages (> 100 Myr), but they scale L_X with other stellar parameters, e.g., L_X/L_{bol} (Jackson et al. 2012), L_X normalized by stellar surface (Booth et al. 2017).

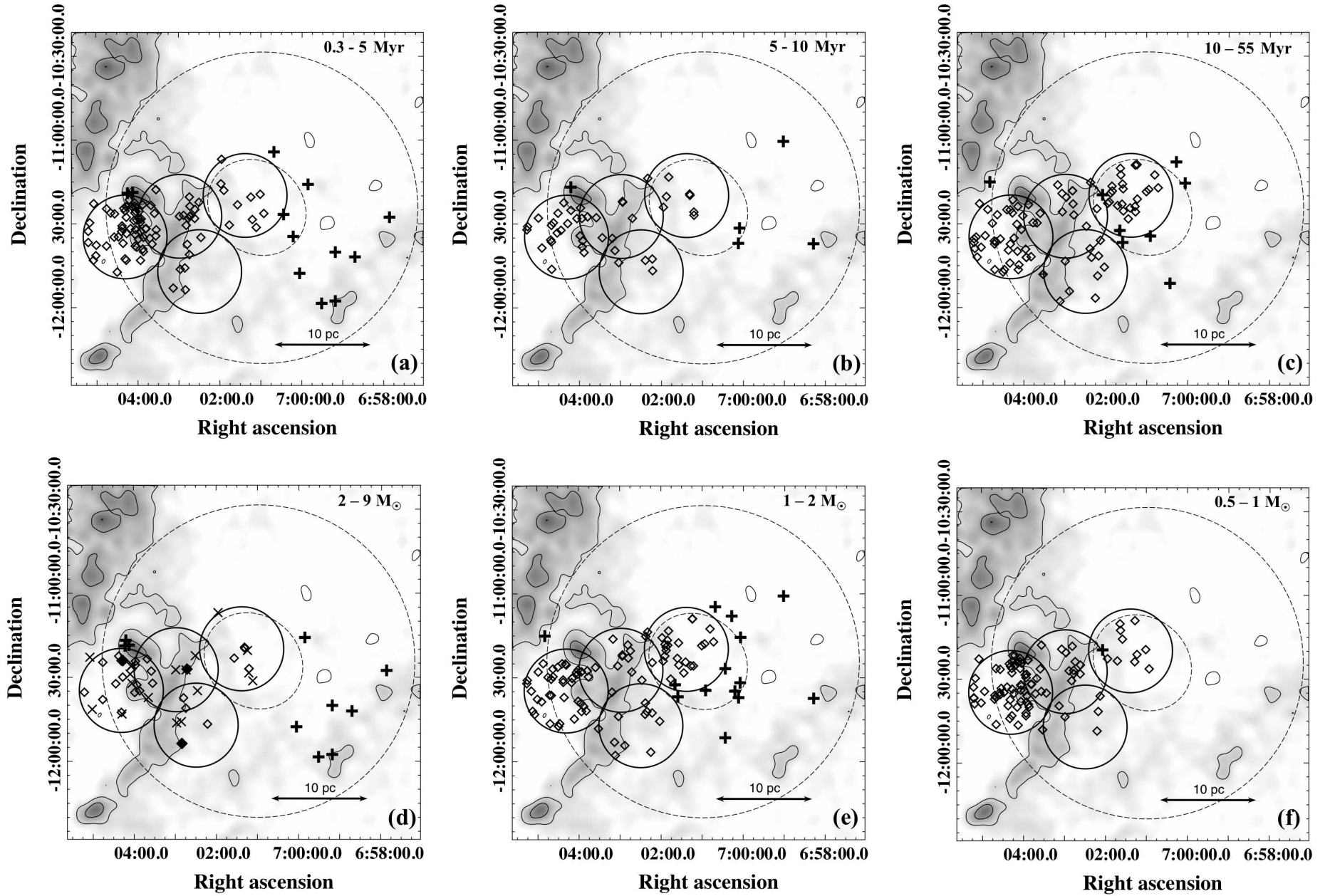


Fig. 12. Spatial distribution of NIR counterparts compared with the visual extinction map⁹. The lowest contours indicate a separation of dense regions ($A_V > 2$). The diamonds and crosses represent *XMM-Newton* and *ROSAT* sources respectively. Top panels a, b and c show objects with less than 5 Myr, 5 to 10 Myr and more than 10 Myr respectively. Bottom panels d, e and f are objects with masses larger than $2 M_\odot$, 1 to $2 M_\odot$ and between 0.5 to $1 M_\odot$, in this panel are highlighted *XMM-Newton* objects with masses between 2 and $3 M_\odot$ (diamonds), 3 and $5 M_\odot$ (X) and more than $5 M_\odot$ (full diamonds). Black full lines delimit the fields E, C, S and W and *ROSAT* field are by dashed line.

In a study on the reliability of age measurements for YSOs, Preibisch (2012) points out the debate in the literature concerning the time scale of star formation. Some authors argue that star formation should be a “fast”, dynamic process (e.g., Hartmann et al. 2001; Elmegreen 2007; Dib et al. 2010), while an opposite view of a “slow” quasi-static equilibrium process has also been discussed (e.g., Palla & Stahler 2000; Tan et al. 2006; Huff & Stahler 2007; Palla 2011). Testing these theories depends on the estimate of star-forming duration and a good determination of the age spread of the YSO population.

The presence of a relatively old population in the whole area (i.e., both the dense gaseous and empty sides of the cloud) suggests that stars were slowly formed in a first episode throughout the region, > 10 Myr ago. As argued above, the older low-mass stars are not seen in the West side because their X-ray emission has fallen below our detection limit. Massive stars ($M_{\star} < 9 M_{\odot}$) are however present in this area, but are younger than 10 Myr and are absent at older ages. Since these stars have a lifetime ~ 40 Myr, more massive ones having a lifetime $< 40 - 10 = 30$ Myr, i.e., $M_{\star} > 10 M_{\odot}$, consistent with the current IMF (Fig. 7), may have existed then exploded, dispersing the molecular clouds and possibly preventing the formation of new stars. Of course, after such a long time (30 Myr ago), one can hardly expect to see any trace of the explosion(s), precisely because the masses and spatial distribution of the molecular clouds must have been very different from what they are now.

We avoid being affected by these difficulties in the age determinations by being able to break down the ages into less precise, but broader ranges. Indeed, we have found a true bimodal distribution of ages, with two clearly distinct groups: one is younger (< 5 Myr) and the other is older (> 10 Myr), with less of 20% of the objects in the intermediate age range (5 - 10 Myr). Therefore, our results show that at least two star formation episodes took place in the same region, separated by at least ~ 5 Myr.

The older low-mass stars, as well as their putative associated high-mass O stars, are however not seen in the West side: the former because their X-ray emission has fallen below our detection limit, and the latter because they have exploded after having undergone an intense mass loss (Wolf-Rayet) phase, dispersing almost all the CO-emitting material in this area, thus preventing the birth of new stars.

On the other hand, the presence of a large number of objects < 5 Myr old and some disk-bearing T Tauri stars, as well as Herbig stars, located in the dense part (East side) of the cloud suggests a later episode of concentrated star formation that may have been caused by compression of the gas, perhaps triggered from the West side by the now defunct massive stars of the previous generation.

We can compare this scenario with the conclusions of Palla & Stahler (2002), who developed a picture of star formation history in the Taurus-Auriga cloud complex, based on a comparison between stellar ages and the spatial distribution of the gas. At least 10 Myr ago, a low level of dispersed star-formation occurred over a broad and diffuse gaseous area; due to the quasi-static contraction of the clouds, the material was concentrated in filaments under the gravity action combined with shock dissipation. Recent results based on millimetric observations from *Herschel*, for instance, have confirmed the important role of the interstellar filamentary structure on the formation process of low-mass prestellar cores (e.g., André et al. 2010, 2014). These filaments have presumably acquired the minimum density required to accelerate the star-formation rate, and a new group of stars was generated in the last few Myr. In our case, however, we attribute the dissipation of gas to the action of massive stars

that have now disappeared - such massive stars are not invoked in the Taurus-Auriga picture. Palla & Stahler (2002) suggest in this case that dissipation occurs through the action of low-mass stellar outflows.

Considering the ages of the CMa R1 members, their spatial distribution, and the masses of the molecular cloud complex, we find indications that this association is going through the final stages of the star formation process. On a large scale, the cloud material appears dispersed, probably due the evaporation caused by a previous generation of massive stars as argued above. The list of ^{13}CO clouds surveyed by Kim et al. (2004) contains only three small clouds ($< 10^3 M_{\odot}$) near the region covered by our *XMM-Newton* and *ROSAT* observations. Projected against our *XMM-Newton* fields, the only available matter is provided by the cloud 224.7-02.5 ($890 M_{\odot}$, $21 M_{\odot}/\text{pc}^2$), which coincides with the area around Z CMa (East side) where the stars are still being formed. Considering the presence of a few stars with $M_{\star} > 8 M_{\odot}$, within less than ~ 10 Myr from now new supernova explosions will disperse the remaining material, which shall mark the very end of the CMa R1 molecular complex as a star-forming region.

Acknowledgements. Part of this work was supported by CAPES/Cofecub Project 712/2011. TSS acknowledges financial support from CNPq (Proc. No. 142851/2010-8 and 207433/2014-3) and CAPES (Proj: PNP20132533). JGH thanks FAPESP (Proc. No. 2010/50930-6 and 2014/18100-4). BF thanks CNPq project 150281/2017-0. We thank T. Onishi (Osaka University) for having provided us with his ^{13}CO data in advance of publication. This work has made use of the VizieR, and Aladin databases operated at CDS, Strasbourg, France. This publication makes use of data products from the Two Micron All Sky Survey, which is a joint project of the University of Massachusetts and the Infrared Processing and Analysis Center/California Institute of Technology, funded by the National Aeronautics and Space Administration and the National Science Foundation.

References

- Amôres, E. B. & Lépine, J. R. D. 2005, *AJ*, 130, 659
 André, P., Di Francesco, J., Ward-Thompson, D., et al. 2014, *Protostars and Planets VI*, 27
 André, P., Men'shchikov, A., Bontemps, S., et al. 2010, *A&A*, 518, L102
 Bally, J. 2008, *Overview of the Orion Complex*, ed. B. Reipurth, 459
 Barrado, D., Stelzer, B., Morales-Calderón, M., et al. 2011, *A&A*, 526, A21
 Bastian, N., Covey, K. R., & Meyer, M. R. 2010, *ARA&A*, 48, 339
 Bessell, M. S. & Brett, J. M. 1988, *PASP*, 100, 1134
 Booth, R. S., Poppenhaeger, K., Watson, C. A., Silva Aguirre, V., & Wolk, S. J. 2017, *MNRAS*, 471, 1012
 Cambrésy, L., Beichman, C. A., Jarrett, T. H., & Cutri, R. M. 2002, *AJ*, 123, 2559
 Cardelli, J. A., Clayton, G. C., & Mathis, J. S. 1989, *ApJ*, 345, 245
 Casanova, S., Montmerle, T., Feigelson, E. D., & Andre, P. 1995, *ApJ*, 439, 752
 Chabrier, G. 2005, in *Astrophysics and Space Science Library*, Vol. 327, *The Initial Mass Function 50 Years Later*, ed. E. Corbelli, F. Palla, & H. Zinnecker, 41
 Cusano, F., Ripepi, V., Alcalá, J. M., et al. 2011, *MNRAS*, 410, 227
 Cutri, R. M. & et al. 2013, *VizieR Online Data Catalog*, 2328
 Cutri, R. M., Skrutskie, M. F., van Dyk, S., et al. 2003, *VizieR Online Data Catalog*, 2246, 0
 Dib, S., Hennebelle, P., Pineda, J. E., et al. 2010, *ApJ*, 723, 425
 Dickey, J. M. & Lockman, F. J. 1990, *ARA&A*, 28, 215
 Elmegreen, B. G. 2007, *ApJ*, 668, 1064
 Favata, F., Flaccomio, E., Reale, F., et al. 2005, *ApJS*, 160, 469
 Favata, F. & Micela, G. 2003, *Space Sci. Rev.*, 108, 577
 Fedele, D., van den Ancker, M. E., Henning, T., Jayawardhana, R., & Oliveira, J. M. 2010, *A&A*, 510, A72
 Feigelson, E. D., Casanova, S., Montmerle, T., & Guibert, J. 1993, *ApJ*, 416, 623
 Feigelson, E. D., Getman, K., Townsley, L., et al. 2005, *ApJS*, 160, 379
 Feigelson, E. D., Getman, K. V., Townsley, L. K., et al. 2011, *ApJS*, 194, 9
 Feigelson, E. D. & Montmerle, T. 1999, *ARA&A*, 37, 363
 Fernandes, B., Gregorio-Hetem, J., Montmerle, T., & Rojas, G. 2015, *MNRAS*, 448, 119
 Fischer, W. J., Padgett, D. L., Stapelfeldt, K. L., & Sewilo, M. 2016, *ApJ*, 827, 96
 Flagey, N., Boulanger, F., Noriega-Crespo, A., et al. 2011, *A&A*, 531, A51

Forbrich, J., Posselt, B., Covey, K. R., & Lada, C. J. 2010, *ApJ*, 719, 691
Franciosini, E., Pillitteri, I., Stelzer, B., et al. 2007, *A&A*, 468, 485
Getman, K. V., Feigelson, E. D., Grosso, N., et al. 2005a, *ApJS*, 160, 353
Getman, K. V., Flaccomio, E., Broos, P. S., et al. 2005b, *ApJS*, 160, 319
Gregorio-Hetem, J. 2008, *The Canis Major Star Forming Region*, ed. B. Reipurth, 1
Gregorio-Hetem, J., Montmerle, T., Rodrigues, C. V., et al. 2009, *A&A*, 506, 711
Guarcello, M. G., Micela, G., Peres, G., Prisinzano, L., & Sciortino, S. 2010, *A&A*, 521, A61
Güdel, M. 2004, *A&A Rev.*, 12, 71
Güdel, M., Briggs, K. R., Arzner, K., et al. 2007, *A&A*, 468, 353
Günther, H. M., Wolk, S. J., Spitzbart, B., et al. 2012, *AJ*, 144, 101
Gutermuth, R. A., Pipher, J. L., Megeath, S. T., et al. 2011, *ApJ*, 739, 84
Haisch, Jr., K. E., Lada, E. A., & Lada, C. J. 2001, *ApJ*, 553, L153
Hartmann, L., Ballesteros-Paredes, J., & Bergin, E. A. 2001, *ApJ*, 562, 852
Hasinger, G., Altieri, B., Arnaud, M., et al. 2001, *A&A*, 365, L45
Hernández, J., Hartmann, L., Calvet, N., et al. 2008, *ApJ*, 686, 1195
Huff, E. M. & Stahler, S. W. 2007, *ApJ*, 666, 281
Jackson, A. P., Davis, T. A., & Wheatley, P. J. 2012, *MNRAS*, 422, 2024
Jose, J., Pandey, A. K., Ogura, K., et al. 2011, *MNRAS*, 411, 2530
Kalberla, P. M. W., Burton, W. B., Hartmann, D., et al. 2005, *VizieR Online Data Catalog*, 8076, 0
Kaltcheva, N. T. & Hilditch, R. W. 2000, *MNRAS*, 312, 753
Kim, B. G., Kawamura, A., Yonekura, Y., & Fukui, Y. 2004, *PASJ*, 56, 313
Koenig, X. P. & Leisawitz, D. T. 2014, *ApJ*, 791, 131
Kroupa, P. 2001, *MNRAS*, 322, 231
Krumholz, M. R. 2014, *Phys. Rep.*, 539, 49
Lee, H.-T., Chen, W. P., Zhang, Z.-W., & Hu, J.-Y. 2005, *ApJ*, 624, 808
López-Santiago, J., Albacete Colombo, J. F., & López-García, M. A. 2010, *A&A*, 524, A97
López-Santiago, J. & Caballero, J. A. 2008, *A&A*, 491, 961
Megeath, S. T., Gutermuth, R., Muzerolle, J., et al. 2012, *AJ*, 144, 192
Meyer, M. R., Calvet, N., & Hillenbrand, L. A. 1997, *AJ*, 114, 288
Nebot Gómez-Morán, A., Motch, C., Barcons, X., et al. 2013, *A&A*, 553, A12
Onishi, T., Nishimura, A., Ota, Y., et al. 2013, *PASJ*, 65, 78
Palla, F. 2011, in *EAS Publications Series*, Vol. 51, *EAS Publications Series*, ed. C. Charbonnel & T. Montmerle, 245–287
Palla, F. & Stahler, S. W. 2000, *ApJ*, 540, 255
Palla, F. & Stahler, S. W. 2002, *ApJ*, 581, 1194
Preibisch, T. 2012, *Research in Astronomy and Astrophysics*, 12, 1
Preibisch, T. & Feigelson, E. D. 2005, *ApJS*, 160, 390
Preibisch, T., Kim, Y.-C., Favata, F., et al. 2005, *ApJS*, 160, 401
Preibisch, T. & Mamajek, E. 2008, *The Nearest OB Association: Scorpius-Centaurus (Sco OB2)*, ed. B. Reipurth, 235
Rebull, L. M., Padgett, D. L., McCabe, C.-E., et al. 2010, *ApJS*, 186, 259
Rieke, G. H. & Lebofsky, M. J. 1985, *ApJ*, 288, 618
Ryter, C. E. 1996, *Ap&SS*, 236, 285
Salpeter, E. E. 1955, *ApJ*, 121, 161
Santos-Silva, T. & Gregorio-Hetem, J. 2012, *A&A*, 547, A107
Shevchenko, V. S., Ezhkova, O. V., Ibrahimov, M. A., van den Ancker, M. E., & Tjin A Djie, H. R. E. 1999, *MNRAS*, 310, 210
Siess, L., Dufour, E., & Forestini, M. 2000, *A&A*, 358, 593
Smith, R. K., Brickhouse, N. S., Liedahl, D. A., & Raymond, J. C. 2001, *ApJ*, 556, L91
Soares, J. B. & Bica, E. 2002, *A&A*, 388, 172
Soares, J. B. & Bica, E. 2003, *A&A*, 404, 217
Stelzer, B., Flaccomio, E., Briggs, K., et al. 2007, *A&A*, 468, 463
Tan, J. C., Krumholz, M. R., & McKee, C. F. 2006, *ApJ*, 641, L121
Townsend, L. K., Broos, P. S., Corcoran, M. F., et al. 2011, *ApJS*, 194, 1
Vidotto, A. A., Gregory, S. G., Jardine, M., et al. 2014, *MNRAS*, 441, 2361
Vuong, M. H., Montmerle, T., Grosso, N., et al. 2003, *A&A*, 408, 581
Watson, M. G., Pye, J. P., Denby, M., et al. 2003, *Astronomische Nachrichten*, 324, 89
Wolk, S. J., Harnden, Jr., F. R., Flaccomio, E., et al. 2005, *ApJS*, 160, 423
Wright, E. L., Eisenhardt, P. R. M., Mainzer, A. K., et al. 2010, *AJ*, 140, 1868

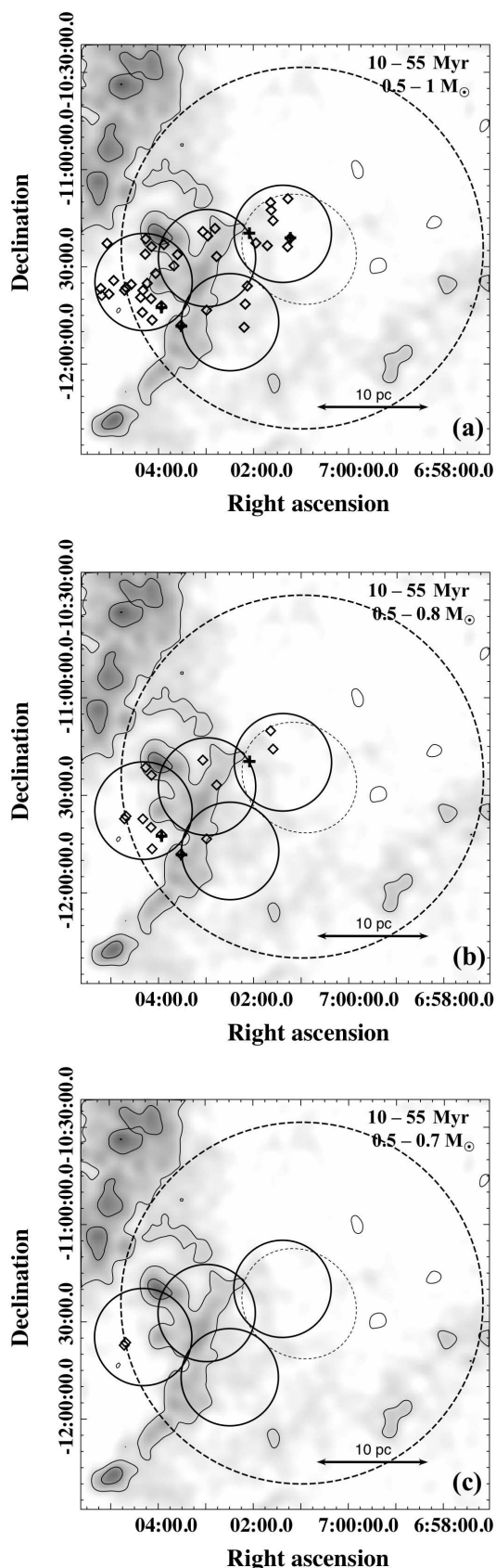


Fig. 13. Same as Fig. 12c (spatial distribution in the age range 10–55 Myr), but for low-mass stars only. In the three panels (a, b, c), the stellar masses are broken down in three mass ranges ($0.5\text{--}1 M_{\odot}$, $0.5\text{--}0.8 M_{\odot}$, $0.5\text{--}0.7 M_{\odot}$, respectively), diamonds represents *XMM-Newton* sources and crosses are *ROSAT* sources. As discussed in the text (Sect. 7.2) and as is visible in Fig. 6, the nearly complete absence of stars with $M < 0.7 M_{\odot}$ is due to the decline of their magnetic activity after ~ 10 Myr.

Appendix A: X-ray properties

This appendix describes in detail how the X-ray properties, such as hardness ratios (HRs), variability, spectra and light curves, were obtained from the *XMM-Newton* PN data (See Sect.2).

Appendix A.1: Hardness ratios diagrams

We have adopted the energy bands defined by Barrado et al. (2011) from 0.5 to 7.3 keV and Hasinger et al. (2001) from 0.2 to 4.5 keV (see Sect. 2) aiming to distinguish sources with predominant soft, thermal emission (up to 2 keV), expected in young stars (Feigelson & Montmerle 1999), from sources with hard, non-thermal emission produced by AGNs¹².

In order to compare the observed HRs with the expected values from a stellar (thermal coronal) emission or extragalactic emission, two models were simulated for the respective energy bands using XSPEC version 12.7.1: a thermal (APEC) and a power-law (PWL) distribution. A multiplicative absorption photoelectric model (PHABS) with $\log N_H$ between 20 and 23, in steps of 0.5, was applied to both models. The APEC model was used to simulate the thermal emission for $\log(T)$ varying from 6.0 to 8.5 in steps of 0.5 and metallicity Z relative to the Sun of $Z = 0.2 Z_\odot$. The choice of this metallicity is based on tests that we performed, which provided good fittings with Z varying from 0.04 to 0.34 Z_\odot . The assumed intermediate value $Z = 0.2 Z_\odot$ resulted in differences of less than 10% on estimates of T and N_H . In the power-law simulations we use the index $\gamma = 0, 1, 2$ and 3, for $F_X(E) \propto E^{-\gamma}$. Fig. A.1 and A.2 show diagrams for Hardness Ratios (HRs) obtained respectively in the bands defined by Barrado et al. (2011, B2011) and by Hasinger et al. (2001, 2011), described in Sect. 3. The thermal grid is presented by red lines and the power-law grid by black lines. Different colours are used in Fig. A.1 and A.2 to indicate how the sources were classified as compatible with each grid model.

Our analysis was restricted to the sources with estimates in the range $-1 < HR < 1$. These limits avoid sources having soft emission at the same level found in the background ($HR > 1$), and sources lacking of emission in the hard bands ($HR < -1$). Following Nebot Gómez-Morán et al. (2013), our sub-sample was also constrained to the sources having HR error-bars smaller than 0.3. Among 340 sources with PN data, only 196 sources with HRs in the B2011 bands (Fig. A.1) fulfil these restriction criteria and could be compared with the grids. Among them, 133 are only compatible with the APEC grid while 9 with the PWL grid only. The other 54 coincide with both models. For H2001 HRs diagrams (Fig. A.2) the number of analysed sources is little lower than the subsample studied in the B2011 energy ranges, probably due to intrinsically low emission of stars in the soft band or high absorption of our observations in the soft band (0.2 to 0.4keV), which gives $HR_{H2001} = -1$ for several of the sources. In total, Fig. A.2 contains 178 sources, 137 of them are compatible with the APEC grids, 8 for PWL and 33 for both.

Aiming to enlarge the number of classified sources, and to solve inconclusive characterization of sources that coincide with the two model grids, we combined the results from both definitions for energy bands. For each source we adopted the more reliable classification that could be found by comparing its position in both Figs. A.1 and A.2. If a given source falls in the models overlapping region of the B2011 HR diagram, for in-

stance, and coincides with the H2001 APEC grid, it is classified as compatible with the APEC model.

We could not discuss the origin of 193 sources because 149 of them have no data available in any HRs diagram and 44 sources remained consistent with both models (APEC and PWL). In total, 194 sources were classified according to their X-ray emission: about 6% (11/194) of them are compatible only with the PWL model, so they probably are extragalactic or evolved objects, while 94% (183/194) may have stellar origin.

The HRs of ~60% of the sources are compatible with the APEC model grid. The majority of them are found in the ranges $21 < \log N_H < 22$ and $6.5 < \log T(K) < 7.5$, which corresponds to the plasma temperature expected for low-mass young stars (Feigelson & Montmerle 1999). In spite of their larger scattering, in Fig. A.1 these objects have HRs comparable with the young stars associated with the low extinction stellar cluster Collinder 69, studied by Barrado et al. (2011), which are more concentrated in between $\log N_H = 20 - 21.5$. The results are discussed in Sect. 3.

Appendix A.1.1: Ages and X-ray emission

Aiming to discuss the efficiency of adopting the HRs diagrams to select young star candidates, we compare here the results from Sect. 3.1 with the ages that were determined in Sect. 4.1 and analyzed in Sect. 4.3. In this comparison, we consider only X-ray sources with HRs that are inside the diagrams edges and have NIR counterparts with ages well determined (our “best sample”). So that 130 and 134 objects were taken into account in B2011 and H2001 diagrams, respectively.

The histograms in Fig. A.3 show the distribution of number of sources as a function of age, compared with their position in the HRs diagrams. As expected, most of the objects, in all the PMS ranges of age, correspond to the APEC (stellar emission) model for both HRs diagrams. Only a few sources (~10%), mainly for B2011 and those with >5 Myr, coincide with PWL model or appear out of both grids. Finally, Fig. A.3 also shows 10% to 20% of objects with < 10 Myr coinciding with both models (APEC and PWL), which is confirmed by both HRs diagrams (B2011 and H2001). This is an indication that these sources must be kept as possible young stars.

If we consider the sources having infrared excess not included in the “best sample”, more than 75% of these objects are compatible with APEC model in both HRs diagrams, i. e. they may be young stars that are still embedded or have circumstellar disk. Only a few (4%) coincide with PWL model and the remaining ones (20%) are compatible with both grids.

These results show that our method, based only on X-ray emission, is efficient in identifying young star candidates. In fact, the main difficulty of this method is to obtain the HRs in all soft bands.

Appendix A.2: Flares

The extraction of light curves was made for 340 sources detected with the EPIC-PN camera (typical exposures ~ 30 ks) in the 0.5 - 7.3 keV energy band by estimating the count rate in time bins of 1000s. For each source, the count rate was calculated over an area of the image, the size of which is proportional to the intensity of the X-ray emission. The radius of the extraction region varies from $r = 10''$, for faint sources ($L_X \sim 3 \times 10^{29}$ erg/s) to $r = 40''$ for the brightest source showing flare ($L_X \sim 4 \times 10^{31}$ erg/s), but typical values were about $15''$. Following standard routines

¹² Typical pulsars, for instance, are very luminous in X-rays, so at the detection level we have here they would have to be very distant, so very improbable.

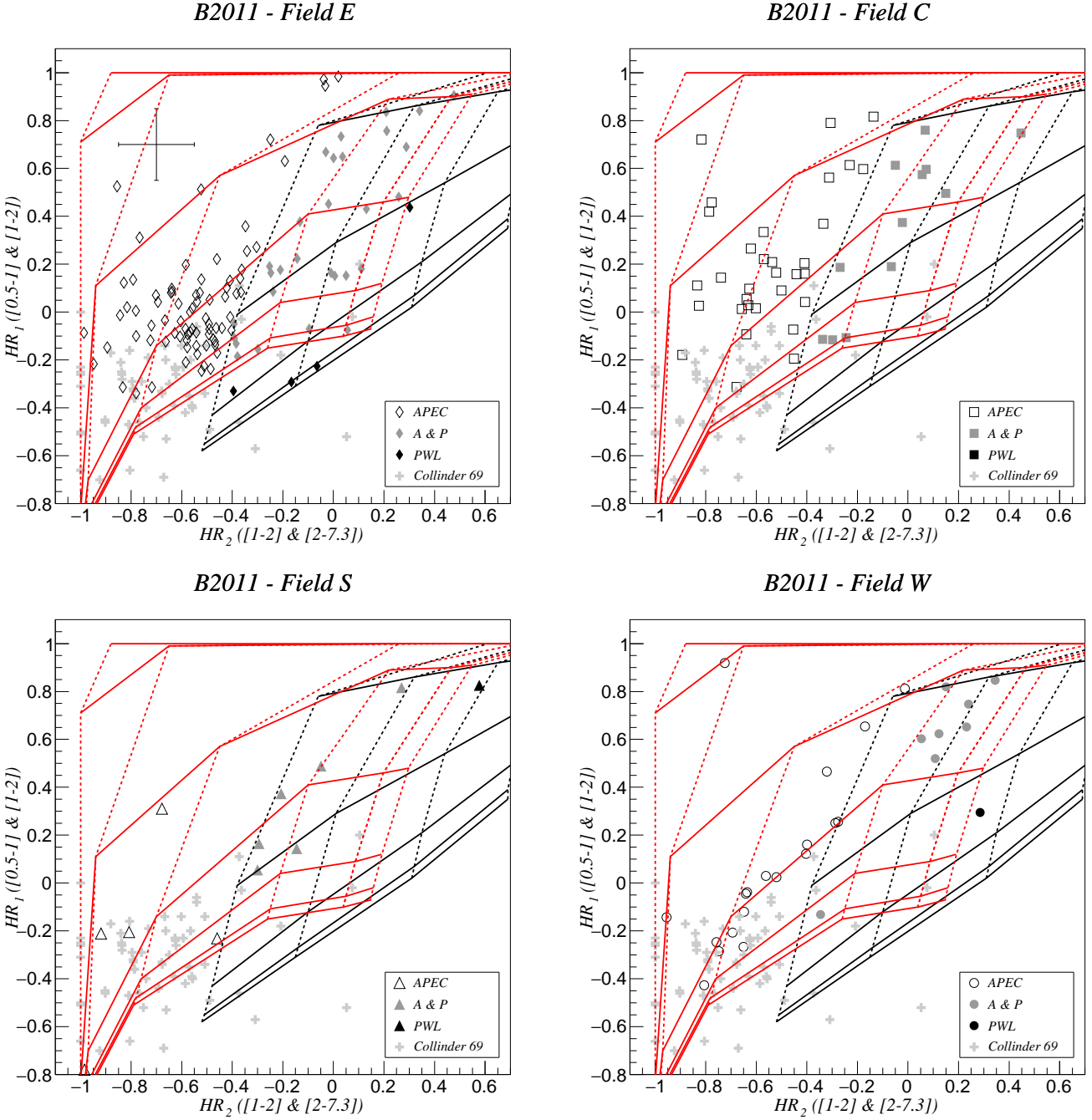


Fig. A.1. Hardness ratio diagrams in 0.5 - 7.3 keV energy band, defined by Barrado et al. (2011), comparing our sample with the stars of the young Collinder 69 cluster (grey crosses). For illustration, error-bars corresponding to 0.15, which is the mean error found in the HR estimates of our sample, are plotted in the first panel. Top panels present the sources from fields E (diamonds) and C (squares), while S (triangles) and W (circles) are shown in the bottom. Grids from the APEC model are displayed in red, by using dotted lines for $6.0 < \log T < 8.5$ (increasing from left to right, in steps of 0.5). Power-law grid with $\gamma = 0, 1, 2$ is shown by black dotted lines (increasing from left to right). Both grids use full lines to represent $20 < \log N_H < 23$, increasing in steps of 0.5, from bottom to top.

from SAS¹³, the background light curve, corresponding to an area of the same size near the source (on the same detector), but free of other sources contamination, was subtracted from the light curve measured at the source position. We searched for sources showing signs of variability by adopting the elevated levels $1.2 \times C_{ch} + 1.5\sigma_{ch} < C_i < 2.5 \times C_{ch} + 1.5\sigma_{ch}$ pro-

posed by Wolk et al. (2005) to indicate peaks of X-ray emission (C_i , in a time bin (i)) detected above the characteristic count-rate ($C_{ch} \pm \sigma_{ch}$). 32 objects were found showing two or more peaks of intensity. In order to identify variations caused by flares, in a first step we estimated C_{ch} by the linear fit of count-rates in the bins (1000s each) with lowest count-rates in a time interval.

We consider a *flare-like* candidate the event with an increase by factor $res = \frac{C_i - C_{ch}}{\sigma_i}$ higher than 3, where C_i and σ_i are the

¹³ <http://xmm.esac.esa.int/sas/current/documentation/threads/timing.-shtml>

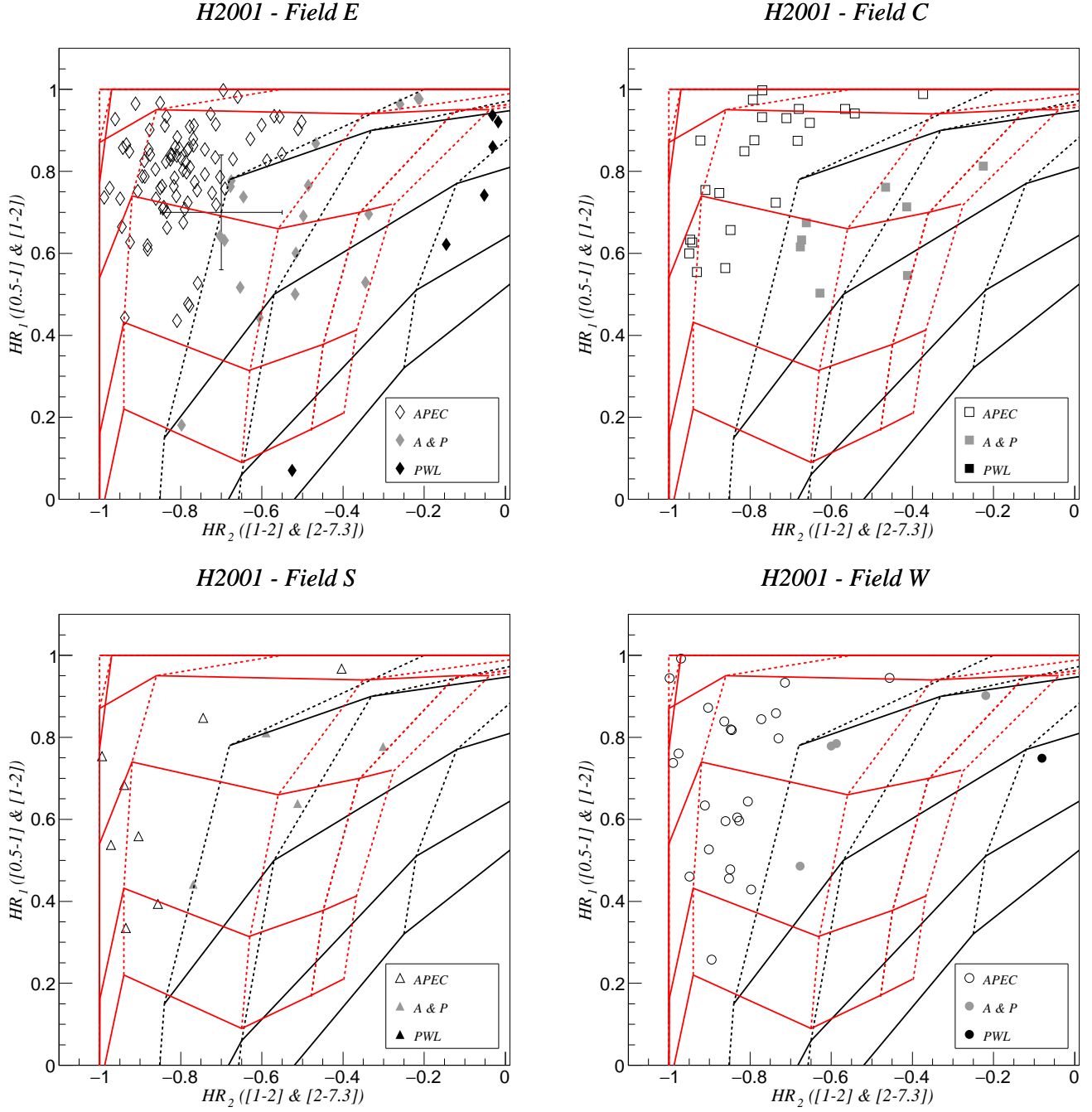


Fig. A.2. The same as Fig. A.1 for hardness ratio diagrams based on 0.2 - 4.5 keV energy band suggested by Hasinger et al. (2001).

count-rate and its error in a time interval i , respectively. The *flare-like* events were confirmed using the definition of flare proposed by Wolk et al. (2005) and Stelzer et al. (2007) that makes use of amplitude (A_i) and the derivative (Δ_i) of a count-rate in a time interval, both defined as:

$$A_i = \frac{C_i - 2\sigma_i}{C_{ch} + 2\sigma_{ch}} \quad (\text{A.1})$$

$$\Delta_{i+1} = \frac{(C_{i+1} - C_i)/C_i}{\text{MIN}[t_{i+1}, t_i]} [s^{-1}] \quad (\text{A.2})$$

The confirmed flares have amplitude $A_i > 1.5$ in one or more consecutive bins and the maximum derivative in these intervals above the threshold is $\Delta_i > 5 \times 10^{-5}$. We also derived the flare luminosity L_f subtracting the characteristic luminosity L_{ch} from the average value of source luminosity during the flare. The flare energies (E_f) were calculated by multiplying this L_f by the time interval during which the X-ray emission is larger than C_{ch} .

The light curves of the 13 sources with *flare-like* events are presented in Figs A.4 and A.5. The increasing factor is shown in the bottom panel of these figures. All parameters derived for these events are listed in Table A.1. Sources E001, E003 and C007 have shown a strong flare. Sources C006 and E041 shown

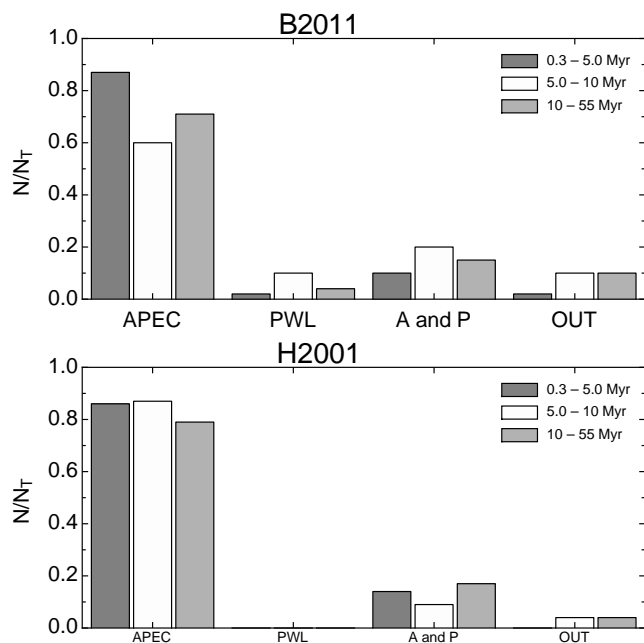


Fig. A.3. Distribution of sources coinciding with thermal plasma (APEC) or power law (PWL) models, and those appearing in the intersection of both grids (A and P) or outside both grids (OUT).

a decay phase that we called ‘partial’ flare, while only the source E007 was not confirmed by Stelzer et al. (2007) criteria.

Appendix A.3: Spectra

In order to investigate the X-ray emitting plasma we analysed the low-resolution EPIC spectra integrated over the whole exposure. They were grouped according to the number of counts, adopting a threshold of 10 counts per bin, after background subtraction. We tested fits for 1T and 2T temperature APEC models. However, due to intrinsically low luminosity, bad statistics or quality of spectra, only 1T model produced good fits with $Z = 0.2 Z_{\odot}$ (see Appendix A.1), and photoelectric absorption model (PHABS) in the XSPEC environment. The fits and the residual $[\sigma(\text{data} - \text{model}) \times \Delta(\chi^2)]$ of observed spectra are shown in Figs. A.7, A.8 and A.9. Best-fits parameters were found by χ^2 minimization. Only for 21 sources a good fit with $0.75 < \chi^2 < 1.3$ was achieved. The fit parameters (N_H and $kT1$), reduced χ^2 and degrees of freedom (d.o.f) are presented in Table A.2, along with the derived fluxes (and luminosities) in the 0.5 - 7.3 keV band.

The hydrogen column density obtained from the spectral fits varies from $0.4 \times 10^{21} \text{cm}^{-2}$ to $5.4 \times 10^{21} \text{cm}^{-2}$, with mean value $N_H = 1.8 \pm 1.5 \times 10^{21} \text{cm}^{-2}$ that corresponds to an extinction $A_V = 0.9 \pm 0.7 \text{ mag}$, adopting $N_H = 2.1 \times 10^{21} A_V \text{cm}^{-2}$ (e.g., Vuong et al. 2003). The coronal temperatures in Table A.2 vary from 0.7 to 2.1 keV, with average value of $1.4 \pm 0.4 \text{ keV}$.

Table A.1. Parameters of X-ray flares detected on CMa R1 sources

Source	T ^a (ks)	log L _{ch} ^b [erg/s]	res ^c	log L _f ^d [erg/s]	log E _f ^e [erg]	A _f ^f	Δ _f ^g [10 ⁻⁵ cts/s ²]	Flare
C003	5	30.1	3.4	30.0	33.7	1.7	2262.4	Confirmed
C006	>7	29.8	3.4	>29.9	>33.7	-	-	Partial
C007	7	29.6	4.6	30.2	34.1	7.1	5147.1	Confirmed
C019	2	29.7	3.5	29.7	33.0	2.6	45833.3	Confirmed
E001	26	30.7	11.5	31.1	35.5	5.2	4340.3	Confirmed
E003	19	30.2	11.2	30.9	35.2	12.2	20122	Confirmed
E007	3	30.2	3.1	29.5	33.0	-	-	Candidate
E016	2	30.1	3.9	29.3	32.6	2.2	3492.1	Confirmed
E017	4	30.0	3.6	30.3	33.9	2.2	15555.6	Confirmed
E041	>15	29.7	3.7	>30.0	>34.2	2.9	-	Partial
E043**	5	29.9	3.0	29.3	33.0	1.6	77777.8	Confirmed
E060	7	29.8	3.3	29.7	33.5	2.1	3896.1	Confirmed
S003**	4	29.7	3.6	29.2	32.8	2.7	34782.6	Confirmed

(a) Duration of flares (T); (b) Characteristic luminosity (L_{ch}); (c) Maximum factor of light curves; (d) Flare luminosity (L_f); (e) Flare Energy (E_f); (f) Amplitude (A_f); (g) Derivative Δ_f;
 ** Sources with two NIR counterparts.

Table A.2. Spectral parameters of CMa R1 bright sources.

ID	N _H (10 ²² cm ⁻²)	kT1 (keV)	χ ² (d.o.f)	F _X (10 ⁻¹⁴) (erg/cm ² /s)	log (L _X)
C001	0.36 ^{+0.14} _{-0.08}	1.25 ^{+0.12} _{-0.26}	1.20 (39)	4.7 ^{+1.03} _{-0.78}	30.8
C005	0.13 ^{+0.08} _{-0.05}	1.49 ^{+0.36} _{-0.28}	0.84 (16)	2.6 ^{+0.56} _{-0.50}	30.5
E002	0.14 ^{+0.03} _{-0.03}	2.04 ^{+0.61} _{-0.27}	0.97 (63)	11.9 ^{+1.28} _{-1.21}	31.2
E004	0.16 ^{+0.05} _{-0.04}	1.79 ^{+0.33} _{-0.25}	0.89 (47)	9.2 ^{+1.35} _{-1.22}	31.0
E005	0.07 ^{+0.03} _{-0.03}	1.55 ^{+0.19} _{-0.28}	1.25 (47)	5.8 ^{+0.76} _{-0.76}	30.8
E015	0.12 ^{+0.07} _{-0.05}	1.58 ^{+0.49} _{-0.27}	0.83 (32)	4.6 ^{+0.83} _{-0.86}	30.7
E019	0.34 ^{+0.13} _{-0.10}	2.10 ^{+1.10} _{-0.49}	1.09 (25)	3.7 ^{+0.92} _{-0.86}	30.7
E020	0.07 ^{+0.05} _{-0.04}	1.25 ^{+0.29} _{-0.25}	1.01 (28)	2.7 ^{+0.62} _{-0.55}	30.5
E021	0.30 ^{+0.13} _{-0.15}	0.70 ^{+0.14} _{-0.10}	0.91 (15)	2.7 ^{+1.39} _{-1.16}	30.5
E022	0.08 ^{+0.06} _{-0.05}	1.64 ^{+1.86} _{-0.38}	1.01 (20)	2.4 ^{+0.56} _{-0.49}	30.5
E023	0.08 ^{+0.08} _{-0.05}	1.01 ^{+0.12} _{-0.09}	1.02 (24)	2.7 ^{+0.80} _{-0.60}	30.5
E026	0.61 ^{+0.17} _{-0.17}	0.95 ^{+0.22} _{-0.14}	0.94 (31)	3.1 ^{+1.37} _{-1.03}	30.6
E034	0.08 ^{+0.07} _{-0.05}	1.91 ^{+1.66} _{-0.72}	1.31 (15)	2.0 ^{+0.45} _{-0.45}	30.4
E036	0.12 ^{+0.20} _{-0.10}	1.23 ^{+0.28} _{-0.18}	0.84 (20)	2.4 ^{+1.21} _{-0.73}	30.5
E038	0.13 ^{+0.11} _{-0.09}	1.59 ^{+1.25} _{-0.33}	1.10 (14)	4.5 ^{+1.28} _{-1.09}	30.7
E044	0.54 ^{+0.24} _{-0.13}	0.54 ^{+0.09} _{-0.20}	1.21 (11)	1.2 ^{+3.10} _{-0.47}	30.2
E055	0.11 ^{+0.08} _{-0.06}	1.25 ^{+0.44} _{-0.51}	1.08 (18)	1.9 ^{+0.56} _{-0.49}	30.4
W001	0.04 ^{+0.01} _{-0.01}	0.99 ^{+0.02} _{-0.02}	0.99 (237)	54.5 ^{+2.36} _{-2.28}	31.8
W002	0.04 ^{+0.05} _{-0.04}	1.18 ^{+0.16} _{-0.17}	1.14 (17)	2.4 ^{+0.59} _{-0.51}	30.4
W003	0.12 ^{+0.06} _{-0.06}	2.09 ^{+6.09} _{-0.59}	0.79 (18)	3.8 ^{+0.75} _{-0.68}	30.7
W006	0.12 ^{+0.10} _{-0.07}	1.27 ^{+0.41} _{-0.23}	1.12 (13)	1.5 ^{+0.43} _{-0.37}	30.2

Parameters from APEC with PHABS model fit.

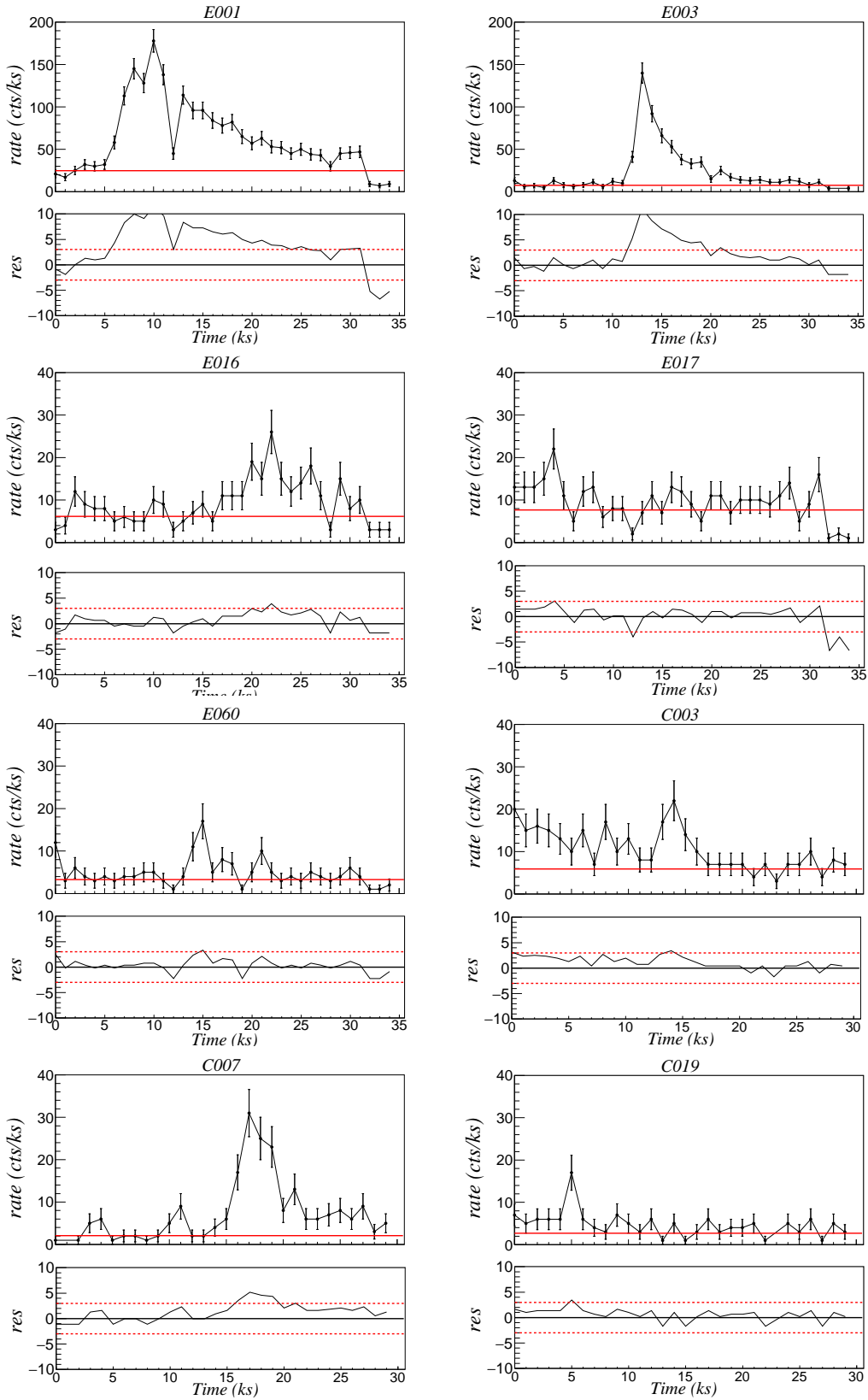


Fig. A.4. XMM-Newton EPIC/pn light curves in the energy band 0.5 -7.3 keV of X-ray sources with flares. In bottom panels are presented the factor $res = \frac{C_i - C_{ch}}{\sigma_i}$. The time bins correspond to 1ks.

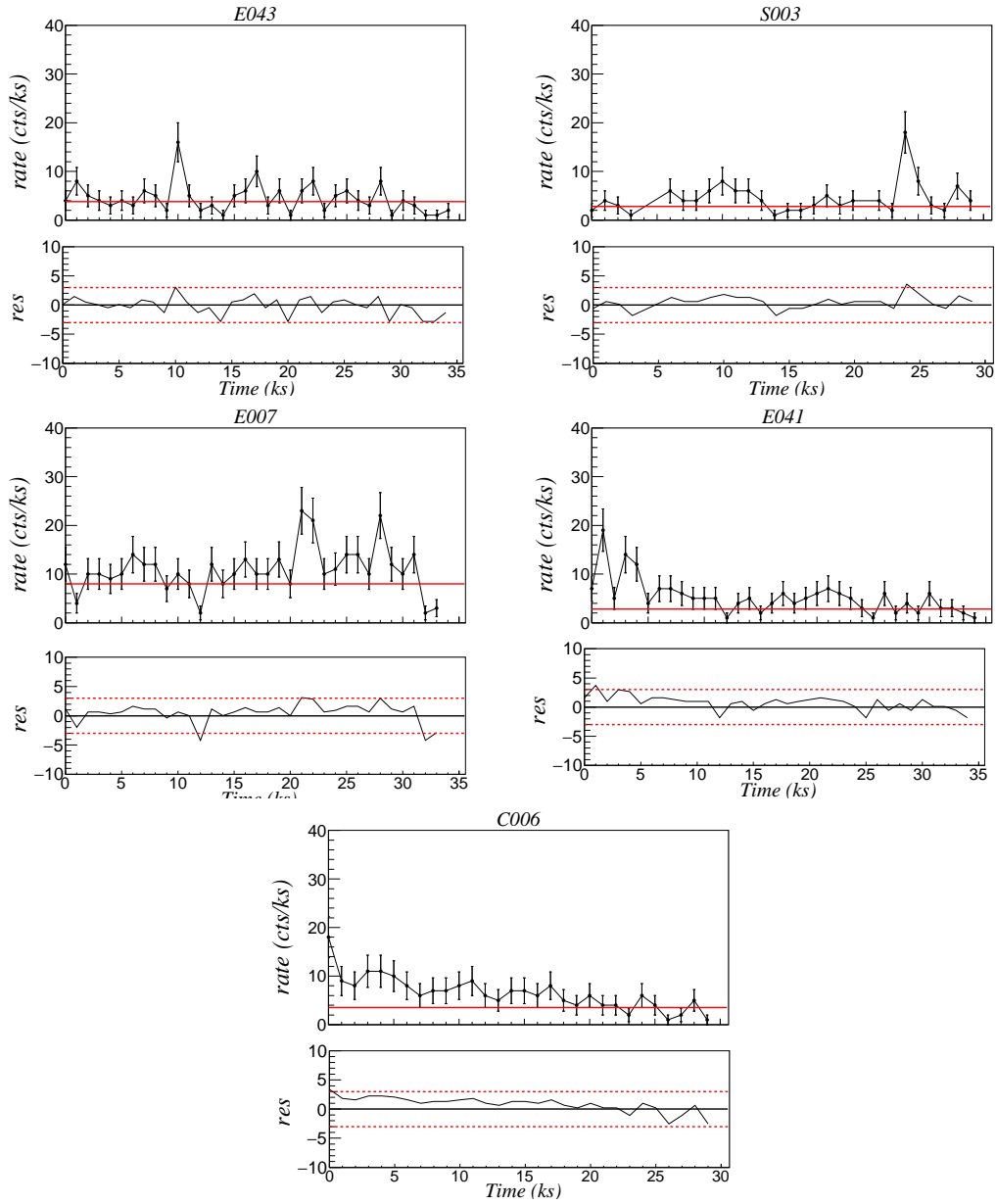


Fig. A.5. *XMM-Newton* EPIC/pn light curves in the energy band 0.5 -7.3 keV of X-ray sources with flares and “partial flares”. In bottom panels are presented the factor $res = \frac{C_i - C_{ch}}{\sigma_i}$. The time bins correspond to 1ks.

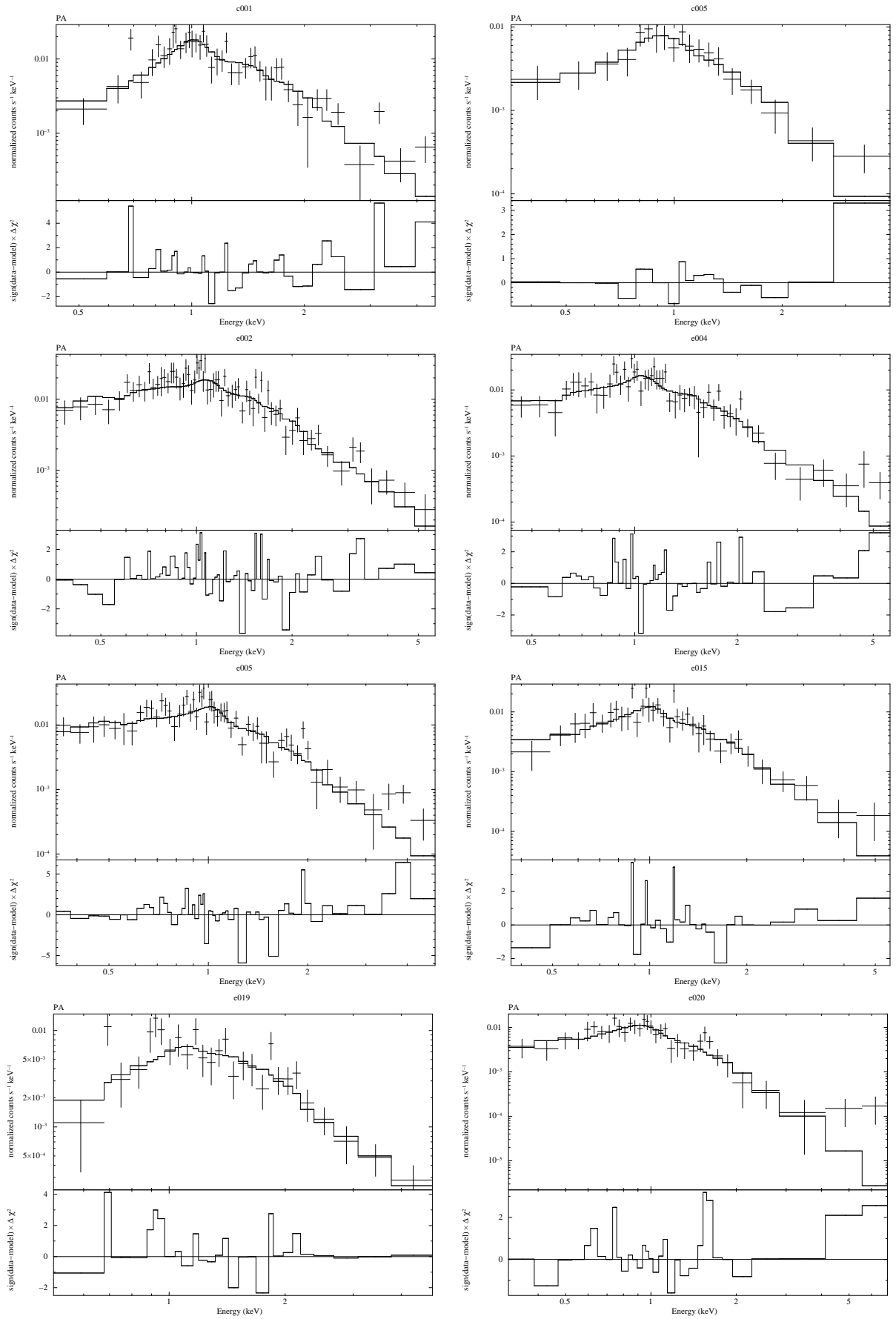


Fig. A.6. Best-fits and residual (see Sect. A.3) obtained for spectra of bright X-ray sources.

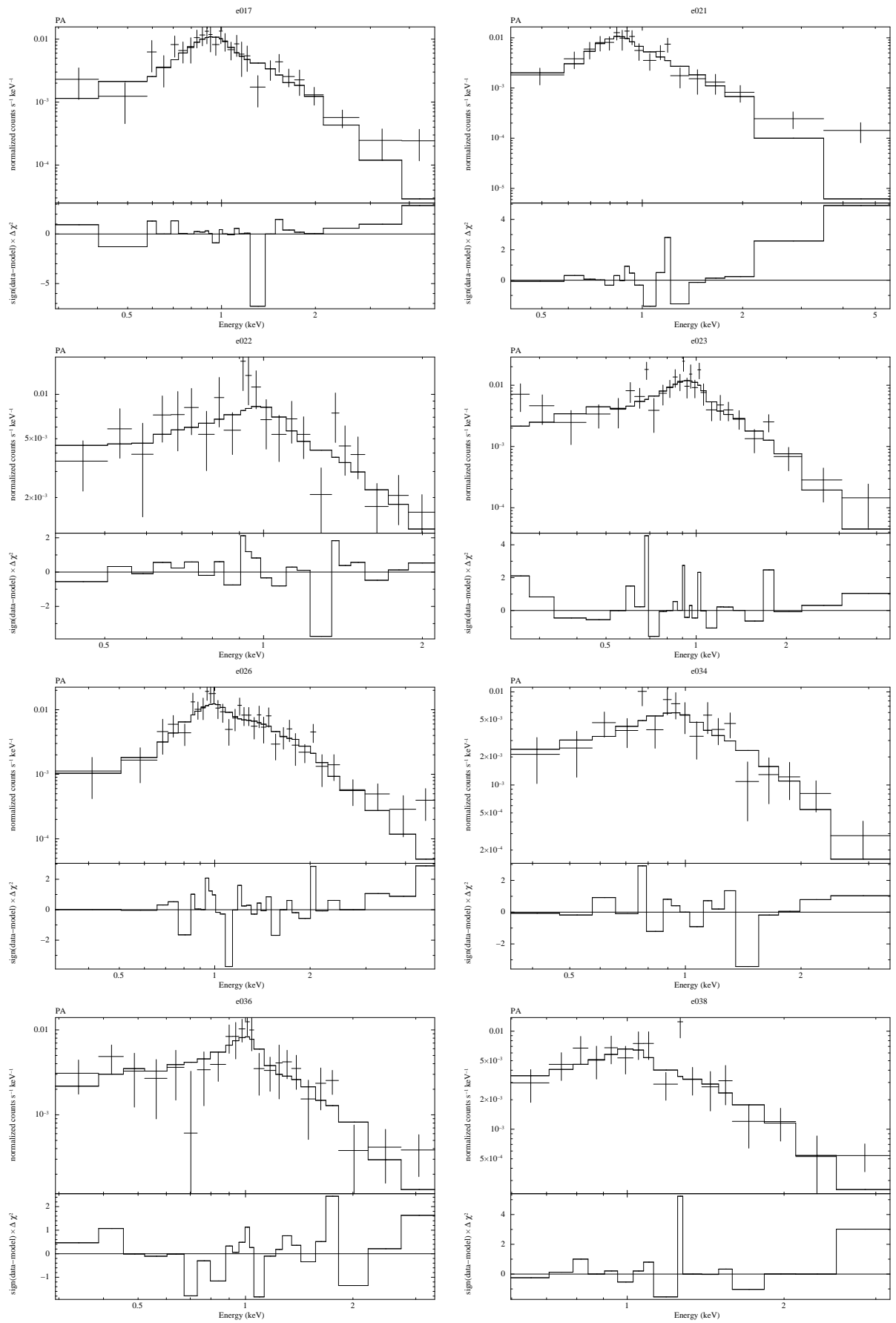


Fig. A.7. The same as Fig. A.7.

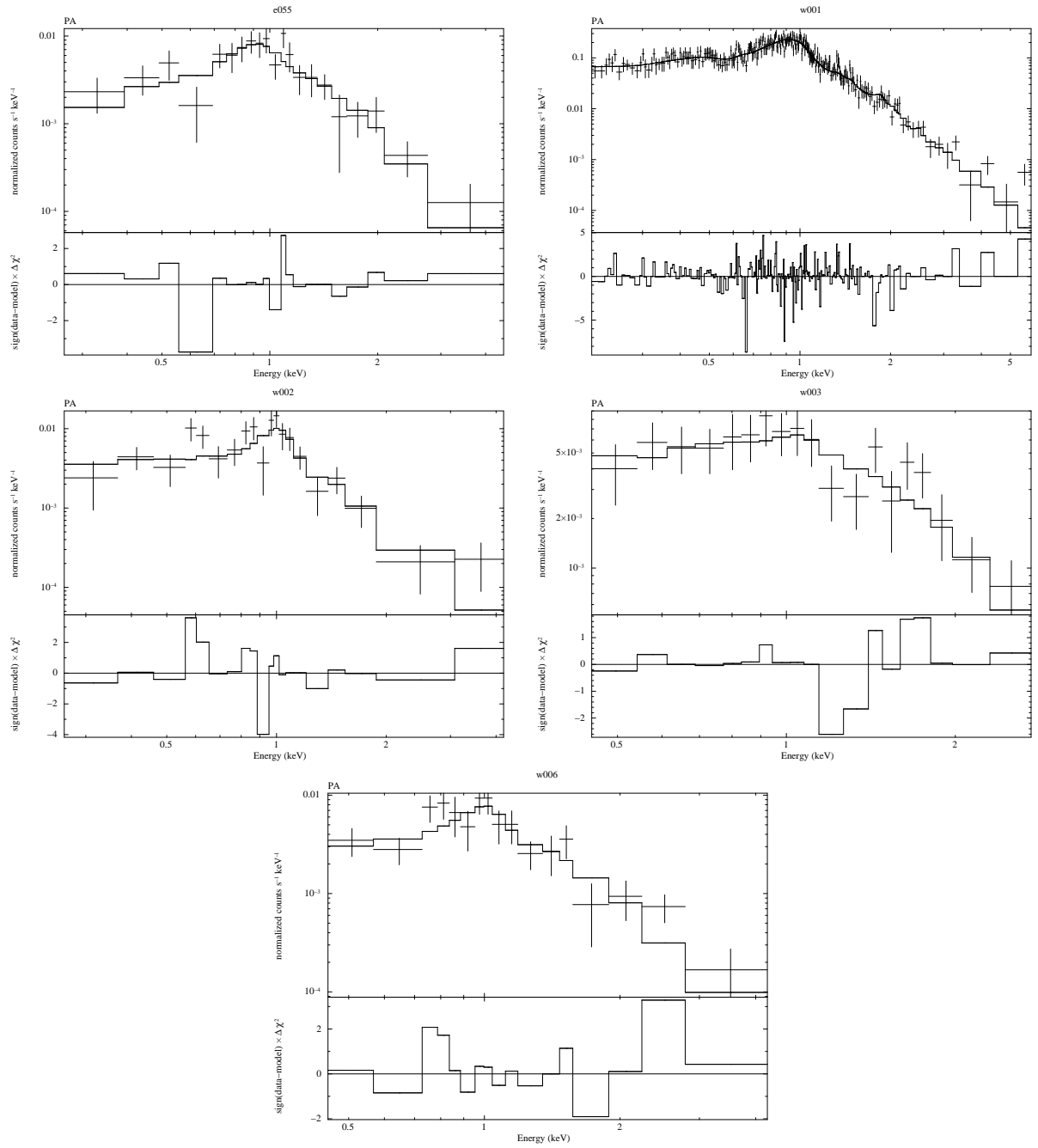


Fig. A.8. The same as Fig. A.7.

Appendix B: Catalogue of X-ray sources

In this section we present all the 387 X-ray sources detected with EPIC cameras PN, MOS1 and MOS2 in tabular form (Table B.1). The infrared counterparts candidates of these sources (2MASS and WISE) are presented in Table B.2.

Table B.1. X-ray sources detected in the combined images of the EPIC cameras PN, MOS1 and MOS2. Column description: (1) X-ray source identification; (2, 3) J_{2000} coordinates (4) Maximum likelihood; (5,6 and 7) Count Rates detected in each EPIC camera PN, MOS1 and MOS2 individually ; (8, 9, 10 and 11) PN hardness ratios.

ID	RA (J2000) (2)	DEC (J2000) (3)	ML (4)	PN ⁽⁵⁾	CR (cts/ks) MOS1 ⁽⁶⁾	MOS2 ⁽⁷⁾	HR ₁ ⁽⁸⁾ 0.5-1.0-2.0 keV	HR ₂ ⁽⁹⁾ 1.0-2.0-7.3 keV	HR ₁ ⁽¹⁰⁾ 0.2-0.5-2.0 keV	HR ₂ ⁽¹¹⁾ 0.5-2.0-4.5 keV
W066	07 00 28.5	-11 21 36.40	26	-	2.2 ± 0.6	2.7 ± 0.6	-	-	-	-
W017	07 00 37.0	-11 23 46.28	111	7.2 ± 1.0	2.8 ± 0.5	3.2 ± 0.6	0.65 ± 0.19	0.23 ± 0.14	1.00 ± 0.11	0.01 ± 0.15
W001	07 00 37.4	-11 14 45.07	18.701	412.1 ± 7.1	117.6 ± 3.0	117.7 ± 3.1	-0.28 ± 0.02	-0.75 ± 0.02	0.63 ± 0.01	-0.91 ± 0.01
W040	07 00 40.2	-11 13 48.51	17	4.6 ± 1.0	-	-	-0.13 ± 0.22	-0.46 ± 0.33	-	-
W002	07 00 43.3	-11 17 15.10	443	16.8 ± 1.3	4.3 ± 0.6	4.4 ± 0.6	-0.25 ± 0.07	-0.76 ± 0.12	0.82 ± 0.05	-0.85 ± 0.05
W048	07 00 47.1	-11 22 02.30	35	2.4 ± 0.5	-	-	-0.52 ± 0.21	-1.00 ± 0.50	0.46 ± 0.17	-0.95 ± 0.11
W042	07 00 48.3	-11 12 37.90	35	3.9 ± 0.8	-	-	0.03 ± 0.21	-0.56 ± 0.30	0.48 ± 0.17	-0.85 ± 0.15
W078	07 00 55.7	-11 26 24.39	17	-	-	1.2 ± 0.3	-	-	-	-
W018	07 00 56.1	-11 21 27.64	109	6.2 ± 0.9	2.1 ± 0.4	1.8 ± 0.4	0.82 ± 0.14	0.15 ± 0.14	0.75 ± 0.18	-0.08 ± 0.15
W061	07 00 56.9	-11 17 51.17	20	2.7 ± 0.6	-	-	0.29 ± 0.29	0.29 ± 0.21	1.00 ± 0.12	-0.20 ± 0.23
W023	07 01 00.5	-11 18 37.80	74	3.7 ± 0.6	-	-	-0.62 ± 0.13	-1.00 ± 0.46	0.72 ± 0.11	-1.00 ± 0.04
W009	07 01 00.8	-11 19 31.06	201	6.1 ± 0.7	-	1.5 ± 0.3	-0.63 ± 0.10	-0.47 ± 0.31	0.50 ± 0.09	-1.00 ± 0.07
W041	07 01 04.1	-11 25 01.41	48	3.2 ± 0.6	-	1.3 ± 0.3	1.00 ± 0.20	0.62 ± 0.14	1.00 ± 0.39	0.52 ± 0.22
W070	07 01 06.8	-11 31 24.01	17	3.2 ± 0.7	-	-	-0.72 ± 0.19	-1.00 ± 1.10	0.93 ± 0.39	-1.00 ± 0.12
W037	07 01 09.6	-11 09 02.50	57	6.7 ± 1.0	2.0 ± 0.5	2.1 ± 0.6	0.49 ± 0.36	0.70 ± 0.12	1.00 ± 0.12	0.39 ± 0.18
W031	07 01 11.2	-11 27 51.41	66	-	-	2.1 ± 0.4	-	-	-	-
W022	07 01 12.2	-11 31 22.52	110	9.0 ± 1.2	-	4.2 ± 0.6	0.75 ± 0.16	0.24 ± 0.13	0.82 ± 0.35	0.20 ± 0.15
W044	07 01 12.2	-11 09 58.53	28	4.0 ± 0.8	-	-	-0.15 ± 0.20	-0.61 ± 0.34	0.87 ± 0.20	-0.90 ± 0.19
W143	07 01 12.2	-11 26 59.01	27	2.6 ± 0.6	-	-	-0.40 ± 0.22	-0.76 ± 0.42	0.73 ± 0.17	-1.00 ± 0.14
W112	07 01 12.6	-11 28 34.63	16	2.1 ± 0.5	-	-	-0.84 ± 0.19	-0.25 ± 1.18	0.57 ± 0.24	-1.00 ± 0.09
W065	07 01 12.6	-11 25 49.65	19	1.8 ± 0.5	-	-	-0.65 ± 0.24	-0.35 ± 0.75	0.94 ± 0.16	-1.00 ± 0.11
W055	07 01 13.8	-11 21 16.95	23	1.8 ± 0.4	-	-	-0.42 ± 0.22	-0.18 ± 0.44	0.49 ± 0.21	-0.68 ± 0.18
W052	07 01 14.2	-11 08 57.23	47	8.1 ± 1.8	1.3 ± 0.4	1.8 ± 0.5	-0.03 ± 0.22	-1.00 ± 0.25	0.97 ± 0.11	-1.00 ± 0.16
W147	07 01 14.5	-11 16 15.98	22	2.6 ± 0.5	-	0.8 ± 0.2	0.52 ± 0.46	0.67 ± 0.17	0.63 ± 0.54	0.50 ± 0.23
W072	07 01 14.6	-11 13 28.95	24	5.8 ± 1.5	-	-	0.92 ± 0.15	-0.73 ± 0.28	-	-
W025	07 01 14.6	-11 20 32.40	87	3.2 ± 0.5	0.5 ± 0.2	0.8 ± 0.2	-0.49 ± 0.13	-1.00 ± 0.16	0.79 ± 0.12	-1.00 ± 0.03
W008	07 01 16.4	-11 25 52.46	241	9.0 ± 0.8	-	2.4 ± 0.4	-0.27 ± 0.09	-0.65 ± 0.15	0.53 ± 0.07	-0.90 ± 0.06
W053	07 01 16.5	-11 09 06.50	20	4.5 ± 0.9	-	-	0.26 ± 0.22	-0.28 ± 0.25	-	-
W149	07 01 16.8	-11 17 59.05	24	1.7 ± 0.4	-	-	0.07 ± 0.21	-0.70 ± 0.33	0.30 ± 0.19	-1.00 ± 0.20
W012	07 01 17.0	-11 23 55.47	184	7.0 ± 0.7	2.5 ± 0.4	1.8 ± 0.3	0.65 ± 0.10	-0.17 ± 0.11	0.95 ± 0.07	-0.46 ± 0.10
W086	07 01 18.0	-11 10 39.93	18	2.8 ± 0.7	-	1.3 ± 0.4	0.95 ± 0.41	0.49 ± 0.22	-	-
W029	07 01 18.1	-11 19 52.12	61	2.5 ± 0.5	-	-	-0.48 ± 0.16	-0.34 ± 0.39	0.76 ± 0.14	-0.98 ± 0.08
W049	07 01 18.8	-11 19 23.32	27	1.0 ± 0.3	0.6 ± 0.2	-	-0.97 ± 0.16	-1.00 ± 9.00	-	-
W019	07 01 19.9	-11 17 30.89	96	4.5 ± 0.6	1.9 ± 0.3	2.3 ± 0.4	0.81 ± 0.13	-0.01 ± 0.13	1.00 ± 0.03	-0.19 ± 0.13
W064	07 01 20.1	-11 26 58.70	21	2.9 ± 0.6	-	-	1.00 ± 0.22	0.41 ± 0.17	1.00 ± 0.14	0.10 ± 0.25
W077	07 01 20.7	-11 11 52.92	18	2.5 ± 0.6	1.2 ± 0.3	-	0.54 ± 0.37	0.34 ± 0.24	1.00 ± 0.14	0.00 ± 0.26
W013	07 01 21.0	-11 06 01.62	246	-	11.2 ± 1.3	16.7 ± 1.8	-	-	-	-
W035	07 01 23.7	-11 27 06.69	50	4.0 ± 0.7	-	-	0.85 ± 0.20	0.35 ± 0.15	0.91 ± 0.16	0.16 ± 0.18
W034	07 01 24.2	-11 24 27.55	28	2.8 ± 0.5	-	0.6 ± 0.2	-0.75 ± 0.15	-0.05 ± 0.53	0.84 ± 0.14	-0.86 ± 0.14
W051	07 01 24.3	-11 09 01.76	53	3.5 ± 0.8	-	-	-0.04 ± 0.21	-0.90 ± 0.33	1.00 ± 0.07	-0.79 ± 0.20
W085	07 01 25.3	-11 22 13.44	16	2.1 ± 0.5	-	-	0.50 ± 0.36	0.44 ± 0.19	1.00 ± 0.14	0.18 ± 0.22
W057	07 01 25.5	-11 15 28.42	16	2.1 ± 0.5	-	-	1.00 ± 0.12	0.31 ± 0.22	1.00 ± 0.27	0.35 ± 0.28
W014	07 01 26.4	-11 17 55.91	150	5.2 ± 0.6	1.1 ± 0.3	1.6 ± 0.3	-0.21 ± 0.11	-0.69 ± 0.20	0.46 ± 0.10	-0.85 ± 0.07
W004	07 01 26.9	-11 28 22.35	483	18.8 ± 1.3	-	5.0 ± 0.6	-0.39 ± 0.07	-0.48 ± 0.12	0.60 ± 0.05	-0.83 ± 0.04
W006	07 01 29.1	-11 21 30.28	276	9.1 ± 0.8	2.0 ± 0.3	2.3 ± 0.3	-0.04 ± 0.09	-0.64 ± 0.12	0.84 ± 0.06	-0.77 ± 0.06
W080	07 01 30.9	-11 13 32.95	18	-	-	-	-	-	-	-
W007	07 01 33.9	-11 10 51.17	271	-	8.3 ± 1.0	6.3 ± 0.8	-	-	-	-
W054	07 01 34.0	-11 23 17.56	24	2.9 ± 0.5	-	-	-0.37 ± 0.16	-1.00 ± 0.43	0.74 ± 0.13	-0.99 ± 0.07
W026	07 01 34.1	-11 25 32.46	78	6.3 ± 0.8	-	0.7 ± 0.3	-0.50 ± 0.12	-0.38 ± 0.26	0.60 ± 0.10	-0.83 ± 0.08
W011	07 01 34.3	-11 17 36.63	221	8.1 ± 1.4	2.9 ± 0.4	2.0 ± 0.4	-0.12 ± 0.17	-0.65 ± 0.25	0.82 ± 0.13	-0.85 ± 0.11
W050	07 01 35.3	-11 15 53.27	28	3.1 ± 0.6	-	-	0.52 ± 0.24	0.11 ± 0.21	0.90 ± 0.21	-0.22 ± 0.20
W033	07 01 36.0	-11 23 06.60	50	-	0.9 ± 0.3	0.8 ± 0.2	-	-	-	-
W096	07 01 37.6	-11 12 37.56	15	2.2 ± 0.5	-	-	-0.01 ± 0.24	-1.00 ± 0.17	0.74 ± 0.21	-1.00 ± 0.10
W076	07 01 38.5	-11 10 15.45	15	3.0 ± 0.8	-	-	-0.29 ± 0.26	-0.16 ± 0.45	-	-
W043	07 01 39.2	-11 16 02.03	47	2.7 ± 0.6	-	1.3 ± 0.3	-1.00 ± 574.88	1.00 ± 0.08	0.00 ± 0.00	1.00 ± 0.22
W015	07 01 39.5	-11 23 25.87	136	7.0 ± 0.8	1.8 ± 0.4	2.0 ± 0.4	0.62 ± 0.12	0.12 ± 0.11	1.00 ± 0.04	-0.20 ± 0.12
W021	07 01 42.4	-11 23 35.44	88	4.4 ± 0.6	1.1 ± 0.3	1.2 ± 0.3	0.02 ± 0.15	-0.52 ± 0.22	0.93 ± 0.09	-0.71 ± 0.12
W024	07 01 46.0	-11 30 33.07	104	7.4 ± 1.1	2.7 ± 0.6	1.6 ± 0.4	-0.05 ± 0.15	-0.64 ± 0.23	1.00 ± 0.03	-0.77 ± 0.11
W038	07 01 46.6	-11 18 11.04	46	2.6 ± 0.6	3.3 ± 0.9	-	0.09 ± 0.21	-0.67 ± 0.34	0.64 ± 0.20	-0.81 ± 0.17
W060	07 01 49.1	-11 13 18.97	22	-	1.3 ± 0.4	-	-	-	-	-
W047	07 01 50.0	-11 18 23.33	35	-	-	1.4 ± 0.4	-	-	-	-
W005	07 01 50.5	-11 16 40.15	331	7.2 ± 1.6	6.8 ± 0.7	5.7 ± 0.7	-0.14 ± 0.22	-0.49 ± 0.35	0.43 ± 0.18	-0.80 ± 0.17
W003	07 01 52.5	-11 20 17.71	444	16.6 ± 1.2	5.0 ± 0.8	5.1 ± 0.6	0.12 ± 0.08	0.10 ± 0.09	0.80 ± 0.05	-0.73 ± 0.06
W016	07 01 52.5	-11 19 07.98	121	6.6 ± 0.9	1.7 ± 0.4	-	0.03 ± 0.12	-1.00 ± 0.15	0.82 ± 0.11	-1.00 ± 0.06
C054	07 01 54.0	-11 29 13.17	31	7.2 ± 1.4	-	-	-0.46 ± 0.19	0.11 ± 0.33	0.50 ± 0.18	-0.63 ± 0.17
W010	07 01 54.1	-11 18 07.12	187	8.0 ± 0.9	2.2 ± 0.5	1.8 ± 0.4	-0.45 ± 0.11	-0.59 ± 0.24	0.26 ± 0.09	-0.89 ± 0.07
W056	07 01 54.1	-11 27 28.15	21	2.9 ± 0.8	1.6 ± 0.5	-	1.00 ± 0.27	-0.14 ± 0.27	-	-
W045	07 01 54.4	-11 22 19.35	30	2.1 ± 0.5	-	-	-0.14 ± 0.24	-0.95 ± 0.30	0.99 ± 0.11	-0.97 ± 0.11
W058	07 01 56.8	-11 22 47.37	24	-	-	-	-	-	-	-
W036	07 01 56.9	-11 24 07.96	54	4.2 ± 0.7	1.1 ± 0.4	-	-0.57 ± 0.15	-0.74 ± 0.44	0.60 ± 0.13	-0.86 ± 0.12
W027	07 01 57.4	-11 06 58.33	96	13.7 ± 1.7	-	-	-0.43 ± 0.11	-0.81 ± 0.24	-	-
W039	07 01 58.4	-11 15 46.60	49	4.9 ± 0.8	-	-	-0.48 ± 0.15	-1.00 ± 0.30	0.72 ± 0.13	-1.00 ± 0.08

Table B.1. Continued. Column description: (1) X-ray source identification; (2, 3) J_{2000} coordinates (4) Maximum likelihood; (5,6 and 7) Count Rates detected in each EPIC camera PN, MOS1 and MOS2 individually ; (8, 9, 10 and 11) PN hardness ratios.

ID CMAx ⁽¹⁾	RA (J2000) (2)	DEC (J2000) (3)	ML (4)	CR (cts/ks)			HR1 ⁽⁸⁾ 0.5-1.0-2.0 keV	HR2 ⁽⁹⁾ 1.0-2.0-7.3 keV	HR1 ⁽¹⁰⁾ 0.2-0.5-2.0 keV	HR2 ⁽¹¹⁾ 0.5-2.0-4.5 keV
				PN ⁽⁵⁾	MOS1 ⁽⁶⁾	MOS2 ⁽⁷⁾				
S012	07 01 58.4	-11 57 39.36	52	6.0 ± 1.1	2.4 ± 0.6	-	0.49 ± 0.21	-0.05 ± 0.19	0.78 ± 0.22	-0.30 ± 0.17
W028	07 02 00.1	-11 27 43.63	68	7.6 ± 1.2	-	2.1 ± 0.5	0.16 ± 0.15	-0.40 ± 0.21	0.86 ± 0.12	-0.74 ± 0.13
S015	07 02 01.1	-11 55 14.63	31	4.7 ± 0.9	1.7 ± 0.4	-	0.32 ± 0.41	0.65 ± 0.16	-0.47 ± 0.16	0.14 ± 0.22
S008	07 02 01.9	-11 45 38.55	103	4.3 ± 0.6	-	0.9 ± 0.3	-0.21 ± 0.13	-0.92 ± 0.17	0.33 ± 0.12	-0.93 ± 0.07
S030	07 02 03.3	-11 40 45.19	16	3.1 ± 0.7	-	-	0.47 ± 0.33	0.41 ± 0.21	1.00 ± 0.46	0.00 ± 0.25
W059	07 02 06.1	-11 14 24.84	19	2.8 ± 0.8	-	2.0 ± 0.6	-0.02 ± 0.28	-0.97 ± 0.46	0.59 ± 0.28	-1.00 ± 0.19
S119	07 02 07.6	-11 36 03.73	20	3.1 ± 0.9	-	-	-0.66 ± 0.27	0.25 ± 0.60	1.00 ± 0.06	-0.80 ± 0.24
S027	07 02 09.7	-11 44 04.21	17	2.4 ± 0.5	-	-	1.00 ± 0.26	0.53 ± 0.18	1.00 ± 0.29	0.34 ± 0.26
S020	07 02 10.3	-11 41 38.58	34	2.5 ± 0.5	1.2 ± 0.3	-	0.12 ± 0.20	-1.00 ± 0.16	1.00 ± 0.06	-1.00 ± 0.11
S013	07 02 11.9	-11 48 47.09	42	3.0 ± 0.5	-	1.2 ± 0.3	0.83 ± 0.27	0.58 ± 0.14	1.00 ± 0.17	0.40 ± 0.19
C078	07 02 12.5	-11 22 37.29	21	3.0 ± 0.8	-	-	-0.06 ± 0.26	-0.55 ± 0.46	-	-
W046	07 02 12.6	-11 24 42.17	36	7.0 ± 1.2	-	1.6 ± 0.5	-0.13 ± 0.18	-0.35 ± 0.28	1.00 ± 0.06	-0.75 ± 0.14
S006	07 02 12.8	-11 46 49.64	20	-	0.6 ± 0.2	-	-	-	-	-
S032	07 02 13.1	-11 42 37.50	16	2.0 ± 0.4	-	-	-0.61 ± 0.18	-1.00 ± 0.65	0.40 ± 0.18	-1.00 ± 0.10
W032	07 02 13.7	-11 21 10.67	51	8.2 ± 1.2	-	3.1 ± 0.7	0.60 ± 0.17	0.05 ± 0.16	1.00 ± 0.03	-0.20 ± 0.16
S044	07 02 15.1	-11 56 44.63	16	-	-	1.2 ± 0.3	-	-	-	-
S010	07 02 16.1	-11 33 54.15	66	5.3 ± 1.0	2.7 ± 0.6	-	0.37 ± 0.21	-0.21 ± 0.23	0.97 ± 0.12	-0.40 ± 0.18
S016	07 02 16.6	-11 50 55.09	42	1.9 ± 0.4	0.6 ± 0.2	0.9 ± 0.2	-0.19 ± 0.22	-0.53 ± 0.40	0.44 ± 0.21	-0.77 ± 0.16
W063	07 02 19.6	-11 13 45.82	32	4.8 ± 1.2	-	-	-0.52 ± 0.20	-1.00 ± 0.98	1.00 ± 0.09	-1.00 ± 0.20
S022	07 02 20.0	-11 48 42.34	24	2.3 ± 0.6	-	1.0 ± 0.3	1.00 ± 0.14	0.25 ± 0.25	-	-
S033	07 02 20.2	-11 47 59.02	16	1.5 ± 0.4	-	-	0.04 ± 0.24	-0.90 ± 0.32	0.19 ± 0.20	-1.00 ± 0.24
S041	07 02 20.6	-11 42 09.19	17	1.5 ± 0.4	-	-	-0.54 ± 0.24	-1.00 ± 0.48	0.17 ± 0.21	-1.00 ± 0.14
C100	07 02 21.8	-11 15 19.54	23	4.9 ± 1.1	-	-	-0.08 ± 0.23	-0.56 ± 0.40	0.55 ± 0.19	-0.93 ± 0.14
C066	07 02 22.0	-11 26 39.11	28	4.6 ± 0.8	-	-	0.76 ± 0.20	0.07 ± 0.19	0.43 ± 0.24	0.01 ± 0.18
W030	07 02 22.2	-11 21 22.65	62	12.7 ± 1.7	-	-	0.47 ± 0.13	-0.32 ± 0.15	0.78 ± 0.13	-0.60 ± 0.12
S025	07 02 22.9	-11 39 04.14	23	2.4 ± 0.6	-	-	-0.01 ± 0.22	-1.00 ± 0.54	1.00 ± 0.14	-0.85 ± 0.18
S019	07 02 23.2	-11 43 07.40	37	2.5 ± 0.5	-	-	0.31 ± 0.18	-0.68 ± 0.27	0.68 ± 0.18	-0.94 ± 0.11
W020	07 02 23.9	-11 24 56.07	131	21.7 ± 2.3	-	1.1 ± 0.3	0.25 ± 0.11	-0.29 ± 0.13	0.78 ± 0.09	-0.59 ± 0.09
W068	07 02 24.9	-11 16 10.52	32	6.9 ± 1.4	3.1 ± 0.8	-	0.81 ± 0.79	0.88 ± 0.13	-	-
S005	07 02 26.3	-11 55 06.74	95	9.5 ± 0.9	-	2.1 ± 0.4	0.82 ± 0.10	0.27 ± 0.10	1.00 ± 0.04	0.06 ± 0.11
C136	07 02 26.4	-11 34 09.10	17	3.8 ± 0.8	-	-	-1.00 ± 0.46	1.00 ± 0.06	-1.00 ± 5.33	1.00 ± 0.28
S114	07 02 27.4	-11 54 08.06	37	3.7 ± 0.6	-	1.0 ± 0.3	0.35 ± 0.40	0.67 ± 0.15	1.00 ± 0.17	0.41 ± 0.20
C080	07 02 27.5	-11 34 58.50	22	3.4 ± 1.0	-	0.9 ± 0.4	-0.70 ± 0.25	-1.00 ± 1.33	0.48 ± 0.23	-1.00 ± 0.13
C056	07 02 28.1	-11 31 00.58	21	2.5 ± 0.6	-	-	0.42 ± 0.23	-0.79 ± 0.29	1.00 ± 0.10	-1.00 ± 0.09
C090	07 02 30.0	-11 39 14.20	21	4.0 ± 1.0	-	-	-0.78 ± 0.21	0.41 ± 0.55	-0.06 ± 0.27	-1.00 ± 0.23
C011	07 02 30.4	-11 22 22.08	231	9.0 ± 0.9	2.1 ± 0.4	2.0 ± 0.4	-0.59 ± 0.09	-0.61 ± 0.26	0.63 ± 0.07	-0.95 ± 0.05
C062	07 02 30.6	-11 19 03.50	28	3.9 ± 0.8	-	-	0.19 ± 0.21	-0.27 ± 0.29	1.00 ± 0.04	-0.58 ± 0.21
S039	07 02 33.8	-11 47 41.20	17	1.8 ± 0.4	-	-	1.00 ± 0.21	0.54 ± 0.19	0.13 ± 0.55	0.51 ± 0.25
S021	07 02 33.8	-11 51 09.84	36	2.7 ± 0.5	1.0 ± 0.3	1.4 ± 0.3	1.00 ± 0.15	0.51 ± 0.17	0.55 ± 0.48	0.47 ± 0.23
S029	07 02 33.9	-11 57 21.87	24	2.9 ± 0.7	-	-	0.39 ± 0.40	0.30 ± 0.25	-	-
C012	07 02 36.2	-11 24 57.85	199	7.2 ± 0.8	2.1 ± 0.4	2.5 ± 0.4	0.03 ± 0.10	-0.83 ± 0.13	0.63 ± 0.09	-0.94 ± 0.05
C064	07 02 36.6	-11 35 05.51	29	3.8 ± 0.8	-	-	0.61 ± 0.21	-0.05 ± 0.21	0.81 ± 0.21	-0.23 ± 0.19
C019	07 02 36.6	-11 28 10.03	139	6.6 ± 0.8	2.5 ± 0.4	2.0 ± 0.4	0.02 ± 0.12	-0.60 ± 0.16	0.88 ± 0.07	-0.79 ± 0.08
C041	07 02 40.0	-11 28 24.06	65	3.0 ± 0.5	1.3 ± 0.3	1.4 ± 0.3	-0.18 ± 0.17	-0.89 ± 0.28	1.00 ± 0.04	-0.85 ± 0.14
C048	07 02 41.2	-11 34 07.10	64	6.1 ± 1.2	-	2.4 ± 0.5	0.75 ± 0.29	0.45 ± 0.18	-	-
C042	07 02 42.3	-11 28 03.21	48	3.4 ± 0.6	-	1.0 ± 0.3	0.03 ± 0.17	-0.63 ± 0.24	0.93 ± 0.10	-0.77 ± 0.12
C009	07 02 42.6	-11 27 09.23	137	-	3.2 ± 0.5	2.7 ± 0.4	-	-	-	-
C035	07 02 43.1	-11 25 54.89	61	3.4 ± 0.5	1.0 ± 0.3	0.9 ± 0.3	0.05 ± 0.16	-0.64 ± 0.22	1.00 ± 0.07	-0.75 ± 0.12
C026	07 02 43.7	-11 23 47.77	110	5.4 ± 0.7	1.5 ± 0.3	1.7 ± 0.3	-0.19 ± 0.12	-0.45 ± 0.21	0.93 ± 0.07	-0.71 ± 0.10
C001	07 02 43.9	-11 27 27.25	1,515	31.4 ± 1.5	10.0 ± 0.7	10.6 ± 0.7	0.16 ± 0.05	-0.41 ± 0.06	0.92 ± 0.02	-0.65 ± 0.04
S018	07 02 44.3	-11 41 07.08	41	2.5 ± 0.5	-	-	-0.74 ± 0.17	-1.00 ± 1.29	0.56 ± 0.17	-0.90 ± 0.15
C124	07 02 44.4	-11 20 28.30	15	2.1 ± 0.5	-	-	-0.29 ± 0.21	-0.83 ± 0.47	0.70 ± 0.23	-1.00 ± 0.08
C013	07 02 45.0	-11 35 13.07	208	7.6 ± 0.9	3.2 ± 0.7	3.0 ± 0.5	-0.48 ± 0.10	-1.00 ± 0.29	0.60 ± 0.08	-0.95 ± 0.06
C015	07 02 46.0	-11 28 03.77	147	11.6 ± 1.5	1.5 ± 0.3	1.2 ± 0.3	-0.11 ± 0.13	-0.34 ± 0.19	0.62 ± 0.10	-0.68 ± 0.10
C023	07 02 46.4	-11 26 56.13	109	5.5 ± 0.7	1.1 ± 0.3	1.5 ± 0.3	0.20 ± 0.13	-0.41 ± 0.14	1.00 ± 0.05	-0.61 ± 0.09
C033	07 02 46.5	-11 32 58.69	95	4.8 ± 0.7	1.1 ± 0.3	1.7 ± 0.4	-0.07 ± 0.14	-0.45 ± 0.21	0.72 ± 0.12	-0.74 ± 0.11
C020	07 02 47.5	-11 25 07.77	125	-	2.6 ± 0.4	2.3 ± 0.4	-	-	1.00 ± 0.17	-0.14 ± 0.23
C058	07 02 47.6	-11 37 26.21	33	3.0 ± 0.7	-	-	-0.43 ± 0.24	-1.00 ± 0.57	1.00 ± 0.07	-0.93 ± 0.11
C075	07 02 47.6	-11 22 59.03	22	1.5 ± 0.3	-	-	-0.89 ± 0.17	-1.00 ± 1.65	0.84 ± 0.18	-1.00 ± 0.06
C021	07 02 48.2	-11 18 16.47	149	9.0 ± 1.0	-	2.8 ± 0.5	-0.31 ± 0.11	-0.68 ± 0.21	0.87 ± 0.08	-0.92 ± 0.07
C017	07 02 48.3	-11 24 22.31	108	-	2.0 ± 0.4	1.8 ± 0.3	-	-	-	-
C050	07 02 48.8	-11 17 51.15	27	3.4 ± 0.7	-	2.5 ± 0.5	0.50 ± 0.28	0.15 ± 0.23	1.00 ± 0.10	-0.05 ± 0.21
C027	07 02 49.1	-11 30 37.50	90	4.5 ± 0.6	1.0 ± 0.3	1.0 ± 0.3	0.04 ± 0.14	-0.41 ± 0.18	0.67 ± 0.14	-0.66 ± 0.11
C030	07 02 49.3	-11 25 45.34	85	4.2 ± 0.6	-	1.2 ± 0.3	0.09 ± 0.14	-0.50 ± 0.19	1.00 ± 0.05	-0.73 ± 0.11
C117	07 02 49.8	-11 19 37.34	16	1.7 ± 0.4	-	-	-0.77 ± 0.22	-1.00 ± 1.33	0.88 ± 0.17	-1.00 ± 0.10
C003	07 02 50.1	-11 24 32.29	852	19.9 ± 1.1	5.9 ± 0.6	5.6 ± 0.5	0.37 ± 0.06	-0.34 ± 0.06	0.94 ± 0.03	-0.54 ± 0.05
S011	07 02 50.4	-11 53 43.58	80	3.8 ± 0.8	-	9.4 ± 1.5	0.06 ± 0.22	-0.30 ± 0.30	0.85 ± 0.17	-0.74 ± 0.18
S002	07 02 51.0	-11 45 54.02	169	4.9 ± 0.8	-	2.0 ± 0.5	-0.21 ± 0.17	-0.81 ± 0.27	0.70 ± 0.14	-1.00 ± 0.13
C102	07 02 52.2	-11 17 08.24	20	4.0 ± 0.8	-	-	0.44 ± 0.33	0.47 ± 0.17	1.00 ± 0.06	0.26 ± 0.19
S014	07 02 52.3	-11 53 41.63	33	-	-	-	-	-	-	-
C022	07 02 52.8	-11 27 03.23	119	4.1 ± 0.5	-	1.6 ± 0.3	0.11 ± 0.12	-0.83 ± 0.18	0.88 ± 0.09	-1.00 ± 0.03
C052	07 02 53.1	-11 30 06.86	30	2.8 ± 0.5	-	-	0.60 ± 0.18	-0.18 ± 0.19	0.99 ± 0.09	-0.37 ± 0.16
S007	07 02 53.1	-11 54 17.32	121	-	-	3.0 ± 0.6	-	-	-	-
C039	07 02 53.2	-11 30 51.29	74	3.9 ± 0.6	1.1 ± 0.3	1.3 ± 0.3	0.22 ± 0.14	-0.57 ± 0.18	1.00 ± 0.04	-0.76 ± 0.11
C044	07 02 54.3	-11 25 15.38	35	3.2 ± 0.5	-	0.8 ± 0.2	0.16 ± 0.17	-0.44 ± 0.22	0.63 ± 0.14	-0.67 ± 0.13
C004	07 02 56.0	-11 28 28.58	539	13.8 ± 0.9	5.8 ± 0.6	5.0 ± 0.5	0.61 ± 0.07	-0.23 ± 0.07	1.00 ± 0.02	-0.38 ± 0.06
C028	07 02 56.3	-11 22 17.53	92	2.3 ± 0.6	1.8 ± 0.5	1.6 ± 0.3	-0.22 ± 0.23	-1.00 ± 0.61	0.86 ± 0.18	-1.00 ± 0.18
C061	07 02 56.7	-11 22 01.54	17	-	-	1.1 ± 0.3	-	-	-	-
C119	07 02 57.3	-11 20 36.05	19	5.2 ± 1.4	-	1.1 ± 0.3	-0.26 ± 0.27	-0.89 ± 0.41	1.00 ± 0.15	-1.00 ± 0.15
S001	07 02 57.9	-11 46 23.30	379	12.2 ± 1.2	3.1 ± 0.5	3.6 ± 0.5	-0.78 ± 0.07	-0.98 ± 0.22	0.75 ± 0.07	-0.99 ± 0.02
S017	07 02 57.9	-11 54 28.52	47	6.4 ± 1.2	1.7 ± 0.5	-	-0.16 ± 0.35	0.66 ± 0.17	1.00 ± 0.12	0.13 ± 0.22

Table B.1. Continued. Column description: (1) X-ray source identification; (2, 3) J_{2000} coordinates (4) Maximum likelihood; (5,6 and 7) Count Rates detected in each EPIC camera PN, MOS1 and MOS2 individually ; (8, 9, 10 and 11) PN hardness ratios.

ID CMax ⁽¹⁾	RA (J2000) (2)	DEC (J2000) (3)	ML (4)	PN ⁽⁵⁾	CR (cts/ks) MOS1 ⁽⁶⁾	MOS2 ⁽⁷⁾	HR1 ⁽⁸⁾ 0.5-1.0-2.0 keV	HR2 ⁽⁹⁾ 1.0-2.0-7.3 keV	HR1 ⁽¹⁰⁾ 0.2-0.5-2.0 keV	HR2 ⁽¹¹⁾ 0.5-2.0-4.5 keV
C037	07 02 58.3	-11 28 41.26	59	-	-	1.3 ± 0.3	-	-	-	-
S028	07 02 59.0	-11 43 30.88	21	1.8 ± 0.6	-	-	-0.38 ± 0.29	-0.51 ± 0.61	-	-
C034	07 02 59.1	-11 30 02.27	70	3.5 ± 0.5	0.9 ± 0.2	-	0.60 ± 0.18	0.07 ± 0.15	1.00 ± 0.11	-0.16 ± 0.15
C008	07 02 59.2	-11 27 23.47	438	11.1 ± 0.8	3.9 ± 0.6	3.3 ± 0.4	0.10 ± 0.07	-0.63 ± 0.09	1.00 ± 0.01	-0.77 ± 0.05
C065	07 02 59.4	-11 31 57.42	17	1.6 ± 0.4	-	-	0.40 ± 2.85	0.97 ± 0.10	-0.75 ± 0.54	0.92 ± 0.19
C126	07 02 60.0	-11 39 44.28	16	3.7 ± 0.9	-	-	1.00 ± 0.31	0.45 ± 0.21	-	-
C006	07 03 00.7	-11 26 22.03	314	9.3 ± 0.8	3.2 ± 0.4	3.6 ± 0.4	0.37 ± 0.09	-0.02 ± 0.09	1.00 ± 0.05	-0.29 ± 0.08
C082	07 03 00.7	-11 22 46.20	19	1.9 ± 0.4	-	-	0.46 ± 0.19	-0.78 ± 0.26	1.00 ± 0.13	-0.89 ± 0.15
S023	07 03 02.1	-11 43 53.41	32	2.2 ± 0.6	-	-	-0.62 ± 0.23	-1.00 ± 0.89	0.62 ± 0.27	-1.00 ± 0.15
C091	07 03 02.6	-11 28 19.24	15	-	-	-	-	-	-	-
C002	07 03 02.9	-11 26 23.63	1,203	20.0 ± 1.0	7.4 ± 0.6	7.0 ± 0.6	0.21 ± 0.05	-0.54 ± 0.06	0.95 ± 0.02	-0.68 ± 0.04
C024	07 03 03.1	-11 25 49.48	76	2.8 ± 0.5	1.2 ± 0.3	0.8 ± 0.2	-0.75 ± 0.14	-0.45 ± 0.60	0.87 ± 0.12	-1.00 ± 0.07
C063	07 03 03.5	-11 24 45.75	21	-	-	-	-	-	-	-
C045	07 03 03.5	-11 19 14.68	22	2.4 ± 0.6	-	-	-0.55 ± 0.25	0.44 ± 0.33	1.00 ± 0.31	-0.29 ± 0.22
C040	07 03 04.6	-11 21 53.65	81	6.1 ± 0.7	-	-	1.00 ± 0.12	0.23 ± 0.11	1.00 ± 0.03	0.08 ± 0.12
S031	07 03 06.7	-11 57 50.49	18	5.1 ± 1.2	-	-	0.14 ± 0.24	-0.15 ± 0.29	1.00 ± 0.08	-0.50 ± 0.23
S004	07 03 07.6	-11 39 35.63	123	12.3 ± 1.5	4.0 ± 0.8	5.3 ± 0.9	0.17 ± 0.13	-0.29 ± 0.15	0.81 ± 0.10	-0.59 ± 0.10
S003	07 03 08.0	-11 53 06.10	157	9.1 ± 1.1	3.0 ± 0.6	2.2 ± 0.5	-0.45 ± 0.11	-1.00 ± 0.32	0.54 ± 0.10	-0.97 ± 0.06
C060	07 03 08.9	-11 25 56.97	27	2.0 ± 0.4	0.8 ± 0.2	1.0 ± 0.3	0.57 ± 0.26	0.06 ± 0.22	1.00 ± 0.11	-0.40 ± 0.23
C036	07 03 09.9	-11 16 10.39	79	9.1 ± 1.1	-	2.0 ± 0.5	-0.09 ± 0.12	-0.64 ± 0.17	1.00 ± 0.04	-0.74 ± 0.11
C073	07 03 11.1	-11 39 23.43	46	-	24.3 ± 4.2	-	-	-	-	-
C025	07 03 11.4	-11 35 11.37	109	5.9 ± 0.8	1.8 ± 0.4	2.0 ± 0.5	0.27 ± 0.13	-0.62 ± 0.16	1.00 ± 0.06	-0.79 ± 0.09
C031	07 03 11.8	-11 30 13.17	84	3.4 ± 0.5	0.8 ± 0.2	1.0 ± 0.3	0.14 ± 0.14	-0.74 ± 0.20	0.97 ± 0.07	-0.79 ± 0.11
C074	07 03 12.2	-11 24 32.00	27	-	-	1.1 ± 0.3	-	-	-	-
C029	07 03 12.7	-11 28 37.97	81	4.3 ± 0.6	1.3 ± 0.3	0.9 ± 0.3	0.56 ± 0.13	-0.31 ± 0.15	0.76 ± 0.13	-0.47 ± 0.12
C097	07 03 15.4	-11 28 19.18	17	1.9 ± 0.5	0.8 ± 0.2	-	0.72 ± 0.20	-0.82 ± 0.21	0.75 ± 0.19	-0.88 ± 0.15
S024	07 03 16.8	-11 54 01.41	22	5.8 ± 1.2	-	-	0.01 ± 0.22	-0.33 ± 0.31	0.64 ± 0.19	-0.51 ± 0.18
C107	07 03 18.3	-11 35 11.90	16	-	1.2 ± 0.4	-	-	-	-	-
C072	07 03 20.0	-11 28 00.95	28	2.2 ± 0.5	-	-	0.16 ± 0.20	-0.52 ± 0.29	1.00 ± 0.18	-0.59 ± 0.18
C086	07 03 22.7	-11 38 26.06	22	3.6 ± 0.9	-	-	0.76 ± 0.37	0.43 ± 0.21	-	-
C114	07 03 23.3	-11 29 14.17	16	-	-	-	-	-	-	-
C067	07 03 26.2	-11 34 59.95	21	3.1 ± 0.7	-	1.3 ± 0.4	-0.26 ± 0.20	-0.40 ± 0.39	0.66 ± 0.18	-0.85 ± 0.17
C059	07 03 26.2	-11 23 34.67	21	1.6 ± 0.4	-	-	-0.15 ± 0.23	-1.00 ± 0.40	1.00 ± 0.09	-0.98 ± 0.17
C053	07 03 27.3	-11 32 51.19	33	3.4 ± 0.6	-	1.3 ± 0.4	0.79 ± 0.17	-0.31 ± 0.18	0.55 ± 0.21	-0.41 ± 0.16
E175	07 03 30.3	-11 32 00.92	31	2.4 ± 0.6	1.9 ± 0.5	1.6 ± 0.4	0.38 ± 0.28	-0.13 ± 0.26	0.77 ± 0.22	-0.49 ± 0.21
S009	07 03 31.5	-11 48 11.62	97	14.3 ± 1.9	-	-	-0.23 ± 0.13	-0.46 ± 0.23	0.39 ± 0.11	-0.86 ± 0.09
C046	07 03 32.8	-11 32 11.34	64	4.1 ± 0.7	-	1.3 ± 0.4	-0.64 ± 0.14	-0.26 ± 0.44	0.56 ± 0.13	-0.86 ± 0.13
C032	07 03 33.1	-11 17 49.57	106	10.1 ± 1.2	-	2.8 ± 0.6	-0.12 ± 0.13	-0.30 ± 0.18	1.00 ± 0.10	-0.81 ± 0.12
E051	07 03 33.5	-11 34 25.92	198	9.6 ± 1.1	1.4 ± 0.4	2.2 ± 0.5	0.08 ± 0.11	-0.64 ± 0.14	0.90 ± 0.09	-0.88 ± 0.07
E118	07 03 34.5	-11 35 04.95	27	3.4 ± 0.7	-	-	-0.04 ± 0.19	-0.64 ± 0.31	1.00 ± 0.13	-0.86 ± 0.14
C071	07 03 34.7	-11 27 50.35	17	1.4 ± 0.4	-	-	-0.68 ± 0.29	-1.00 ± 0.56	-	-
C005	07 03 35.5	-11 26 19.75	478	13.6 ± 1.1	4.7 ± 0.6	5.2 ± 0.6	1.01 ± 0.08	-0.66 ± 0.10	0.85 ± 0.05	-0.81 ± 0.05
C018	07 03 36.2	-11 27 51.74	160	7.6 ± 0.9	2.9 ± 0.5	3.6 ± 0.6	0.00 ± 0.11	0.59 ± 0.10	1.00 ± 0.08	0.46 ± 0.12
C007	07 03 37.2	-11 31 12.44	379	16.3 ± 1.3	5.2 ± 0.7	4.8 ± 0.7	0.19 ± 0.09	-0.07 ± 0.09	0.71 ± 0.07	-0.41 ± 0.07
E076	07 03 38.6	-11 42 48.31	92	6.4 ± 1.0	2.8 ± 0.6	2.6 ± 0.5	0.18 ± 0.16	-0.36 ± 0.19	1.00 ± 0.10	-0.59 ± 0.13
E095	07 03 38.9	-11 37 18.91	54	4.5 ± 0.7	1.5 ± 0.4	1.4 ± 0.3	0.08 ± 0.17	-0.53 ± 0.23	0.81 ± 0.13	-0.78 ± 0.14
C055	07 03 39.0	-11 27 55.86	36	4.0 ± 0.7	-	1.4 ± 0.4	0.82 ± 0.18	-0.14 ± 0.18	1.00 ± 0.04	-0.31 ± 0.17
E131	07 03 39.5	-11 32 03.96	20	2.2 ± 0.5	-	-	-0.09 ± 0.22	-0.82 ± 0.35	1.00 ± 0.16	-0.85 ± 0.18
C057	07 03 40.0	-11 29 46.63	30	2.5 ± 0.6	-	1.2 ± 0.4	-0.55 ± 0.23	-0.25 ± 0.63	0.75 ± 0.24	-0.91 ± 0.16
C043	07 03 40.5	-11 23 28.00	54	5.0 ± 0.8	1.4 ± 0.4	1.4 ± 0.4	-0.11 ± 0.17	-0.24 ± 0.25	0.95 ± 0.09	-0.57 ± 0.15
E086	07 03 42.1	-11 35 12.69	68	4.0 ± 0.6	2.1 ± 0.6	1.5 ± 0.4	0.12 ± 0.15	-0.83 ± 0.21	0.85 ± 0.12	-0.78 ± 0.13
E220	07 03 43.1	-11 38 12.12	16	-	1.1 ± 0.3	-	-	-	-	-
E046	07 03 43.3	-11 33 06.00	202	9.1 ± 0.9	2.7 ± 0.4	2.3 ± 0.5	-0.08 ± 0.10	-0.57 ± 0.15	0.82 ± 0.07	-0.79 ± 0.08
E083	07 03 45.4	-11 29 19.57	53	-	2.2 ± 0.5	2.2 ± 0.5	-	-	-	-
E336	07 03 45.9	-11 39 16.22	15	-	1.4 ± 0.4	-	-	-	-	-
E077	07 03 46.0	-11 29 41.40	83	14.3 ± 1.5	1.5 ± 0.4	-	0.26 ± 0.11	-0.34 ± 0.14	0.50 ± 0.10	-0.52 ± 0.10
C016	07 03 46.1	-11 23 59.07	168	10.7 ± 1.2	-	3.6 ± 0.6	0.33 ± 0.11	-0.57 ± 0.14	0.87 ± 0.07	-0.68 ± 0.09
E133	07 03 47.4	-11 45 08.64	32	4.5 ± 0.9	-	1.8 ± 0.4	0.91 ± 0.27	0.48 ± 0.18	1.00 ± 0.93	0.20 ± 0.28
C051	07 03 47.5	-11 31 45.73	19	-	3.2 ± 0.5	2.0 ± 0.5	-	-	-	-
E173	07 03 47.6	-11 27 30.33	19	2.6 ± 0.7	-	-	0.33 ± 0.23	-1.00 ± 0.35	0.53 ± 0.20	-1.00 ± 0.09
E115	07 03 48.5	-11 37 32.25	37	3.0 ± 0.6	-	1.4 ± 0.3	0.48 ± 0.25	0.26 ± 0.19	0.74 ± 0.27	-0.05 ± 0.20
E039	07 03 48.6	-11 31 49.24	405	22.3 ± 1.4	2.1 ± 0.4	8.7 ± 1.0	-0.06 ± 0.06	-0.72 ± 0.09	0.61 ± 0.05	-0.88 ± 0.04
E023	07 03 49.0	-11 41 52.15	667	20.8 ± 1.4	7.0 ± 0.7	5.0 ± 0.6	-0.23 ± 0.07	-0.51 ± 0.10	0.71 ± 0.05	-0.84 ± 0.04
E061	07 03 50.0	-11 32 14.08	107	3.9 ± 0.7	-	2.2 ± 0.4	-0.03 ± 0.19	-0.50 ± 0.25	0.48 ± 0.16	-0.78 ± 0.13
E157	07 03 50.1	-11 27 37.66	18	2.8 ± 0.7	-	-	-0.08 ± 0.30	0.13 ± 0.29	-	-
E011	07 03 51.6	-11 34 54.09	943	32.1 ± 2.7	8.0 ± 0.6	7.0 ± 0.6	-0.03 ± 0.09	-0.67 ± 0.11	0.76 ± 0.06	-0.82 ± 0.06
E119	07 03 51.7	-11 40 00.55	21	3.1 ± 0.6	-	-	-0.07 ± 0.23	0.06 ± 0.25	0.53 ± 0.19	-0.34 ± 0.18
E190	07 03 52.5	-11 23 12.82	20	3.7 ± 0.9	1.9 ± 0.6	-	-0.37 ± 0.22	-1.00 ± 0.61	1.00 ± 0.21	-1.00 ± 0.14
E142	07 03 52.6	-11 39 05.63	18	1.6 ± 0.4	-	-	-0.35 ± 0.23	-0.99 ± 0.34	0.62 ± 0.21	-1.00 ± 0.12
E161	07 03 52.6	-11 26 12.52	22	3.4 ± 0.7	-	2.2 ± 0.5	-0.02 ± 0.22	-0.41 ± 0.30	0.44 ± 0.20	-0.81 ± 0.16
E104	07 03 52.8	-11 40 15.69	54	4.4 ± 0.7	-	1.0 ± 0.3	0.20 ± 0.15	-0.58 ± 0.22	0.83 ± 0.11	-0.67 ± 0.13
E065	07 03 53.1	-11 29 33.99	106	7.7 ± 1.0	8.5 ± 1.1	8.2 ± 1.0	-0.07 ± 0.13	-0.46 ± 0.18	0.47 ± 0.12	-0.78 ± 0.10
E107	07 03 53.5	-11 34 46.49	21	2.3 ± 0.5	-	-	0.09 ± 0.25	-0.24 ± 0.30	1.00 ± 0.07	-0.57 ± 0.21
E056	07 03 54.0	-11 32 47.92	121	3.7 ± 0.6	1.6 ± 0.3	1.3 ± 0.3	-0.22 ± 0.16	-0.95 ± 0.21	0.85 ± 0.12	-0.88 ± 0.12
E074	07 03 54.7	-11 36 04.77	77	4.3 ± 0.6	-	-	0.01 ± 0.13	-0.78 ± 0.18	0.84 ± 0.09	-0.88 ± 0.08
E015	07 03 54.8	-11 28 18.67	853	22.6 ± 1.5	8.6 ± 0.8	8.6 ± 1.0	0.02 ± 0.07	-0.56 ± 0.08	0.84 ± 0.05	-0.81 ± 0.05
E072	07 03 55.0	-11 34 34.08	96	4.8 ± 0.6	1.1 ± 0.3	1.7 ± 0.4	-0.12 ± 0.13	-0.72 ± 0.19	0.96 ± 0.06	-0.91 ± 0.08
E079	07 03 55.4	-11 38 14.07	72	3.2 ± 0.5	1.2 ± 0.3	1.6 ± 0.3	-0.17 ± 0.19	0.08 ± 0.22	0.91 ± 0.11	-0.60 ± 0.15
C047	07 03 55.6	-11 28 02.57	50	-	2.9 ± 0.6	3.8 ± 0.7	-	-	-	-
E044	07 03 55.8	-11 32 45.74	280	20.0 ± 1.5	2.8 ± 0.4	7.6 ± 0.9	-0.12 ± 0.07	-0.66 ± 0.12	0.76 ± 0.06	-0.85 ± 0.05
E017	07 03 55.8	-11 29 30.92	755	22.3 ± 1.3	6.7 ± 0.6	7.7 ± 0.7	-0.07 ± 0.06	-0.56 ± 0.08	0.78 ± 0.04	-0.82 ± 0.04

Table B.1. Continued. Column description: (1) X-ray source identification; (2, 3) J_{2000} coordinates (4) Maximum likelihood; (5,6 and 7) Count Rates detected in each EPIC camera PN, MOS1 and MOS2 individually ; (8, 9, 10 and 11) PN hardness ratios.

ID CMAx ⁽¹⁾	RA (J2000) (2)	DEC (J2000) (3)	ML (4)	PN ⁽⁵⁾	CR (cts/ks) MOS1 ⁽⁶⁾	MOS2 ⁽⁷⁾	HR1 ⁽⁸⁾ 0.5-1.0-2.0 keV	HR2 ⁽⁹⁾ 1.0-2.0-7.3 keV	HR1 ⁽¹⁰⁾ 0.2-0.5-2.0 keV	HR2 ⁽¹¹⁾ 0.5-2.0-4.5 keV
E026	07 03 55.9	-11 33 38.37	573	21.7 ± 1.2	1.4 ± 0.3	4.3 ± 0.9	0.14 ± 0.06	-0.37 ± 0.06	0.98 ± 0.02	-0.66 ± 0.04
E198	07 03 55.9	-11 43 09.50	17	-	-	-	-	-	-	-
E031	07 03 56.0	-11 42 07.93	349	15.0 ± 1.3	-	3.9 ± 0.5	-0.09 ± 0.08	-0.58 ± 0.12	0.86 ± 0.05	-0.81 ± 0.06
E378	07 03 56.4	-11 29 45.68	15	-	-	1.7 ± 0.4	-	-	-	-
E099	07 03 56.8	-11 34 55.63	37	2.3 ± 0.5	-	0.9 ± 0.3	0.53 ± 0.18	-0.86 ± 0.21	1.00 ± 0.03	-0.97 ± 0.10
E089	07 03 56.9	-11 39 10.64	61	3.8 ± 0.6	1.0 ± 0.3	1.0 ± 0.3	-0.37 ± 0.15	-0.21 ± 0.25	0.85 ± 0.11	-0.74 ± 0.11
E003	07 03 57.1	-11 28 29.73	2,190	109.0 ± 3.1	18.2 ± 1.0	6.5 ± 1.1	0.08 ± 0.03	-0.38 ± 0.04	0.63 ± 0.02	-0.69 ± 0.02
E150	07 03 57.6	-11 25 33.31	26	2.7 ± 0.7	-	-	-0.44 ± 0.25	-0.06 ± 0.46	-	-
E042	07 03 57.8	-11 24 18.99	256	13.0 ± 1.3	4.0 ± 0.7	4.9 ± 0.8	-0.09 ± 0.10	-0.99 ± 0.08	0.76 ± 0.07	-0.97 ± 0.04
E103	07 03 58.0	-11 30 03.65	19	2.6 ± 0.6	-	-	-0.19 ± 0.22	-0.57 ± 0.33	0.62 ± 0.17	-0.88 ± 0.13
E091	07 03 58.1	-11 32 40.65	50	2.7 ± 0.5	-	1.6 ± 0.3	0.63 ± 0.24	-0.19 ± 0.20	1.00 ± 0.13	-0.37 ± 0.18
E106	07 03 58.5	-11 34 17.40	29	2.0 ± 0.4	-	-	0.02 ± 0.21	-0.82 ± 0.30	1.00 ± 0.06	-0.96 ± 0.11
E078	07 03 58.8	-11 29 35.22	72	6.0 ± 0.7	-	-	0.14 ± 0.12	-0.79 ± 0.15	0.79 ± 0.10	-0.89 ± 0.08
E016	07 03 58.9	-11 35 30.29	739	15.0 ± 0.9	3.1 ± 0.5	4.9 ± 0.5	0.10 ± 0.06	-0.64 ± 0.07	0.84 ± 0.04	-0.82 ± 0.04
E034	07 04 00.0	-11 30 31.18	295	9.1 ± 0.8	2.8 ± 0.4	2.3 ± 0.4	0.00 ± 0.09	-0.57 ± 0.12	0.83 ± 0.06	-0.83 ± 0.06
E067	07 04 00.5	-11 33 58.51	108	4.7 ± 0.6	-	-	1.9 ± 0.3	-0.25 ± 0.13	0.87 ± 0.11	-0.47 ± 0.11
E359	07 04 00.8	-11 23 20.13	29	-	-	4.5 ± 0.9	-	-	-	-
E085	07 04 00.9	-11 27 11.65	63	3.6 ± 0.6	-	1.4 ± 0.4	-0.15 ± 0.17	-0.89 ± 0.22	0.86 ± 0.14	-0.94 ± 0.09
E058	07 04 01.1	-11 38 25.27	153	6.5 ± 0.7	1.6 ± 0.3	1.9 ± 0.3	-0.17 ± 0.11	-0.46 ± 0.16	0.91 ± 0.06	-0.84 ± 0.07
E032	07 04 01.3	-11 36 23.33	373	15.8 ± 1.7	2.8 ± 0.4	3.7 ± 0.4	-0.14 ± 0.11	-0.50 ± 0.16	0.91 ± 0.06	-0.77 ± 0.08
E055	07 04 01.3	-11 28 43.73	145	10.1 ± 0.9	-	-	-0.04 ± 0.09	-0.60 ± 0.12	0.83 ± 0.06	-0.80 ± 0.07
E053	07 04 01.4	-11 37 00.10	157	6.5 ± 0.7	2.0 ± 0.3	1.7 ± 0.3	0.69 ± 0.16	0.29 ± 0.10	0.94 ± 0.09	-0.03 ± 0.12
E093	07 04 01.6	-11 21 30.60	78	10.9 ± 1.4	-	4.7 ± 0.8	0.64 ± 0.15	0.00 ± 0.13	1.00 ± 0.06	-0.17 ± 0.13
E080	07 04 01.7	-11 26 14.83	44	7.1 ± 1.1	-	2.2 ± 0.5	1.00 ± 0.10	-0.14 ± 0.15	1.00 ± 0.14	-0.28 ± 0.16
E040	07 04 02.2	-11 23 29.31	426	75.2 ± 3.7	-	14.7 ± 1.6	0.45 ± 0.06	-0.02 ± 0.05	1.00 ± 0.01	-0.29 ± 0.05
E068	07 04 02.3	-11 24 17.87	105	9.7 ± 1.2	-	2.9 ± 0.7	-0.14 ± 0.13	-0.54 ± 0.19	1.00 ± 0.04	-0.88 ± 0.08
E036	07 04 02.3	-11 25 37.12	290	16.0 ± 1.3	3.5 ± 0.7	5.0 ± 0.7	0.04 ± 0.09	-0.61 ± 0.11	0.75 ± 0.06	-0.76 ± 0.06
E057	07 04 03.1	-11 32 07.02	120	4.5 ± 0.6	1.3 ± 0.3	2.2 ± 0.3	-0.05 ± 0.13	-0.39 ± 0.17	0.79 ± 0.09	-0.70 ± 0.10
E019	07 04 03.1	-11 33 57.80	692	16.9 ± 1.1	5.2 ± 0.5	5.3 ± 0.5	0.36 ± 0.07	-0.35 ± 0.07	0.93 ± 0.04	-0.57 ± 0.05
E075	07 04 03.2	-11 28 06.24	65	4.8 ± 0.7	1.2 ± 0.3	-	-0.19 ± 0.15	-0.38 ± 0.22	1.00 ± 0.05	-0.70 ± 0.12
E138	07 04 03.5	-11 38 02.15	24	1.7 ± 0.4	-	-	-0.19 ± 0.25	-1.00 ± 0.21	0.47 ± 0.22	-1.00 ± 0.07
E002	07 04 04.1	-11 26 09.14	2,419	67.2 ± 2.4	22.1 ± 1.2	20.0 ± 1.2	0.13 ± 0.04	-0.41 ± 0.04	0.78 ± 0.02	-0.68 ± 0.03
E043	07 04 04.1	-11 23 44.15	102	-	-	-	-	-	-	-
E125	07 04 04.4	-11 24 20.55	15	-	-	-	-	-	-	-
E110	07 04 04.8	-11 22 29.35	54	5.7 ± 1.1	-	-	-0.04 ± 0.19	-0.55 ± 0.32	1.00 ± 0.06	-0.94 ± 0.11
E101	07 04 05.3	-11 23 23.61	20	4.8 ± 1.1	-	-	0.16 ± 0.30	-0.01 ± 0.28	-	-
E060	07 04 05.4	-11 28 54.99	120	8.2 ± 0.8	2.1 ± 0.5	-	-0.07 ± 0.10	-0.49 ± 0.14	0.86 ± 0.06	-0.78 ± 0.07
E102	07 04 06.0	-11 23 54.78	37	3.7 ± 0.9	-	-	1.00 ± 0.25	-0.62 ± 0.22	1.00 ± 0.05	-0.66 ± 0.20
E185	07 04 06.5	-11 42 20.58	19	3.2 ± 0.6	-	-	1.00 ± 0.24	0.36 ± 0.17	1.00 ± 0.38	0.15 ± 0.22
E127	07 04 06.7	-11 44 46.18	38	3.8 ± 0.7	-	1.1 ± 0.3	-0.42 ± 0.17	-1.00 ± 0.20	1.00 ± 0.03	-1.00 ± 0.05
E193	07 04 07.1	-11 39 42.56	17	-	-	1.1 ± 0.3	-	-	-	-
E092	07 04 07.2	-11 27 29.58	59	4.7 ± 0.7	1.4 ± 0.3	1.8 ± 0.4	0.44 ± 0.22	0.30 ± 0.15	0.92 ± 0.14	-0.02 ± 0.16
E140	07 04 07.4	-11 21 35.25	27	4.1 ± 1.1	-	-	-0.55 ± 0.26	-0.04 ± 0.57	-	-
E096	07 04 07.7	-11 46 30.77	49	6.2 ± 0.9	-	1.7 ± 0.4	0.07 ± 0.15	-0.70 ± 0.20	-0.18 ± 0.13	-0.90 ± 0.11
E014	07 04 08.0	-11 23 09.53	898	43.5 ± 2.5	15.5 ± 1.2	16.2 ± 1.3	0.67 ± 0.06	-0.03 ± 0.06	1.00 ± 0.01	-0.24 ± 0.06
E109	07 04 08.1	-11 23 52.35	38	6.6 ± 1.1	-	-	-0.25 ± 0.16	-0.52 ± 0.28	1.00 ± 0.04	-0.88 ± 0.10
E113	07 04 08.9	-11 39 55.03	28	2.1 ± 0.5	-	-	-0.45 ± 0.20	-0.38 ± 0.50	0.64 ± 0.17	-0.70 ± 0.18
E020	07 04 09.6	-11 30 13.23	552	16.8 ± 1.2	8.6 ± 0.8	10.2 ± 0.9	-0.09 ± 0.07	-0.54 ± 0.09	0.66 ± 0.05	-0.83 ± 0.04
E094	07 04 10.4	-11 31 44.47	64	3.0 ± 0.6	0.7 ± 0.2	1.3 ± 0.3	-0.23 ± 0.23	-0.06 ± 0.30	0.44 ± 0.19	-0.61 ± 0.17
E137	07 04 10.8	-11 34 33.07	23	2.1 ± 0.4	-	1.0 ± 0.2	0.98 ± 0.14	0.02 ± 0.19	0.62 ± 0.24	-0.15 ± 0.20
E169	07 04 11.3	-11 39 49.47	15	1.8 ± 0.4	-	-	1.00 ± 0.35	0.63 ± 0.19	0.92 ± 0.64	0.63 ± 0.27
E081	07 04 11.8	-11 25 10.99	69	5.7 ± 0.9	-	1.9 ± 0.5	-0.11 ± 0.17	-0.39 ± 0.24	0.74 ± 0.13	-0.65 ± 0.13
E038	07 04 12.0	-11 21 28.72	314	24.6 ± 1.9	7.1 ± 0.9	5.4 ± 1.1	0.22 ± 0.08	-0.46 ± 0.09	1.00 ± 0.01	-0.65 ± 0.07
E008	07 04 12.4	-11 39 22.26	893	15.7 ± 0.9	5.0 ± 0.5	4.5 ± 0.5	-0.39 ± 0.06	-0.49 ± 0.10	0.71 ± 0.04	-0.84 ± 0.04
E108	07 04 13.7	-11 35 08.71	40	1.8 ± 0.4	0.6 ± 0.2	-	-0.29 ± 0.20	-1.00 ± 0.48	0.93 ± 0.12	-0.84 ± 0.15
E154	07 04 14.3	-11 23 14.36	23	4.7 ± 1.2	-	-	0.19 ± 0.27	-0.25 ± 0.31	1.00 ± 0.07	-0.67 ± 0.22
E129	07 04 14.6	-11 39 53.42	36	3.0 ± 0.5	1.2 ± 0.3	-	-0.11 ± 0.18	-0.47 ± 0.26	0.76 ± 0.13	-0.69 ± 0.13
E050	07 04 14.7	-11 42 17.31	173	9.0 ± 0.9	-	4.1 ± 0.5	0.65 ± 0.11	0.04 ± 0.10	0.96 ± 0.06	-0.26 ± 0.10
E062	07 04 15.2	-11 33 56.12	114	-	1.9 ± 0.3	2.4 ± 0.3	-	-	-	-
E097	07 04 15.4	-11 45 50.44	60	6.9 ± 1.0	-	1.6 ± 0.4	0.84 ± 0.15	0.21 ± 0.13	1.00 ± 0.09	0.04 ± 0.15
E205	07 04 15.4	-11 21 28.41	18	-	-	-	-	-	-	-
E111	07 04 16.0	-11 26 09.78	31	3.8 ± 0.7	-	-	0.04 ± 0.18	-0.54 ± 0.25	0.53 ± 0.16	-0.76 ± 0.14
E028	07 04 16.0	-11 24 01.98	498	24.8 ± 1.8	7.4 ± 0.8	5.1 ± 0.8	-0.34 ± 0.07	-0.78 ± 0.11	0.87 ± 0.04	-0.93 ± 0.04
E087	07 04 16.0	-11 33 33.36	41	2.7 ± 0.5	0.9 ± 0.2	-	-0.44 ± 0.20	-0.10 ± 0.35	0.77 ± 0.14	-0.77 ± 0.15
E149	07 04 16.0	-11 37 00.24	18	2.0 ± 0.4	-	-	0.40 ± 0.33	0.37 ± 0.20	1.00 ± 0.13	-0.06 ± 0.23
E195	07 04 16.3	-11 23 45.03	58	-	1.9 ± 0.5	3.1 ± 0.7	-	-	-	-
E177	07 04 16.5	-11 29 53.64	17	1.9 ± 0.5	-	0.9 ± 0.3	-0.74 ± 0.57	0.94 ± 0.13	-	-
E120	07 04 16.6	-11 27 41.97	42	3.3 ± 0.6	-	-	-0.12 ± 0.18	-0.45 ± 0.32	0.84 ± 0.16	-0.82 ± 0.15
E117	07 04 16.8	-11 43 06.55	24	2.8 ± 0.6	-	-	-0.37 ± 0.19	-0.52 ± 0.45	0.93 ± 0.13	-0.96 ± 0.10
E141	07 04 17.9	-11 28 18.87	31	2.8 ± 0.5	-	-	-0.32 ± 0.18	-0.73 ± 0.32	0.74 ± 0.15	-0.99 ± 0.07
E025	07 04 18.0	-11 34 25.56	494	8.3 ± 0.7	3.2 ± 0.4	3.5 ± 0.4	0.08 ± 0.10	-0.37 ± 0.11	0.88 ± 0.06	-0.63 ± 0.07
E030	07 04 18.3	-11 25 24.83	227	14.3 ± 1.3	3.7 ± 0.6	5.5 ± 0.8	-0.14 ± 0.09	-0.47 ± 0.13	0.71 ± 0.07	-0.79 ± 0.06
E005	07 04 18.5	-11 42 35.81	1,406	37.2 ± 1.6	-	11.0 ± 0.8	-0.08 ± 0.05	-0.40 ± 0.06	0.75 ± 0.03	-0.72 ± 0.03
E012	07 04 19.2	-11 33 46.60	842	71.2 ± 3.1	4.5 ± 0.4	5.0 ± 0.5	0.14 ± 0.05	-0.52 ± 0.05	0.91 ± 0.03	-0.71 ± 0.03
E105	07 04 19.3	-11 37 18.84	29	2.9 ± 0.5	-	-	-0.07 ± 0.19	-0.10 ± 0.22	0.84 ± 0.15	-0.55 ± 0.15
E004	07 04 19.3	-11 25 05.45	1,814	56.9 ± 2.3	23.9 ± 1.6	16.9 ± 1.2	0.10 ± 0.04	-0.42 ± 0.05	0.83 ± 0.03	-0.71 ± 0.03
E128	07 04 19.9	-11 44 07.89	36	2.4 ± 0.6	-	1.9 ± 0.4	0.28 ± 0.25	-0.63 ± 0.32	0.52 ± 0.25	-0.65 ± 0.20
E122	07 04 20.1	-11 32 14.53	23	2.5 ± 0.5	-	-	0.15 ± 0.23	0.01 ± 0.22	1.00 ± 0.04	-0.45 ± 0.18
E071	07 04 20.3	-11 24 29.89	59	7.1 ± 1.0	2.3 ± 0.6	-	-0.15 ± 0.15	-0.30 ± 0.21	0.86 ± 0.11	-0.80 ± 0.11
E147	07 04 20.7	-11 25 49.24	17	2.7 ± 0.6	-	-	-0.15 ± 0.23	-0.90 ± 0.36	1.00 ± 0.07	-1.00 ± 0.18
E033	07 04 20.8	-11 36 43.42	104	-	1.6 ± 0.3	1.6 ± 0.3	-	-	0.70 ± 0.12	-0.83 ± 0.09

Table B.1. Continued. Column description: (1) X-ray source identification; (2, 3) J_{2000} coordinates (4) Maximum likelihood; (5,6 and 7) Count Rates detected in each EPIC camera PN, MOS1 and MOS2 individually ; (8, 9, 10 and 11) PN hardness ratios.

ID	RA (J2000) (2)	DEC (J2000) (3)	ML (4)	PN ⁽⁵⁾	CR (cts/ks) MOS1 ⁽⁶⁾	MOS2 ⁽⁷⁾	HR1 ⁽⁸⁾ 0.5-1.0-2.0 keV	HR2 ⁽⁹⁾ 1.0-2.0-7.3 keV	HR1 ⁽¹⁰⁾ 0.2-0.5-2.0 keV	HR2 ⁽¹¹⁾ 0.5-2.0-4.5 keV
E143	07 04 20.9	-11 29 35.90	20	2.4 ± 0.5	-	-	-0.21 ± 0.23	-0.32 ± 0.37	0.92 ± 0.13	-0.50 ± 0.19
E007	07 04 21.5	-11 37 02.14	1.065	19.7 ± 1.0	6.4 ± 0.5	6.4 ± 0.5	-0.09 ± 0.05	-0.63 ± 0.07	0.80 ± 0.04	-0.86 ± 0.03
E130	07 04 21.6	-11 29 13.14	31	2.5 ± 0.5	1.0 ± 0.3	-	-0.01 ± 0.20	-0.84 ± 0.28	1.00 ± 0.09	-0.95 ± 0.13
E066	07 04 22.1	-11 22 26.73	122	11.4 ± 1.3	2.6 ± 0.6	2.8 ± 0.7	-0.29 ± 0.12	-0.17 ± 0.17	1.00 ± 0.08	-0.75 ± 0.09
E126	07 04 22.1	-11 39 30.62	29	1.9 ± 0.4	-	-	-0.36 ± 0.22	-1.00 ± 0.38	0.73 ± 0.19	-1.00 ± 0.13
E013	07 04 22.6	-11 31 38.20	836	17.7 ± 1.0	4.9 ± 0.7	5.4 ± 0.5	0.07 ± 0.06	-0.54 ± 0.07	0.94 ± 0.03	-0.73 ± 0.04
E049	07 04 22.8	-11 30 47.06	183	7.2 ± 0.7	2.3 ± 0.4	1.9 ± 0.4	-0.10 ± 0.10	-0.78 ± 0.14	0.79 ± 0.07	-0.89 ± 0.06
E063	07 04 23.4	-11 27 16.35	137	6.0 ± 0.8	2.0 ± 0.4	1.9 ± 0.4	-0.31 ± 0.12	-0.72 ± 0.24	0.83 ± 0.09	-0.89 ± 0.08
E047	07 04 23.4	-11 24 14.72	256	16.9 ± 2.2	5.4 ± 0.7	7.3 ± 0.9	-0.07 ± 0.13	-0.44 ± 0.18	1.00 ± 0.03	-0.76 ± 0.10
E024	07 04 23.5	-11 32 49.63	506	12.0 ± 0.8	3.3 ± 0.4	4.2 ± 0.4	-0.05 ± 0.07	-0.49 ± 0.09	0.80 ± 0.05	-0.79 ± 0.05
E027	07 04 24.0	-11 42 05.79	517	16.5 ± 1.1	-	5.3 ± 0.6	-0.15 ± 0.07	-0.82 ± 0.09	0.71 ± 0.05	-0.91 ± 0.04
E059	07 04 24.1	-11 25 00.14	127	12.7 ± 1.3	2.5 ± 0.6	3.9 ± 0.8	0.05 ± 0.10	-0.49 ± 0.13	0.76 ± 0.07	-0.68 ± 0.08
E146	07 04 24.8	-11 25 22.53	18	3.2 ± 0.8	1.9 ± 0.5	-	0.30 ± 0.40	0.43 ± 0.25	1.00 ± 0.19	0.16 ± 0.27
E022	07 04 26.4	-11 31 19.49	579	13.6 ± 0.9	3.8 ± 0.4	4.2 ± 0.7	-0.12 ± 0.07	-0.58 ± 0.09	0.80 ± 0.05	-0.79 ± 0.04
E153	07 04 26.5	-11 32 18.61	17	2.0 ± 0.5	-	-	-0.56 ± 0.28	0.48 ± 0.34	0.69 ± 0.24	-0.50 ± 0.22
E212	07 04 27.8	-11 27 16.73	18	1.8 ± 0.5	1.0 ± 0.3	-	0.23 ± 0.25	0.34 ± 0.27	0.34 ± 0.23	-1.00 ± 0.19
E052	07 04 28.0	-11 46 27.03	176	11.9 ± 1.2	-	3.4 ± 0.6	-0.21 ± 0.10	-0.58 ± 0.16	0.73 ± 0.13	-0.86 ± 0.07
E018	07 04 28.2	-11 34 41.38	597	13.4 ± 0.9	4.5 ± 0.5	3.2 ± 0.4	-0.15 ± 0.07	-0.58 ± 0.09	0.82 ± 0.05	-0.84 ± 0.04
E168	07 04 28.5	-11 38 49.48	19	-	-	-	-	-	-	-
E010	07 04 30.0	-11 47 21.05	934	56.0 ± 2.8	-	11.8 ± 1.1	0.51 ± 0.05	-0.52 ± 0.05	-	-
E116	07 04 30.7	-11 26 10.69	47	13.8 ± 1.9	-	1.4 ± 0.4	-0.33 ± 0.13	-0.40 ± 0.27	0.72 ± 0.13	-0.78 ± 0.12
E148	07 04 30.7	-11 23 10.31	16	4.1 ± 0.9	-	-	0.43 ± 0.28	0.13 ± 0.24	1.00 ± 0.07	-0.02 ± 0.22
E186	07 04 30.9	-11 34 30.87	16	-	-	-	-	-	-	-
E035	07 04 31.1	-11 32 39.87	293	8.9 ± 0.9	2.7 ± 0.4	2.8 ± 0.4	-0.18 ± 0.10	-0.54 ± 0.14	0.85 ± 0.07	-0.93 ± 0.05
E114	07 04 32.0	-11 33 15.14	25	1.6 ± 0.4	-	-	0.02 ± 0.24	-0.87 ± 0.34	0.75 ± 0.19	-0.91 ± 0.14
E098	07 04 33.5	-11 26 27.61	54	-	1.4 ± 0.5	2.3 ± 0.5	-	-	-	-
E164	07 04 33.7	-11 35 29.85	21	1.6 ± 0.4	-	-	-0.27 ± 0.24	-1.00 ± 0.70	0.80 ± 0.19	-1.00 ± 0.06
E064	07 04 34.4	-11 34 47.54	116	10.0 ± 1.5	2.0 ± 0.3	1.7 ± 0.3	0.27 ± 0.16	-0.30 ± 0.17	0.93 ± 0.08	-0.56 ± 0.12
E084	07 04 37.5	-11 29 35.71	66	4.3 ± 0.7	1.1 ± 0.4	1.4 ± 0.4	-0.33 ± 0.15	-0.48 ± 0.33	0.74 ± 0.13	-0.81 ± 0.13
E090	07 04 38.3	-11 26 48.37	80	6.6 ± 0.9	2.7 ± 0.5	2.3 ± 0.6	0.95 ± 0.09	-0.03 ± 0.14	0.98 ± 0.09	-0.21 ± 0.15
E009	07 04 38.5	-11 31 24.72	966	22.0 ± 1.2	4.5 ± 0.6	5.0 ± 0.5	-0.69 ± 0.04	-0.60 ± 0.15	0.44 ± 0.04	-0.94 ± 0.03
E203	07 04 39.3	-11 26 08.43	16	3.1 ± 0.7	-	-	0.11 ± 0.23	-0.62 ± 0.32	1.00 ± 0.07	-1.00 ± 0.22
E112	07 04 39.8	-11 33 56.30	46	-	1.1 ± 0.3	1.1 ± 0.3	-	-	-	-
E088	07 04 40.0	-11 46 14.92	54	6.2 ± 1.0	1.8 ± 0.5	1.8 ± 0.5	-0.31 ± 0.16	-0.83 ± 0.28	-	-
E156	07 04 40.3	-11 36 27.05	15	1.9 ± 0.5	-	-	-0.21 ± 0.23	-1.00 ± 0.68	0.77 ± 0.21	-1.00 ± 0.20
E132	07 04 40.4	-11 30 31.74	23	2.6 ± 0.6	-	-	-0.75 ± 0.19	-0.06 ± 0.68	1.00 ± 0.11	-0.88 ± 0.14
E100	07 04 41.6	-11 35 43.63	39	3.6 ± 0.6	-	1.4 ± 0.3	0.18 ± 0.22	0.11 ± 0.20	0.02 ± 0.14	-0.34 ± 0.15
E069	07 04 42.0	-11 46 27.50	97	9.4 ± 1.4	2.8 ± 0.7	3.3 ± 0.7	-0.39 ± 0.14	-0.59 ± 0.33	1.00 ± 0.08	-0.88 ± 0.17
E165	07 04 42.1	-11 32 56.75	17	3.4 ± 0.6	-	-	0.97 ± 0.11	-0.04 ± 0.18	0.98 ± 0.14	-0.22 ± 0.19
E041	07 04 42.1	-11 37 16.54	242	11.9 ± 1.0	2.5 ± 0.4	2.2 ± 0.4	-0.13 ± 0.09	-0.38 ± 0.12	0.72 ± 0.07	-0.71 ± 0.06
E191	07 04 42.6	-11 44 04.86	19	3.1 ± 0.7	-	-	0.31 ± 0.22	-0.77 ± 0.28	0.88 ± 0.17	-0.77 ± 0.18
E037	07 04 42.7	-11 36 12.15	282	11.7 ± 1.0	3.3 ± 0.5	2.6 ± 0.4	0.16 ± 0.10	-0.25 ± 0.11	0.60 ± 0.08	-0.52 ± 0.08
E135	07 04 45.2	-11 29 50.48	26	3.3 ± 0.7	-	-	-0.14 ± 0.20	-0.77 ± 0.31	0.63 ± 0.18	-0.92 ± 0.13
E082	07 04 45.4	-11 24 39.56	74	6.7 ± 1.3	2.8 ± 0.6	3.9 ± 0.7	0.04 ± 0.19	-0.69 ± 0.28	1.00 ± 0.11	-0.78 ± 0.16
E137	07 04 45.7	-11 37 58.45	27	2.0 ± 0.5	-	-	-0.64 ± 0.21	-1.00 ± 0.57	0.51 ± 0.19	-1.00 ± 0.10
E145	07 04 49.7	-11 31 15.77	28	3.7 ± 0.7	-	-	0.84 ± 0.28	0.34 ± 0.18	0.35 ± 0.29	0.11 ± 0.22
E184	07 04 52.0	-11 24 54.07	16	-	-	-	-	-	-	-
E006	07 04 52.6	-11 38 47.61	1.159	33.1 ± 1.7	7.0 ± 0.8	8.8 ± 0.8	-0.60 ± 0.04	-0.79 ± 0.11	0.73 ± 0.04	-0.95 ± 0.02
E163	07 04 53.8	-11 36 53.67	20	3.2 ± 0.7	-	-	0.15 ± 0.25	0.05 ± 0.25	1.00 ± 0.06	-0.40 ± 0.21
E070	07 04 54.2	-11 38 36.29	57	7.4 ± 1.0	2.0 ± 0.6	1.7 ± 0.4	-0.10 ± 0.14	-0.61 ± 0.20	0.68 ± 0.11	-0.79 ± 0.10
E029	07 04 56.0	-11 34 15.91	424	18.9 ± 3.7	10.2 ± 0.9	8.0 ± 0.8	-0.14 ± 0.19	-0.56 ± 0.34	0.97 ± 0.13	-0.85 ± 0.15
E021	07 04 56.5	-11 29 31.29	586	22.2 ± 1.6	9.0 ± 0.9	6.8 ± 0.8	-0.24 ± 0.07	-0.49 ± 0.11	0.86 ± 0.04	-0.77 ± 0.05
E124	07 04 59.2	-11 27 54.82	34	6.5 ± 1.3	-	1.5 ± 0.5	0.06 ± 0.20	-0.43 ± 0.27	0.79 ± 0.14	-0.74 ± 0.15
E045	07 05 00.5	-11 37 40.99	225	13.6 ± 1.3	5.1 ± 0.8	3.3 ± 0.6	0.09 ± 0.10	-0.64 ± 0.12	0.18 ± 0.08	-0.80 ± 0.07
E152	07 05 01.1	-11 36 09.33	23	5.3 ± 0.9	-	-	0.18 ± 0.19	-0.21 ± 0.22	0.07 ± 0.15	-0.53 ± 0.16
E144	07 05 01.1	-11 41 25.68	24	2.9 ± 0.7	-	-	-0.92 ± 0.17	-1.00 ± 0.42	0.66 ± 0.22	-0.94 ± 0.12
E139	07 05 01.4	-11 31 16.08	30	4.3 ± 0.9	-	2.6 ± 0.6	1.00 ± 0.29	0.01 ± 0.21	1.00 ± 0.11	-0.32 ± 0.24
E123	07 05 01.9	-11 38 26.18	26	4.1 ± 0.8	-	-	-0.15 ± 0.20	-1.00 ± 0.16	0.91 ± 0.15	-1.00 ± 0.05
E181	07 05 04.2	-11 22 48.02	20	4.8 ± 1.3	-	-	-0.54 ± 0.25	-0.51 ± 0.64	-	-
E001	07 05 04.7	-11 43 06.08	5.257	217.6 ± 5.2	23.6 ± 3.6	-	0.19 ± 0.03	-0.25 ± 0.03	0.83 ± 0.02	-0.59 ± 0.02
E183	07 05 07.2	-11 30 23.12	22	7.6 ± 1.3	2.4 ± 0.7	-	0.73 ± 0.21	0.03 ± 0.17	0.70 ± 0.21	-0.34 ± 0.18
E151	07 05 07.6	-11 41 57.55	18	6.1 ± 1.2	-	-	0.22 ± 0.21	-0.14 ± 0.24	0.90 ± 0.15	-0.51 ± 0.18
E214	07 05 09.2	-11 34 47.06	15	4.7 ± 1.0	-	-	-0.41 ± 0.29	0.57 ± 0.23	0.06 ± 0.24	-0.20 ± 0.23
E048	07 05 09.7	-11 28 23.79	252	36.2 ± 2.4	-	-	0.76 ± 0.07	0.21 ± 0.07	0.86 ± 0.08	-0.03 ± 0.07
E054	07 05 10.1	-11 29 39.63	199	16.7 ± 1.7	10.8 ± 1.7	-	-0.07 ± 0.10	-0.58 ± 0.15	0.76 ± 0.07	-0.85 ± 0.07
E155	07 05 11.1	-11 38 50.52	23	4.1 ± 0.9	-	-	0.03 ± 0.22	-1.00 ± 0.27	0.73 ± 0.17	-1.00 ± 0.09
E194	07 05 11.6	-11 34 33.41	17	4.5 ± 1.0	-	-	0.02 ± 0.23	-0.38 ± 0.33	1.00 ± 0.12	-0.80 ± 0.18
E121	07 05 12.3	-11 32 41.55	56	7.6 ± 1.3	2.7 ± 0.8	2.7 ± 0.8	-0.09 ± 0.17	-0.49 ± 0.27	0.88 ± 0.14	-0.81 ± 0.13
E202	07 05 12.3	-11 35 25.37	21	-	-	-	-	-	-	-
E167	07 05 12.3	-11 36 41.79	17	2.2 ± 0.7	-	-	-1.00 ± 0.24	1.00 ± 14.52	-	-
E134	07 05 15.2	-11 30 55.66	31	5.1 ± 1.1	-	-	-0.05 ± 0.20	-1.00 ± 0.35	1.00 ± 0.15	-1.00 ± 0.20
E073	07 05 16.0	-11 32 04.62	97	13.2 ± 1.6	-	-	-0.12 ± 0.12	-0.47 ± 0.19	0.91 ± 0.08	-0.78 ± 0.09

Table B.2. Infrared 2MASS photometry, mass, age and infrared classification of members of CMA R1 region and counterparts to X-ray sources. A distance of 1 kpc is assumed for them. Column description: (1) X-ray source identification (Table B.1); (2) Distance from X-ray source center; (3) 2MASS identification (4, 5 and 6) J, H and K magnitudes; (7) 2MASS Quality flag; (8) Mass; (9) Age; (10) *WISE* classification. Note:(*) Counterpart candidate not considered, due to distance incompatible with the cloud (see Sect. 4.1).

ID ⁽¹⁾	D	ID ⁽³⁾	J ⁽⁴⁾	σ_J	H ⁽⁵⁾	σ_H	K ⁽⁶⁾	σ_K	Qflag ⁽⁷⁾	Mass ⁽⁸⁾	Age ⁽⁹⁾	WISE ⁽¹⁰⁾
CMaX	(")	2MASS	mag	mag	mag	mag	mag	mag		M _⊙	Myr	
W066	–	–	–	–	–	–	–	–	–	–	–	–
W017*	9	07003741-1123529	13.554	0.024	13.231	0.026	13.211	0.035	AAA	–	–	–
W001	2	07003760-1114451	6.575	0.023	6.032	0.049	5.905	0.023	AAA	??	??	Class III
W040	–	–	–	–	–	–	–	–	–	–	–	–
W002	3	07004336-1117153	12.883	0.026	12.312	0.024	12.24	0.024	AAA	1.45	12	??
W048	2	07004705-1122044	15.438	0.048	14.799	0.083	14.385	0.079	AAA	0.28	4.5	Class III
W042	4	07004851-1112380	13.901	0.03	13.225	0.037	13.114	0.041	AAA	1.18	14	Class III
W078	3	07005585-1126246	13.542	0.024	12.826	0.034	12.58	0.026	AAA	0.7	1.8	Class III
W018	–	–	–	–	–	–	–	–	–	–	–	–
W061	1	07005640-1117579	13.399	0.024	12.922	0.026	12.798	0.027	AAA	1.15	22	??
W023	2	07010058-1118374	14.131	0.024	13.5	0.028	13.277	0.04	AAA	1.1	10	??
W009	1	07010086-1119307	12.8	0.026	12.083	0.032	11.846	0.024	AAA	0.72	0.9	??
W041	–	–	–	–	–	–	–	–	–	–	–	–
W070	2	07010686-1131229	9.436	0.022	8.955	0.025	8.813	0.019	AAA	4.2	0.9	Class III
W037	9	07011019-1109056	16.687	0.158	16.267	–	15.291	–	CUU	–	–	–
W031	2	07011115-1127501	10.857	0.03	10.604	0.035	10.539	0.027	AEA	–	–	–
W022	–	–	–	–	–	–	–	–	–	–	–	–
W044	4	07011245-1110002	14.208	0.027	13.45	0.029	13.181	0.038	AAA	0.37	1.9	??
W143	0.9	07011222-1126597	11.535	0.026	11.429	0.027	11.393	0.026	AAA	2.35	5.5	Class III
W112a	2	07011260-1128337	9.421	0.026	9.199	0.022	9.155	0.021	AAA	3.9	1.2	Class III
W112b	8	07011291-1128304	12.136	–	14.868	0.355	11.731	–	UDU	–	–	–
W065	4	07011271-1125514	13.396	0.027	12.816	0.029	12.576	0.033	AAA	1.35	6	Class III
W055	1	07011369-1121159	15	0.04	14.312	0.041	14.129	0.065	AAA	0.85	27.5	Class III
W052a	2	07011404-1108578	13.51	0.032	13.079	0.038	12.824	0.029	AAA	1.25	17.5	??
W052b	8	07011425-1109053	12.226	0.024	11.905	0.023	11.865	0.025	AAA	1.6	12	??
W147	–	–	–	–	–	–	–	–	–	–	–	–
W072	–	–	–	–	–	–	–	–	–	–	–	–
W025a	2	07011454-1120333	10.296	0.026	10.139	0.025	10.069	0.024	AAA	3.55	1.9	??
W025b	8	07011510-1120281	16.547	0.172	15.552	–	15.308	–	CUU	–	–	–
W008	2	07011643-1125525	13.654	0.029	13.028	0.027	12.928	0.034	AAA	1.25	13	Class III
W053	1	07011660-1109075	14.919	0.038	14.291	0.036	14.15	0.072	AAA	0.85	48	Class III
W149	3	07011692-1117569	16.446	0.114	15.845	0.196	15.063	–	BCU	–	–	–
W012	4	07011698-1123514	14.872	0.043	14.238	0.063	13.918	0.069	AAA	0.8	12.5	??
W086	–	–	–	–	–	–	–	–	–	–	–	–
W029	1	07011816-1119524	11.762	0.022	11.487	0.022	11.46	0.023	AAA	2.05	8	??
W049	3	07011889-1119241	11.702	0.024	11.483	0.025	11.419	0.026	AAA	2.1	8	Class III
W019*	0.9	07011995-1117301	15.807	0.068	15.239	0.096	15.371	0.185	AAC	–	–	–
W064	–	–	–	–	–	–	–	–	–	–	–	–
W077	–	–	–	–	–	–	–	–	–	–	–	–
W013	3	07012127-1105589	16.89	0.161	16.102	0.206	15.417	0.214	CCC	–	–	–
W035	–	–	–	–	–	–	–	–	–	–	–	–
W034	1	07012418-1124287	13.869	0.026	13.397	0.027	13.266	0.039	AAA	1.05	40	??
W051*	4	07012440-1109043	14.779	0.038	14.225	0.048	14.115	0.062	AAA	–	–	–
W085	–	–	–	–	–	–	–	–	–	–	–	–
W057	–	–	–	–	–	–	–	–	–	–	–	–
W014*	0.5	07012640-1117565	15.989	0.073	15.429	0.113	15.186	0.157	ABC	–	–	–
W004	1	07012678-1128220	12.341	0.023	12	0.022	11.876	0.021	AAA	1.55	13	Class III
W006a	8	07012872-1121240	16.224	0.091	15.78	0.156	15.13	0.168	ACC	–	–	–
W006b	10	07012942-1121383	16.535	0.124	15.863	0.167	15.014	–	BCU	–	–	–
W080a	5	07013059-1113327	16.64	0.153	16.07	0.215	15.252	–	BCU	–	–	–
W080b	9	07013066-1113254	16.755	0.142	16.576	–	15.468	–	BUU	–	–	–
W007	–	–	–	–	–	–	–	–	–	–	–	–
W054a	2	07013393-1123176	10.802	0.022	10.623	0.023	10.528	0.019	AAA	2.9	3.7	Class III
W054b	9	07013352-1123148	15.237	0.091	14.645	0.177	14.374	0.091	ACA	–	–	–
W026a	1	07013401-1125326	13.805	0.027	13.217	0.029	13.124	0.031	AAA	1.13	23	Class III
W026b	8	07013361-1125362	16.371	0.104	15.901	0.182	15.397	0.206	ACC	–	–	–
W011a	2	07013441-1117375	13.512	0.032	12.905	0.044	12.779	0.03	AAA	1.35	12	??
W011b	5	07013419-1117417	15.6	0.06	14.798	0.087	14.433	0.135	AAB	–	–	–
W050	10	07013489-1115453	15.397	0.054	14.732	0.061	14.544	0.079	AAA	0.75	60	–
W033	3	07013612-1123088	14.289	0.027	13.683	0.027	13.541	0.038	AAA	1	25	Class III
W096	1	07013774-1112371	15.133	0.045	14.415	0.063	14.222	0.072	AAA	0.83	24	–
W076	0.9	07013843-1110147	15.207	0.042	14.476	0.044	14.325	0.077	AAA	0.78	27	??
W043	–	–	–	–	–	–	–	–	–	–	–	–
W015	–	–	–	–	–	–	–	–	–	–	–	–
W021	2	07014236-1123337	14.552	0.039	13.965	0.028	13.696	0.053	AAA	0.98	20.5	??
W024	3	07014590-1130331	13.354	0.024	12.668	0.022	12.469	0.023	AAA	1.05	3	??
W038	2	07014669-1118126	14.794	0.038	13.988	0.034	13.724	0.054	AAA	0.28	2.2	–
W060	4	07014897-1113201	11.399	0.024	10.994	0.023	10.909	0.021	AAA	1.95	6	Class III
W047a	5	07015002-1118275	12.6	0.022	12.203	0.021	12.126	0.024	AAA	1.42	16	–
W047b	7	07015058-1118196	16.076	0.104	15.484	0.124	15.147	0.167	ABC	–	–	–
W005	0.9	07015058-1116405	13.692	0.022	13.149	0.03	12.929	0.033	AAA	1.25	17	–
W003	2	07015243-1120184	12.056	0.022	11.669	0.021	11.457	0.023	AAA	1.75	7.5	Class II/III
W016	0.9	07015256-1119089	12.313	0.022	11.976	0.022	11.926	0.021	AAA	1.55	12.5	Class III
C054	3	07015417-1129128	15.569	0.063	15.086	0.11	14.7	0.097	ABA	–	–	–
W010a	3	07015414-1118094	12.943	0.021	12.336	0.021	12.069	0.021	AAA	1.1	1.9	Class III
W010b	9	07015341-1118042	16.304	0.12	15.609	0.151	15.121	0.167	BBC	–	–	–

Table B.2. Continued. Column description: (1) X-ray source identification (Table B.1); (2) Distance from X-ray source center; (3) 2MASS identification (4, 5 and 6) J, H and K magnitudes; (7) 2MASS Quality flag; (8) Mass; (9) Age; (10) WISE classification. Note: (*) Counterpart candidate not considered, due to distance incompatible with the cloud (see Sect. 4.1).

ID ⁽¹⁾ CMaX	D (^o)	ID ⁽³⁾ 2MASS	J ⁽⁴⁾ mag	σ_J mag	H ⁽⁵⁾ mag	σ_H mag	K ⁽⁶⁾ mag	σ_K mag	Qflg ⁽⁷⁾	Mass ⁽⁸⁾ M _⊙	Age ⁽⁹⁾ Myr	WISE ⁽¹⁰⁾
W056	–	–	–	–	–	–	–	–	–	–	–	–
W045	0.4	07015445-1122194	12.896	0.024	12.595	0.024	12.511	0.029	AAA	1.45	26	Class III
W058	2	07015673-1122462	14.533	0.035	13.819	0.026	13.615	0.044	AAA	0.92	10.5	Class II/III
W036	0.5	07015688-1124083	14.228	0.029	13.552	0.035	13.341	0.034	AAA	1.04	8	??
W027	3	07015745-1107011	10.368	0.023	10.116	0.022	10.078	0.023	AAA	3.4	2.5	Class III
W039	2	07015843-1115469	12.287	0.03	11.646	0.032	11.528	0.029	AAA	1.9	3	Class III
S012	–	–	–	–	–	–	–	–	–	–	–	–
W028	4	07015981-1127407	16.213	0.107	15.887	–	15.089	–	AUU	–	–	–
S015	–	–	–	–	–	–	–	–	–	–	–	–
S008	0.9	07020190-1145394	13.246	0.026	12.768	0.026	12.682	0.026	AAA	1.22	21	??
S030	9	07020363-1140372	14.407	0.035	13.539	0.03	13.191	0.035	AAA	0.18	0.3	??
W059	–	–	–	–	–	–	–	–	–	–	–	–
S119	5	07020757-1136088	14.877	0.044	14.272	0.059	14.005	0.062	AAA	0.88	23	??
S027	–	–	–	–	–	–	–	–	–	–	–	–
S020	2	07021035-1141399	14.582	0.049	13.948	0.046	13.831	0.051	AAA	0.95	40	–
S013	8	07021205-1148405	14.575	0.035	13.883	0.044	13.712	0.043	AAA	0.98	18	??
C078	3	07021265-1122366	14.838	0.044	13.94	0.038	13.727	0.059	AAA	0.24	2.5	??
W046	3	07021274-1124394	13.822	0.028	13.189	0.028	13.087	0.037	AAA	1.15	18	??
S006	1	07021278-1146494	11.752	0.024	11.54	0.024	11.474	0.027	AAA	2.1	8	??
S032	4	07021295-1142395	12.661	0.024	12.139	0.024	12	0.024	AAA	1.7	9	Class III
W032*	6	07021392-1121054	16.079	0.099	15.782	0.173	15.277	0.175	ACC	–	–	–
S044	3	07021498-1156417	13.234	0.026	12.832	0.026	12.662	0.029	AAA	1.23	21	Class III
S010	2	07021606-1133560	12.204	0.032	11.388	0.028	11.08	0.023	AAA	??	??	??
S016	2	07021645-1150558	16.343	0.109	15.525	0.131	15.231	0.168	ABC	–	–	–
W063	3	07021951-1113448	13.793	0.029	13.076	0.024	12.935	0.034	AAA	1.15	6	Class III
S022	–	–	–	–	–	–	–	–	–	–	–	–
S033*	3	07022033-1148007	15.836	0.071	15.037	0.1	15.012	0.144	AAB	–	–	–
S041	1	07022058-1142102	13.798	0.027	13.193	0.026	13.074	0.035	AAA	1.15	17.5	??
C100	6	07022222-1115184	13.823	0.036	13.274	0.044	13.084	0.044	AAA	1.15	17	??
C066a	5	07022196-1126438	16.19	0.105	15.255	0.104	14.332	–	AAU	–	–	–
C066b	2	07022200-1126404	14.914	0.058	14.221	0.067	13.906	–	AAU	–	–	–
W030	3	07022212-1121238	15.086	0.049	14.259	0.064	14.061	0.064	AAA	0.38	4.5	Class III
S025	3	07022282-1139064	14.232	0.029	13.636	0.028	13.424	0.043	AAA	1.05	17.5	??
S019	2	07022324-1143091	14.316	0.026	13.626	0.035	13.429	0.038	AAA	1.02	9	??
W020	4	07022384-1124588	15.081	0.039	14.088	0.043	13.899	0.055	AAA	0.18	2.1	??
W068*	9	07022560-1116095	16.037	0.075	15.206	0.113	15.219	0.172	ABC	–	–	–
S005	6	07022600-1155067	13.204	0.024	12.349	0.022	12.13	0.024	AAA	0.14	0.28	Class III
C136	–	–	–	–	–	–	–	–	–	–	–	–
S114	–	–	–	–	–	–	–	–	–	–	–	–
C080	5	07022735-1134552	10.04	0.024	9.761	0.022	9.695	0.023	AAA	3.6	1.9	Class III
C056	5	07022785-1130569	14.391	0.022	13.727	0.026	13.515	0.039	AAA	1.04	14	??
C090	–	–	–	–	–	–	–	–	–	–	–	–
C011	2	07023052-1122244	9.874	0.023	9.67	0.024	9.624	0.019	AAA	3.7	1.7	Class III
C062	2	07023071-1119055	15.919	0.076	15.04	0.073	14.67	0.108	AAA	??	??	??
S039	8	07023368-1147492	16.787	0.17	15.805	0.18	15.346	0.195	CCC	–	–	–
S021	–	–	–	–	–	–	–	–	–	–	–	–
S029	2	07023378-1157206	12.31	0.023	11.357	0.022	11.061	0.023	AAA	??	??	Class III
C012	2	07023628-1125008	13.38	0.028	12.562	0.028	12.376	0.03	AAA	0.55	0.9	–
C064	–	–	–	–	–	–	–	–	–	–	–	–
C019	2	07023666-1128115	14.087	0.026	13.367	0.035	13.106	0.035	AAA	0.65	3	Class III
C041	3	07024001-1128240	14.567	0.05	13.727	0.042	13.423	0.055	AAA	0.21	2.05	–
C048	–	–	–	–	–	–	–	–	–	–	–	–
C042a	6	07024193-1128079	14.737	0.072	13.799	0.067	13.56	0.084	AAA	0.18	2	Class III
C042b	8	07024222-1128112	15.289	0.083	14.363	0.088	13.667	0.06	AAA	??	??	Class II
C042c	5	07024255-1128015	13.149	0.024	12.619	0.025	12.443	0.023	AAA	1.42	9.5	Class III
C042d	7	07024247-1128095	16.231	0.122	15.461	0.146	15.102	0.151	BBB	–	–	–
C042e	4	07024206-1128004	16.007	0.087	15.298	0.106	14.842	0.129	AAB	–	–	–
C009	3	07024261-1127117	7.825	0.021	7.773	0.036	7.73	0.018	AAA	7.5	0.3	Class III
C035	3	07024314-1125544	14.063	0.026	13.245	0.022	13.025	0.026	AAA	0.29	1.5	–
C026a	4	07024393-1123475	13.488	0.029	12.781	0.031	12.524	0.032	AAA	0.68	1.7	??
C026b	10	07024312-1123532	14.607	0.033	13.669	0.027	13.355	0.042	AAA	0.15	0.21	–
C001a	1	07024398-1127282	10.291	0.023	10.027	0.022	9.952	0.023	AAA	3.6	2.1	Class III
C001b	9	07024369-1127360	14.133	0.037	13.216	0.035	12.954	0.037	AAA	0.21	0.5	–
C001c	10	07024458-1127264	15.788	0.084	14.963	0.112	14.665	0.105	ABA	–	–	–
S018	2	07024439-1141088	11.022	0.026	10.519	0.022	10.466	0.024	AAA	2.75	3	Class III
C124	4	07024462-1120270	13.507	0.026	12.884	0.022	12.63	0.019	AAA	1.06	4	??
C013	2	07024498-1135140	13.05	–	12.743	0.056	12.481	0.043	UEA	–	–	–
C015	2	07024607-1128059	13.531	0.029	12.758	0.031	12.534	0.033	AAA	0.55	1.1	–
C023a	2	07024616-1126566	15.296	0.04	14.565	0.053	14.389	0.072	AAA	0.77	30	–
C023b	4	07024651-1126582	14.424	0.036	13.586	0.041	13.309	0.044	AAA	0.24	0.18	Class III
C023c	9	07024651-1127040	16.371	0.103	15.501	0.15	15.191	0.166	ABC	–	–	–
C033	1	07024652-1132594	13.63	0.029	12.797	0.022	12.524	0.024	AAA	0.25	0.24	??
C020a	2	07024757-1125096	14.025	0.036	13.168	0.039	12.809	0.044	AAA	0.18	0.18	??
C020b	6	07024766-1125136	15.753	0.069	14.863	0.077	14.442	0.092	AA	??	??	–
C058a	2	07024768-1137263	11.331	0.023	10.761	0.022	10.656	0.024	AAA	2.6	2.5	Class III
C058b	6	07024724-1137219	15.893	0.129	14.912	0.118	14.616	0.107	BBA	–	–	–
C075	5	07024771-1123033	13.139	0.024	12.75	0.025	12.613	0.027	AA	1.28	21	??
C021a	2	07024815-1118175	14.691	0.033	14.037	0.049	13.768	0.048	AAA	0.88	12	–
C021b	4	07024832-1118203	13.82	0.045	13.246	0.06	13.186	0.051	AAA	1.08	30	??

Table B.2. Continued. Column description: (1) X-ray source identification (Table B.1); (2) Distance from X-ray source center; (3) 2MASS identification (4, 5 and 6) J, H and K magnitudes; (7) 2MASS Quality flag; (8) Mass; (9) Age; (10) WISE classification. Note: (*) Counterpart candidate not considered, due to distance incompatible with the cloud (see Sect. 4.1).

ID ⁽¹⁾ CMaX	D (^o)	ID ⁽³⁾ 2MASS	J ⁽⁴⁾ mag	σ_J mag	H ⁽⁵⁾ mag	σ_H mag	K ⁽⁶⁾ mag	σ_K mag	Qflg ⁽⁷⁾	Mass ⁽⁸⁾ M _⊙	Age ⁽⁹⁾ Myr	WISE ⁽¹⁰⁾
C017	3	07024842-1124244	14.15	0.028	13.19	0.029	12.853	0.029	AAA	??	??	Class III
C050	0.9	07024876-1117503	15.686	0.059	14.843	0.095	14.686	0.119	AAB	–	–	–
C027	3	07024912-1130388	13.317	0.024	12.55	0.023	12.319	0.023	AAA	0.55	0.9	??
C030	2	07024945-1125470	13.667	0.022	12.754	0.022	12.513	0.027	AAA	0.23	0.19	Class III
C117	6	07024975-1119428	12.983	0.023	12.691	0.027	12.6	0.024	AAA	1.35	55	Class III
C003	2	07025016-1124341	13.043	0.024	12.13	0.029	11.806	0.023	AAA	??	??	Class III
S011	3	07025018-1153449	8.04	0.021	7.761	0.063	7.66	0.02	AAA	6.2	0.4	Class III
S002a	3	07025102-1145561	9.491	0.023	9.389	0.022	9.339	0.024	AAA	4.5	0.9	Class III
S002b	10	07025047-1145520	14.263	0.158	13.635	0.11	13.546	0.106	CBA	–	–	–
C102	–	–	–	–	–	–	–	–	–	–	–	–
S014	1	07025225-1153408	16.564	0.14	15.443	0.129	15.344	0.192	BBC	–	–	–
C022	2	07025284-1127048	13.461	0.023	12.75	0.023	12.538	0.024	AAA	0.85	1.9	Class III
C052	3	07025308-1130093	14.971	0.033	13.989	0.045	13.709	0.047	AAA	0.12	0.24	??
S007a	2	07025292-1154180	13.386	0.03	12.795	0.031	12.65	0.027	AAA	1.35	11	??
S007b	6	07025345-1154179	13.958	0.028	13.136	0.025	12.87	0.032	AAA	0.27	1.1	Class III
C039	3	07025318-1130539	14.168	0.035	13.22	0.047	12.869	0.043	AAA	??	??	Class II/III
C044	2	07025410-1125160	14.854	0.04	13.909	0.045	13.529	0.037	AAA	??	??	Class II/III
C004a	3	07025603-1128310	12.967	0.026	11.953	0.025	11.641	0.029	AAA	??	??	–
C004b	8	07025646-1128272	15.066	0.061	13.795	0.062	13.145	0.051	AAA	??	??	Class II/III
C028	2	07025642-1122189	13.92	0.029	13.241	0.027	13.042	0.037	AAA	1.05	7	??
C061	9	07025621-1121553	13.754	0.024	13.166	0.027	12.934	0.038	AAA	1.25	9	Class III
C119	0.9	07025731-1120353	14.522	0.03	13.936	0.047	13.622	0.045	AAA	0.96	11	??
S001	0.6	07025788-1146232	10.455	0.023	10.214	0.022	10.16	0.019	AAA	3.25	2.2	Class III
S017	8	07025730-1154275	16.903	0.174	15.95	0.158	15.678	–	CCU	–	–	–
C037	2	07025833-1128428	12.831	0.023	11.577	0.023	10.845	0.023	AAA	??	??	Class II
S028	4	07025893-1143345	15.399	0.052	14.757	0.063	14.454	0.092	AAA	0.72	25.5	??
C034	3	07025893-1130048	14.354	0.036	13.323	0.035	12.969	0.039	AAA	??	??	Class III
C008a	2	07025905-1127257	9.97	0.023	9.761	0.023	9.652	0.023	AAA	3.7	1.8	Class III
C008b	9	07025927-1127313	14.492	0.102	13.609	0.091	13.364	0.069	AAA	0.22	1.9	–
C065a	6	07025949-1131513	15.836	0.067	15.158	0.081	14.803	0.106	AAB	–	–	–
C065b	9	07025893-1131550	16.168	0.093	15.354	0.105	15.094	0.142	ABB	–	–	–
C126	–	–	–	–	–	–	–	–	–	–	–	–
C006	2	07030077-1126239	15.28	0.045	14.364	0.045	14.154	0.065	AAA	0.21	3.5	Class III
C082	4	07030093-1122482	15.365	0.047	14.577	0.055	14.215	0.08	AAA	0.18	3	??
S023	1	07030208-1143539	11.607	0.022	11.253	0.023	11.199	0.021	AAA	1.85	8	Class III
C091	8	07030287-1128116	16.257	0.093	15.048	0.077	14.822	0.108	AAB	–	–	–
C002	3	07030298-1126263	13.754	0.026	12.884	0.025	12.678	0.024	AAA	0.28	0.9	??
C024	2	07030304-1125516	14.031	0.033	13.346	0.029	13.237	0.037	AAA	1.15	15	??
C063	3	07030360-1124488	15.003	0.037	13.894	0.035	13.517	0.049	AAA	??	??	Class III
C045	5	07030365-1119195	15.211	0.046	14.515	0.075	14.272	0.079	AAA	0.78	22	Class III
C040	–	–	–	–	–	–	–	–	–	–	–	–
S031a	1	07030678-1157501	13.83	0.041	13.346	0.05	13.283	0.059	AAA	1.05	55	Class III
S031b	4	07030678-1157542	15.777	0.082	14.902	0.084	14.674	0.126	AAB	–	–	–
S004	5	07030751-1139396	15.04	0.039	14.157	0.039	14.059	0.055	AAA	0.65	9	??
S003a	4	07030793-1153073	13.002	0.03	12.424	0.036	12.154	0.03	AAA	1.3	3	??
S003b	2	07030811-1153043	11.859	0.039	11.261	0.045	11.043	0.038	AEA	–	–	–
C060*	8	07030932-1125533	16.365	0.108	15.839	0.181	15.442	0.192	ACC	–	–	–
C036	4	07030989-1116147	13.605	0.024	13.005	0.023	12.877	0.027	AAA	1.25	13	??
C073	–	–	–	–	–	–	–	–	–	–	–	–
C025	2	07031139-1135127	12.444	0.024	11.953	0.025	11.768	0.024	AAA	1.75	6.5	Class III
C031	4	07031181-1130169	14.009	0.029	13.203	0.025	12.906	0.024	AAA	0.25	1.1	??
C074	–	–	–	–	–	–	–	–	–	–	–	–
C029	0.5	07031269-1128382	13.13	0.024	12.249	0.027	11.932	0.024	AAA	??	??	Class II
C097	4	07031553-1128219	14.154	0.033	13.371	0.039	13.125	0.038	AAA	0.35	1.8	–
S024	–	–	–	–	–	–	–	–	–	–	–	–
C107	–	–	–	–	–	–	–	–	–	–	–	–
C072	5	07031994-1128055	14.802	0.043	13.822	0.044	13.51	0.044	AAA	0.12	0.19	Class III
C086	–	–	–	–	–	–	–	–	–	–	–	–
C114*	–	07032314-1129047	15.423	0.051	14.701	0.079	14.654	0.112	AAB	–	–	–
C067	3	07032616-1135024	15.065	0.041	14.334	0.036	14.06	0.058	AAA	0.55	6	??
C059	2	07032626-1123349	14.579	0.033	13.566	0.027	13.1	0.037	AAA	??	??	??
C053a	2	07032742-1132531	14.337	0.029	13.316	0.027	12.916	0.03	AAA	??	??	Class III
C053b	8	07032767-1132446	16.357	0.098	15.324	0.131	14.962	0.133	ABB	–	–	–
E175	2	07033033-1132028	14.125	0.026	13.2	0.036	12.895	0.029	AAA	0.18	0.19	??
S009a	4	07033139-1148153	13.351	0.029	12.769	0.036	12.663	0.034	AAA	1.3	14	Class III
S009b	6	07033168-1148067	15.222	0.043	14.475	0.1	14.291	0.073	AAA	0.81	20	–
S009c	4	07033172-1148114	15.109	0.051	14.428	0.072	14.199	0.076	AAA	0.78	24	–
C046	1	07033281-1132122	11.116	0.023	10.689	0.025	10.554	0.019	AA	2.6	4	??
C032	1	07033309-1117510	13.473	0.024	12.758	0.022	12.483	0.024	AAA	0.57	1.1	Class III
E051	2	07033347-1134269	13.461	0.023	12.765	0.029	12.543	0.024	AAA	0.85	2	??
E118	1	07033446-1135042	14.238	0.032	13.369	0.036	12.948	0.037	AA	0.15	0.1	–
C071	3	07033469-1127533	11.617	0.023	11.423	0.022	11.338	0.019	AAA	2.1	7.5	Class III
C005a	9	07033492-1126217	14.631	0.038	13.992	0.057	13.753	0.044	AAA	0.95	16	??
C005b	4	07033559-1126229	12.539	0.022	11.862	0.023	11.66	0.026	AAA	1.05	1	??
C018	–	–	–	–	–	–	–	–	–	–	–	–
C007	3	07033726-1131146	13.651	0.029	12.873	0.024	12.619	0.029	AAA	0.32	1.1	–
E076a	3	07033845-1142477	14.807	0.04	13.977	0.034	13.762	0.058	AA	0.28	0.3	Class III
E076b	7	07033905-1142510	16.515	0.125	15.747	0.174	15.244	0.172	BCC	–	–	–
E095a	3	07033905-1137183	14.686	0.04	13.917	0.046	13.677	0.051	AAA	4.5	0.52	–

Table B.2. Continued. Column description: (1) X-ray source identification (Table B.1); (2) Distance from X-ray source center; (3) 2MASS identification (4, 5 and 6) J, H and K magnitudes; (7) 2MASS Quality flag; (8) Mass; (9) Age; (10) WISE classification. Note: (*) Counterpart candidate not considered, due to distance incompatible with the cloud (see Sect. 4.1).

ID ⁽¹⁾ CMaX	D (^o)	ID ⁽³⁾ 2MASS	J ⁽⁴⁾ mag	σ_J mag	H ⁽⁵⁾ mag	σ_H mag	K ⁽⁶⁾ mag	σ_K mag	Qflg ⁽⁷⁾	Mass ⁽⁸⁾ M _⊙	Age ⁽⁹⁾ Myr	WISE ⁽¹⁰⁾
E095b	4	07033880-1137227	16.593	0.164	15.031	–	14.786	–	CUU	–	–	–
C055	4	07033910-1127582	15.72	0.063	14.678	0.053	14.428	0.08	AAA	??	??	–
E131a	2	07033947-1132026	14.196	0.033	13.367	0.036	13.075	0.04	AAA	0.24	1.1	–
E131b	5	07033932-1132084	16.618	0.137	16.165	0.243	15.229	0.181	BDC	–	–	–
C057	2	07034002-1129480	14.683	0.036	14.031	0.037	13.804	0.046	AAA	0.95	18	–
C043	4	07034064-1123314	11.018	0.026	10.838	0.024	10.735	0.023	AAA	2.8	4.5	??
E086	2	07034209-1135139	13.35	0.026	12.604	0.027	12.428	0.032	AAA	0.85	1.9	Class III
E220*	6	07034331-1138091	15.553	0.056	14.979	0.086	14.769	0.131	AAB	–	–	–
E046*	0.5	07034316-1133062	6.543	0.019	5.216	0.027	3.766	0.178	AAC	–	–	–
E083	7	07034567-1129247	16.726	0.153	15.815	0.171	15.596	0.225	BCD	–	–	–
E336	9	07034625-1139093	16.265	0.104	15.857	0.183	15.276	–	ACU	–	–	–
E077	5	07034583-1129446	14.079	0.024	13.428	0.028	13.231	0.027	AAA	1.12	10	–
C016	3	07034610-1124021	13.108	0.03	12.301	0.028	12.014	0.023	AAA	??	??	Class III
E133	–	–	–	–	–	–	–	–	–	–	–	–
C051a	3	07034751-1131489	13.523	0.027	12.765	0.028	12.604	0.033	AAA	0.9	2.1	–
C051b	5	07034782-1131457	15.821	0.091	15.28	0.109	14.634	0.103	AAA	0.14	3	–
E173	4	07034733-1127333	14.127	0.029	13.464	0.037	13.237	0.03	AAA	1.05	7.5	??
E115	–	–	–	–	–	–	–	–	–	–	–	–
E039	3	07034869-1131502	13.986	0.03	13.207	0.032	13.017	0.029	AAA	0.65	3	–
E023	4	07034915-1141544	13.429	0.035	12.848	0.034	12.737	0.035	AAA	1.25	14	Class III
E061a	4	07034972-1132169	14.06	–	14.288	0.057	13.06	–	UAU	–	–	–
E061b	1	07034994-1132148	13.63	–	13.002	0.042	12.731	–	UAU	–	–	–
E157	3	07034996-1127384	14.35	0.032	13.459	0.04	13.087	0.03	AAA	0.15	0.19	??
E011	2	07035152-1134557	10.966	0.023	10.764	0.027	10.689	0.021	AAA	2.6	4.5	Class III
E119a	3	07035140-1140012	14.227	0.024	13.484	0.035	13.265	0.042	AAA	0.75	4	??
E119b	8	07035211-1139579	15.581	0.06	14.826	0.073	14.419	0.088	AAA	0.18	3.5	–
E190a	2	07035271-1123132	13.828	0.047	13.032	0.05	12.83	0.039	AAA	0.55	1.7	Class II/III
E190b	7	07035295-1123097	14.501	0.033	13.838	0.03	13.662	0.045	AAA	0.97	22	–
E142	3	07035234-1139061	13.588	0.033	12.83	0.031	12.613	0.034	AAA	0.65	1.9	??
E161	4	07035249-1126168	13.692	0.027	12.867	0.03	12.571	0.029	AAA	0.25	0.21	Class III
E104	2	07035283-1140177	13.785	0.026	13.116	0.03	12.938	0.029	AAA	1.2	6	??
E065a	1	07035303-1129352	12.356	0.024	11.54	0.022	10.947	0.021	AAA	??	??	Class II
E065b	5	07035278-1129314	16.047	0.141	13.47	–	12.906	–	BUU	–	–	–
E107a	4	07035324-1134449	15.104	0.041	14.253	0.05	13.893	0.059	AAA	0.15	1.2	–
E107b	4	07035338-1134504	13.44	0.026	12.479	0.027	11.925	0.026	AAA	??	??	Class II/III
E056	0.1	07035400-1132478	12.344	0.023	11.611	0.025	11.175	0.023	AAA	??	??	Class II
E074	1	07035472-1136057	14.444	0.026	13.715	0.03	13.538	0.034	AAA	0.95	9.5	Class III
E015a	5	07035503-1128181	14.142	0.027	13.433	0.028	13.199	0.03	AAA	0.8	4.5	–
E015b	10	07035414-1128235	14.115	0.18	13.429	0.143	13.31	0.06	CBA	–	–	–
E072	1	07035486-1134340	8.898	0.021	8.913	0.024	8.93	0.021	AAA	9	4	Class III
E079	4	07035523-1138157	14.341	0.032	13.602	0.03	13.427	0.044	AAA	0.85	8	??
C047a	9	07035584-1127544	14.048	0.055	13.372	0.054	13.156	0.046	AAA	1	6	Class II/III
C047b	3	07035584-1128029	14.117	0.032	13.324	0.028	13.053	0.035	AAA	0.28	1.5	Class III
E044	1	07035564-1132468	10.775	0.023	10.395	0.025	10.312	0.023	AAA	2.8	4	??
E017	2	07035575-1129315	12.922	0.024	12.219	0.022	12.017	0.024	AAA	0.9	1.2	??
E026	0.7	07035587-1133385	12.369	0.024	11.539	0.028	11.239	0.025	AAA	??	??	Class III
E198	0.6	07035594-1143099	13.464	0.027	12.743	0.028	12.473	0.027	AAA	0.58	1.1	Class III
E031a	6	07035586-1142141	15.103	0.043	14.409	0.059	14.143	0.072	AAA	0.75	16	??
E031b	1	07035591-1142065	13.631	0.029	13.049	0.03	12.955	0.037	AAA	1.18	20	??
E031c	10	07035555-1141594	15.898	0.069	15.289	0.108	14.824	0.113	ABB	–	–	–
E378a	2	07035646-1129476	14.034	0.042	13.237	0.042	13.005	0.049	AAA	0.4	1.6	??
E378b	5	07035674-1129447	15.59	0.07	15.014	0.092	14.458	0.096	AAA	0.18	4	–
E099	3	07035666-1134553	12.938	0.024	11.872	0.027	11.169	0.023	AAA	??	??	Class II
E089a	1	07035678-1139106	14.146	0.036	13.498	0.042	13.351	0.044	AAA	1.09	17.5	??
E089b	5	07035716-1139136	15.791	0.074	15.148	0.095	14.714	0.132	AAB	–	–	–
E003	2	07035708-1128317	12.366	0.022	11.69	0.028	11.467	0.023	AAA	0.95	0.85	Class III
E150	3	07035760-1125367	14.624	0.043	13.855	0.049	13.591	0.047	AAA	2.1	0.35	–
E042	2	07035770-1124199	11.269	0.024	10.918	0.026	10.805	0.021	AAA	2.35	6	Class III
E103	5	07035800-1130081	14.545	0.043	13.765	0.058	13.46	0.044	AAA	0.26	1.95	–
E091a	0.7	07035805-1132398	14.102	0.032	13.227	0.032	12.927	0.037	AAA	0.21	0.5	–
E091b	6	07035820-1132458	16.694	0.144	16.047	–	15.131	–	BUU	–	–	–
E106	4	07035833-1134188	14.746	0.029	13.982	0.042	13.781	0.054	AAA	0.75	8	–
E078	4	07035859-1129377	12.969	0.024	12.193	0.022	11.78	0.024	AAA	??	??	Class II
E016a	4	07035880-1135311	10.722	0.023	10.536	0.024	10.468	0.023	AAA	2.5	3.5	Class III
E016b	8	07035865-1134100	15.927	0.075	15.185	0.101	14.92	0.126	AAB	–	–	–
E016c	6	07035884-1134219	16.385	0.116	15.22	0.101	14.859	0.125	BAB	–	–	–
E034	0.9	07035994-1130318	13.207	–	12.271	–	12.247	0.037	UUA	–	–	–
E067a	1	07040041-1133596	12.099	0.03	10.916	0.028	10.19	0.026	AAA	??	??	Class II
E067b	5	07040075-1133559	16.077	0.218	15.146	0.181	15.001	0.209	DCC	–	–	–
E359	3	07040072-1123234	15.714	0.056	13.156	0.026	11.798	0.024	AAA	??	??	Class II/III
E085	3	07040086-1127142	13.374	0.043	12.922	0.044	12.874	0.039	AAA	1.35	26	Class III
E058	4	07040091-1138254	13.4	0.029	12.816	0.031	12.543	0.034	AAA	1.15	4	Class III
E032a	6	07040132-1136174	14.774	0.045	13.926	0.05	13.418	0.042	AAA	??	??	??
E032b	2	07040114-1136255	13.5	–	12.685	0.035	12.512	0.038	UAA	–	–	–
E055a	2	07040119-1128454	13.581	0.029	12.856	0.028	12.719	0.034	AAA	1.15	4	Class III
E055b	9	07040181-1128460	16.255	0.092	15.299	0.112	15.151	0.158	ABC	–	–	–
E053	–	–	–	–	–	–	–	–	–	–	–	–
E093	2	07040165-1121322	15.356	0.047	13.851	0.032	12.983	0.027	AAA	??	??	??
E080	5	07040154-1126102	16.561	0.12	16.074	0.217	15.416	–	BDU	–	–	–

Table B.2. Continued. Column description: (1) X-ray source identification (Table B.1); (2) Distance from X-ray source center; (3) 2MASS identification (4, 5 and 6) J, H and K magnitudes; (7) 2MASS Quality flag; (8) Mass; (9) Age; (10) WISE classification. Note: (*) Counterpart candidate not considered, due to distance incompatible with the cloud (see Sect. 4.1).

ID ⁽¹⁾ CMaX	D (^o)	ID ⁽³⁾ 2MASS	J ⁽⁴⁾ mag	σ_J mag	H ⁽⁵⁾ mag	σ_H mag	K ⁽⁶⁾ mag	σ_K mag	Qflg ⁽⁷⁾	Mass ⁽⁸⁾ M _⊙	Age ⁽⁹⁾ Myr	WISE ⁽¹⁰⁾
E040a	10	07040235-1123385	16.354	0.15	15.264	0.155	15.05	0.149	BBB	–	–	–
E040b	9	07040274-1123252	15.864	0.482	13.937	0.105	12.578	0.04	DAA	–	–	–
E068a	2	07040224-1124188	13.473	0.026	12.643	0.028	12.464	0.027	AAA	0.52	0.95	–
E068b	8	07040267-1124244	15.719	0.101	14.842	0.102	14.633	0.115	AAB	–	–	–
E036a	2	07040234-1125393	10.396	0.047	10.321	0.071	10.261	0.024	AAA	3.6	1.9	–
E036b	6	07040225-1125429	11.306	0.03	10.75	0.034	9.941	0.052	AAA	??	??	Class I
E057a	8	07040284-1132155	11.233	0.021	11.169	0.025	11.161	0.025	AAA	3	4	Class III
E057b	3	07040290-1132074	13.91	0.04	13.143	0.036	12.902	0.033	AAA	0.51	1.6	–
E057c	9	07040369-1132090	14.573	0.033	14.016	0.041	13.784	0.054	AAA	0.95	32	–
E057d	5	07040338-1132044	16.513	0.137	15.813	0.18	15.348	0.2	BCC	–	–	–
E019a	3	07040330-1133586	13.74	0.033	12.971	0.037	12.769	0.045	AAA	0.65	1.9	Class I
E019b	4	07040285-1133579	13.154	0.046	11.897	0.037	11.398	0.034	AAA	??	??	–
E019c	5	07040320-1133530	16.132	0.119	15.222	0.13	14.175	–	BBU	–	–	–
E019d	9	07040345-1134060	16.586	–	15.665	0.176	14.671	0.106	UCA	–	–	–
E075	1	07040309-1128071	13.296	0.027	12.627	0.026	12.488	0.03	AAA	1.45	5.5	??
E138	3	07040337-1138030	13.716	0.023	12.94	0.028	12.785	0.027	AAA	0.85	3	??
E002a	2	07040393-1126097	9.758	0.027	9.717	0.035	9.63	0.024	AAA	4.5	1.3	Class III
E002b	6	07040427-1126148	13.8	0.065	12.945	0.059	12.812	0.047	AAA	0.6	1.9	–
E043a	3	07040426-1123451	13.401	0.036	12.705	0.049	12.502	0.037	AAA	0.98	2.1	–
E043b	5	07040390-1123480	13.926	0.029	13.099	0.038	12.839	0.033	AAA	0.26	1.1	Class II/III
E125	3	07040451-1124212	13.519	0.029	12.717	0.035	12.45	0.027	AAA	0.285	0.5	Class III
E110a	4	07040461-1122328	13.425	0.024	12.692	0.026	12.514	0.029	AAA	0.9	2	Class III
E110b	6	07040507-1122253	14.666	0.035	13.912	0.047	13.624	0.047	AAA	0.29	2.1	–
E101	4	07040505-1123265	16.342	0.116	14.874	0.073	13.822	0.053	BAA	–	–	–
E060	2	07040542-1128562	10.095	0.024	10.062	0.022	10.038	0.019	AAA	4.5	1.2	Class III
E102	4	07040593-1123587	14.418	0.033	13.47	0.026	12.933	0.031	AAA	??	??	Class II
E185*	7	07040696-1142216	15.981	0.072	15.601	0.144	15.434	0.193	ABC	–	–	–
E127	4	07040649-1144473	14.015	0.04	13.456	0.034	13.311	0.05	AAA	1.05	25	??
E193	–	–	–	–	–	–	–	–	–	–	–	–
E092*	9	07040670-1127238	16.069	0.091	15.411	0.126	15.228	0.196	ABC	–	–	–
E140a	7	07040707-1121393	14.503	0.026	13.591	0.032	13.314	0.039	AAA	0.19	0.9	Class III
E140b	10	07040676-1121358	16.665	0.147	15.906	0.199	15.546	0.222	BCD	–	–	–
E096	3	07040744-1146306	15.224	0.048	14.441	0.064	14.412	0.093	AAA	0.79	55	??
E014a	8	07040742-1123127	15.292	0.086	14.5	0.094	14.262	0.12	AAB	–	–	–
E014b	2	07040797-1123114	14.354	–	14.228	0.091	13.682	0.075	UAA	–	–	–
E014c	5	07040812-1123137	14.291	–	13.774	0.093	13.504	0.09	UAA	–	–	–
E014d	4	07040816-1123097	15.455	0.111	14.586	0.055	14.188	0.075	e0AA	??	??	–
E109a	3	07040803-1123547	13.115	0.033	12.441	0.037	12.198	0.03	AAA	0.85	1.4	–
E109b	7	07040839-1123579	15.241	0.054	14.495	0.082	14.281	0.098	AAA	0.75	17.5	–
E113a	8	07040881-1140033	15.505	0.056	14.965	0.07	14.606	0.098	AAA	0.75	40	–
E113b	1	07040892-1139560	14.695	0.047	13.843	0.043	13.664	0.05	AAA	0.35	2.2	??
E020a	8	07040918-1130075	13.648	0.027	12.956	0.024	12.863	0.035	AAA	1.3	10	Class III
E020b	4	07040946-1130168	14.114	0.03	13.443	0.032	13.271	0.044	AAA	1.1	12	Class III
E094a	1	07041037-1131451	14.017	0.029	13.263	0.024	13.015	0.035	AAA	1.9	0.51	??
E094b	8	07041008-1131518	15.901	0.065	15.288	0.108	14.558	0.089	ABA	–	–	–
E137	2	07041065-1134323	15.377	0.051	14.612	0.077	13.927	0.063	AAA	??	??	–
E169	–	–	–	–	–	–	–	–	–	–	–	–
E081	2	07041176-1125125	14.529	0.036	13.746	0.037	13.566	0.046	AAA	0.8	6	??
E038	3	07041191-1121312	11.927	0.024	11.263	0.021	11.009	0.024	AAA	0.9	0.6	Class III
E008	2	07041233-1139229	11.311	0.035	11.039	0.028	10.957	0.026	e0AA	–	–	??
E108	2	07041357-1135085	14.695	0.044	14.076	0.028	13.809	0.054	AAA	0.92	17	Class II/III
E154	3	07041424-1123169	13.896	0.028	12.982	0.022	12.341	0.026	AAA	??	??	Class II
E129	2	07041458-1139547	14.126	0.032	13.379	0.028	13.076	0.038	AAA	0.29	1.5	??
E050	–	–	–	–	–	–	–	–	–	–	–	–
E062	2	07041511-1133577	14.135	0.03	13.308	0.026	13.076	0.035	AAA	0.27	1.5	??
E097	9	07041492-1145438	16.449	0.118	15.811	0.2	15.357	–	BCU	–	–	–
E205a	5	07041523-1121326	15.436	0.064	14.78	0.08	14.517	0.082	AAA	0.75	35	–
E205b	8	07041484-1121315	13.879	0.037	12.971	0.04	12.564	0.031	AAA	??	??	Class II
E111a	7	07041653-1126093	15.362	0.069	14.834	0.1	14.469	0.087	AAA	0.85	38	–
E111b	5	07041591-1126137	14.261	0.04	13.53	0.047	13.238	0.035	AAA	0.4	1.9	–
E111c	1	07041601-1126100	12.905	0.041	12.145	0.049	11.737	0.035	AAA	??	??	Class II/III
E028	5	07041588-1124055	8.947	0.024	8.896	0.024	8.853	0.021	AAA	6.2	0.8	Class III
E087a	3	07041595-1133363	14.72	0.047	13.871	0.05	13.719	0.054	AAA	0.55	4.5	??
E087b	7	07041567-1133374	16.429	0.129	14.618	–	14.304	–	BUU	–	–	–
E149*	8	07041634-1137072	14.269	0.029	13.975	0.03	13.915	0.051	AAA	–	–	–
E195a	4	07041621-1123480	13.229	0.033	12.463	0.024	12.226	0.026	AAA	0.55	0.5	–
E195b	6	07041639-1123509	13.066	0.067	12.315	0.074	12.056	0.055	AAA	0.5	0.3	Class II
E177	8	07041626-1129598	11.267	0.024	11.108	0.022	11.045	0.024	AAA	2.7	5	Class III
E120a	4	07041638-1127455	13.673	0.032	12.943	0.032	12.687	0.033	AAA	0.58	1.5	??
E120b	6	07041673-1127371	15.549	0.058	14.898	0.077	14.409	0.087	AAA	0.18	3.5	–
E117a	9	07041736-1143103	10.208	0.024	10.117	0.024	10.039	0.019	AAA	3.75	1.8	Class III
E117b	4	07041652-1143064	14.056	0.036	13.257	0.034	13.046	0.037	AAA	0.51	1.9	–
E141a	4	07041779-1128212	14.499	0.054	13.75	0.062	13.3	0.051	AAA	0.19	0.9	??
E141b	5	07041804-1128239	15.343	0.049	14.452	0.05	14.228	0.074	AAA	0.22	3.7	–
E025	2	07041786-1134268	14.132	0.032	13.27	0.03	13.081	0.033	AAA	0.28	1.5	??
E030a	4	07041812-1125280	13.14	0.035	12.423	0.04	12.275	0.039	AAA	1.15	2.2	??
E030b	2	07041839-1125239	14.389	0.03	13.557	0.035	13.387	0.045	AAA	0.65	2.3	??
E005a	2	07041833-1142359	12.031	0.024	11.476	0.022	11.32	0.021	AAA	2.1	3.5	Class III
E005b	9	07041829-1142442	16.709	0.17	15.376	–	15.42	–	CUU	??	??	–

Table B.2. Continued. Column description: (1) X-ray source identification (Table B.1); (2) Distance from X-ray source center; (3) 2MASS identification (4, 5 and 6) J, H and K magnitudes; (7) 2MASS Quality flag; (8) Mass; (9) Age; (10) WISE classification. Note: (*) Counterpart candidate not considered, due to distance incompatible with the cloud (see Sect. 4.1).

ID ⁽¹⁾ CMaX	D (^o)	ID ⁽³⁾ 2MASS	J ⁽⁴⁾ mag	σ_J mag	H ⁽⁵⁾ mag	σ_H mag	K ⁽⁶⁾ mag	σ_K mag	Qflg ⁽⁷⁾	Mass ⁽⁸⁾ M _⊙	Age ⁽⁹⁾ Myr	WISE ⁽¹⁰⁾
E012	2	07041912-1133480	13.097	0.033	12.418	0.043	12.162	0.033	e0e0e0	–	–	–
E105	7	07041898-1137255	15.28	0.05	14.473	0.055	14.315	0.066	AAA	0.74	17	??
E004	2	07041923-1125077	12.904	0.026	12.354	0.028	12.26	0.027	AAA	1.45	12	Class III
E128	5	07041959-1144087	14.897	0.042	14.201	0.047	14.045	0.064	AAA	0.97	26	Class III
E122	2	07041999-1132150	14.537	0.04	13.738	0.049	13.469	0.049	AAA	0.28	1.8	Class II
E071	3	07042018-1124325	14.256	0.029	13.517	0.022	13.271	0.037	AAA	0.6	3	Class III
E147	5	07042071-1125537	15.747	0.091	15.2	0.109	14.703	0.106	AAA	0.29	6	??
E033	4	07042063-1136443	14.596	0.03	13.726	0.028	13.539	0.045	AAA	0.28	2	??
E143	0.4	07042086-1129361	13.801	0.024	12.883	0.022	12.286	0.024	AAA	??	??	Class II
E007a	2	07042135-1137043	12.48	0.026	11.906	0.024	11.758	0.023	AAA	1.85	4	??
E007b	7	07042103-1136565	15.252	0.053	14.588	0.076	14.188	0.071	AAA	0.28	4	–
E130a	3	07042153-1129165	15.15	–	14.251	0.062	14.013	–	UAU	–	–	–
E130b	6	07042176-1129184	15.673	–	15.664	0.167	14.42	–	UCU	–	–	–
E066	3	07042196-1122296	11.296	0.023	11.132	0.021	11.034	0.019	AAA	2.65	5.5	Class III
E126	1	07042202-1139318	14.784	0.03	14.076	0.038	13.86	0.047	AAA	0.86	14	??
E013	2	07042250-1131400	13.238	0.024	12.558	0.024	12.356	0.019	AAA	1.05	2.5	??
E049	3	07042264-1130482	13.287	0.043	12.635	0.04	12.417	0.027	AAA	1.1	3	??
E063a	3	07042319-1127184	13.043	0.032	12.316	0.032	12.075	0.026	AAA	0.65	0.105	Class III
E063b	9	07042296-1127235	16.521	0.166	15.241	–	14.815	–	CUU	–	–	–
E047	5	07042325-1124172	13.451	0.024	12.643	0.03	12.191	0.024	AAA	??	??	Class II
E024	3	07042340-1132515	13.224	0.026	12.481	0.024	12.323	0.027	AAA	0.95	1.8	Class III
E027	–	–	–	–	–	–	–	–	–	–	–	–
E059	3	07042412-1125020	14.112	0.03	13.525	0.035	13.388	0.039	AAA	1.05	25	??
E146	–	–	–	–	–	–	–	–	–	–	–	–
E022a	2	07042617-1131287	12.909	0.026	12.15	0.026	11.967	0.027	AAA	0.78	0.1	–
E022b	2	07042625-1131207	12.47	0.026	11.601	0.026	11.152	0.023	AAA	??	??	Class II
E153a	3	07042640-1132211	11.699	0.022	11.604	0.024	11.593	0.023	AAA	2.5	6	??
E153b	3	07042621-1132166	15.81	0.156	15.545	0.198	13.771	–	CCU	–	–	–
E212	4	07042768-1127197	14.583	0.029	13.803	0.044	13.481	0.038	AAA	0.25	2.1	–
E052	5	07042775-1146266	12.872	0.033	12.396	0.038	12.28	0.034	AAA	1.37	16	??
E018a	2	07042798-1134431	12.41	0.03	11.726	0.034	11.533	0.03	AAA	0.5	0.9	Class III
E018b	7	07042820-1134486	14.8	0.051	14.067	0.071	13.793	0.05	AAA	0.53	4	??
E168	4	07042829-1138507	16.038	0.083	15.255	0.138	14.725	–	ABU	–	–	–
E010a	3	07042982-1147208	11.153	0.022	10.47	0.024	10.305	0.021	AAA	1.6	0.6	Class III
E010b	10	07042944-1147264	14.161	0.053	13.482	0.07	13.32	0.05	AAA	1.1	17.5	??
E116	5	07043054-1126150	14.031	0.029	13.285	0.03	13.166	0.021	AAA	1.1	8	??
E148*	9	07043091-1123021	14.384	0.03	14.129	0.049	13.955	0.051	AAA	–	–	–
E186	4	07043077-1134330	14.035	0.043	13.241	0.044	12.963	0.038	AAA	0.27	1.2	Class III
E035a	1	07043129-1132402	15.436	0.049	14.554	0.057	14.26	0.065	AAA	0.18	0.3	–
E035b	3	07043099-1132417	13.901	0.06	13.137	0.079	12.876	0.059	e0e0A	–	–	–
E114	3	07043198-1133181	14.553	0.024	13.826	0.028	13.608	0.038	AAA	0.82	8	??
E098a	4	07043345-1126304	13.629	0.022	12.838	0.03	12.615	0.026	AAA	0.5	1.1	Class III
E098b	4	07043367-1126241	16.645	0.123	15.885	0.188	15.267	0.179	BCC	–	–	–
E164a	5	07043357-1135329	14.898	0.044	14.267	0.055	14.163	0.074	AAA	0.85	55	Class III
E164b	10	07043319-1135327	16.083	0.084	15.375	0.153	15.084	–	ABU	–	–	–
E164c	7	07043415-1135346	16.665	0.126	15.634	0.146	15.25	–	BBU	–	–	–
E064	3	07043428-1134501	14.427	0.039	13.656	0.036	13.445	0.049	AAA	0.6	4.8	–
E084	3	07043739-1129384	11.647	0.024	11.277	0.025	11.131	0.021	AAA	1.85	7	Class III
E090a	9	07043765-1126531	12.262	0.023	11.974	0.026	11.919	0.027	AAA	1.65	12.5	Class III
E090b	3	07043811-1126451	16.372	0.199	15.065	–	15.028	–	CUU	–	–	–
E090c	2	07043812-1126501	16.403	0.207	15.142	0.164	14.341	0.128	CCB	–	–	–
E090d	9	07043874-1126453	16.302	0.146	15.519	–	15.34	–	BUU	–	–	–
E009a	3	07043829-1131265	7.392	0.029	7.416	0.046	7.415	0.029	AAA	15	4	Class III
E009b	7	07043848-1131311	8.693	0.095	8.631	0.104	8.793	0.08	AAA	10	4	–
E203	4	07043946-1126126	14.556	0.041	13.86	0.028	13.579	0.049	AAA	0.65	4.9	Class III
E112	4	07043968-1133593	14.576	0.043	13.8	0.036	13.544	0.049	AAA	0.35	2.1	??
E088	7	07043962-1146155	14.236	0.051	13.612	0.043	13.337	0.052	AAA	0.97	8	Class III
E156a	8	07044000-1136206	13.864	0.045	13.242	0.051	13.026	0.043	AAA	1.18	9	Class III
E156b	4	07044007-1136282	15.307	0.062	14.56	0.033	14.305	0.09	AAA	0.55	11	–
E156c	5	07044029-1136222	15.94	0.128	15.616	0.131	14.066	–	BBU	–	–	–
E132	3	07044011-1130333	11.747	0.023	11.375	0.023	11.239	0.023	AAA	1.75	7.5	Class III
E100	5	07044125-1135469	14.99	0.056	14.266	0.061	14.011	0.069	AAA	0.65	9	??
E069	3	07044183-1146282	13.471	0.026	12.834	0.03	12.767	0.033	AAA	1.29	14	Class III
E165	3	07044186-1132587	14.681	0.039	13.887	0.029	13.171	0.041	AAA	??	??	Class II
E041a	8	07044185-1137104	15.458	0.073	14.665	0.079	14.488	0.103	AAA	0.68	22	–
E041b	4	07044200-1137191	13.742	0.024	13.198	0.025	13.032	0.033	AAA	0.15	17.5	??
E191	0.5	07044244-1144047	15.282	0.065	14.719	0.057	14.454	0.119	AAB	–	–	–
E037	3	07044250-1136133	14.468	0.036	13.763	0.044	13.617	0.055	AAA	1	17	–
E135	10	07044469-1129527	13.779	0.033	13.314	0.041	13.163	0.044	AAA	1.09	26	??
E082	3	07044524-1124420	11.957	0.028	11.385	0.032	11.213	0.029	AAA	2.1	2.1	Class III
E136	2	07044544-1137593	10.919	0.024	10.762	0.025	10.705	0.019	AA	2.9	4	Class III
E145*	3	07044984-1131136	14.329	0.026	14.149	0.052	14.111	0.074	AAA	–	–	–
E184	7	07045169-1124577	13.585	0.028	13.222	0.03	13.061	0.04	AAA	1.19	25	??
E006	2	07045242-1138490	7.451	0.021	7.016	0.046	6.915	0.029	AA	6.5	0.15	Class III
E163*	7	07045354-1137002	14.142	0.029	13.797	0.047	13.607	0.051	AAA	–	–	–
E070	2	07045407-1138362	13.06	0.022	12.486	0.022	12.346	0.023	AAA	1.55	8	Class III
E029a	10	07045640-1134229	14.771	0.036	14.245	0.048	14.032	0.068	AA	0.88	45	–
E029b	3	07045577-1134175	11.532	0.026	10.871	0.029	10.481	0.024	AAA	??	??	Class II
E021	5	07045632-1129332	11.457	0.022	10.846	0.022	10.197	0.021	AAA	??	??	Class II

Table B.2. Continued. Column description: (1) X-ray source identification (Table B.1); (2) Distance from X-ray source center; (3) 2MASS identification (4, 5 and 6) J, H and K magnitudes; (7) 2MASS Quality flag; (8) Mass; (9) Age; (10) WISE classification. Note: (*) Counterpart candidate not considered, due to distance incompatible with the cloud (see Sect. 4.1).

ID ⁽¹⁾ CMaX	D (")	ID ⁽³⁾ 2MASS	J ⁽⁴⁾ mag	σ_J mag	H ⁽⁵⁾ mag	σ_H mag	K ⁽⁶⁾ mag	σ_K mag	Qflg ⁽⁷⁾	Mass ⁽⁸⁾ M _⊙	Age ⁽⁹⁾ Myr	WISE ⁽¹⁰⁾
E124	6	07045894-1127572	14.031	0.035	13.333	0.029	13.131	0.033	AAA	1	6	??
E045	2	07050033-1137419	12.895	0.023	12.243	0.023	12.029	0.023	AAA	1.15	1.8	??
E152*	5	07050114-1136139	15.282	0.069	14.723	0.086	14.567	0.112	AAB	–	–	–
E144	6	07050082-1141270	9.308	0.024	9.098	0.027	9.012	0.024	AAA	4.1	1.1	Class III
E139*	6	07050104-1131173	14.365	0.039	14.08	0.039	14.039	0.073	AAA	–	–	–
E123a	8	07050146-1138300	14.647	0.045	14.068	0.039	13.777	0.063	AAA	0.95	19	??
E123b	9	07050252-1138265	16.025	0.115	15.291	0.102	15.106	0.192	BAC	–	–	–
E181a	4	07050397-1122517	10.348	0.024	9.8	0.022	9.702	0.024	AAA	3.3	1.5	Class III
E181b	6	07050442-1122454	14.888	0.062	14.428	0.078	14.07	0.071	AAA	0.85	40	–
E181c	7	07050362-1122470	15.97	0.328	15.41	0.488	13.564	–	DDU	–	–	–
E001	6	07050441-1143071	12.322	0.024	11.692	0.025	11.499	0.025	AAA	1.55	1.5	Class III
E183	8	07050676-1130272	15.824	0.084	15.301	0.09	14.855	0.144	AAB	–	–	–
E151	6	07050727-1141589	12.544	0.024	12.329	0.027	12.237	0.029	AAA	1.65	17	??
E214	0.8	07050912-1134477	13.219	0.023	12.732	0.03	12.58	0.033	AAA	1.25	17.5	??
E048*	5	07051013-1128260	16.522	0.171	15.724	0.146	15.575	–	CCU	–	–	–
E054	4	07050985-1129411	12.448	0.024	11.754	0.022	11.522	0.024	AAA	0.85	0.8	Class III
E155a	5	07051077-1138539	15.171	0.054	14.62	0.064	14.2	0.088	AAA	0.7	13	??
E155b	10	07051036-1138515	16.002	0.096	15.68	0.154	15.031	0.181	ABC	–	–	–
E194	4	07051131-1134358	14.628	0.049	13.903	0.044	13.599	0.06	AAA	0.38	2.1	Class III
E121	9	07051248-1132500	13.803	0.024	13.058	0.027	12.811	0.04	AAA	0.66	1.8	Class III
E202a	4	07051217-1135218	11.946	0.027	11.779	0.027	11.782	0.027	AAA	2.1	10	Class III
E202b	7	07051183-1135283	15.096	0.062	14.294	0.057	13.998	0.072	AAA	0.24	3.5	–
E167a	9	07051198-1136500	14.164	0.036	13.381	0.032	13.185	0.04	AAA	0.65	3	??
E167b	4	07051208-1136380	14.43	0.042	13.75	0.041	13.667	0.061	AAA	0.96	30	??
E134	4	07051489-1130542	11.826	0.021	11.593	0.025	11.55	0.027	AAA	1.95	8	Class III
E073	5	07051571-1132050	12.746	0.024	12.133	0.028	12.028	0.03	AAA	1.7	6	Class III